論文 / 著書情報
Article / Book Information

題目(和文)	高移動度・高ヘイズを有する薄膜シリコン太陽電池用フッ素ドープ酸化スズ透明導電膜の研究
Title(English)	Study of Fluorine Doped Tin Oxide Transparent Conductive Oxide Films with High Mobility and High Haze for Thin-Film Silicon Solar Cells
著者(和文)	一色眞誠
Author(English)	Masanobu Isshiki
出典(和文)	学位:博士（工学）, 学位授与機関:東京工業大学, 報告番号:甲第9631号, 授与年月日:2014年9月25日, 学位の種別:課程博士, 審査員:小長井　誠,山田　明,中川　茂樹,間中　孝彰,宮島　晋介
Citation(English)	Degree:, Conferring organization: Tokyo Institute of Technology, Report number:甲第9631号, Conferred date:2014/9/25, Degree Type:Course doctor, Examiner:,,,,
学位種別(和文)	博士論文
Type(English)	Doctoral Thesis

DOCTORAL THESIS

Study of Fluorine Doped Tin Oxide Transparent Conductive Oxide Films with High Mobility and High Haze for Thin-Film Silicon Solar Cells

A THESIS SUBMITTED IN PARTIAL FULFILLMENT OF THE REQUIREMENT FOR THE DEGREE OF DOCTOR OF ENGINEERING

August 2014

Masanobu Isshiki
Directed by Professor Makoto Konagai

Department of Physical Electronics
Graduate School of Science and Engineering
Tokyo Institute of Technology

Contents

Chapter 1

1 Introduction

1.1 Global Environment and Energy

After the industrial revolution, many technologies have been developed and human being has received the benefit from the fruits. As the result of the industrial activity of human being, huge amount of carbon dioxide (CO_2) gas have been emitted into the air. The CO_2 is one of the greenhouse gases, which can absorb and emit infrared radiation, but not radiation in or near the visible light region.

The Intergovernmental Panel on Climate Change (IPCC) recently provided three working group (WG) reports in the Fifth Assessment Report (AR5)[1]–[3]. The report of WG1 describes below.

(1) Emission of CO_2 gas due to the activity of human being has the largest effect on the warming of the climate system.

(2) Continued emissions of greenhouse gases will cause further warming and changes in all components of the climate system. Limiting climate change will require substantial and sustained reductions of greenhouse gas emissions.

(3) Global mean surface increment in 2081~2100 compared to 1986~2005 is estimated in 4 scenarios of greenhouse gas emissions, as shown in below and Fig. 1-1.

RCP2.6 : 0.3 ~ 1.7 °C

RCP4.5 : 1.1 ~ 2.6 °C

RCP6.0 : 1.4 ~ 3.1 °C

RCP8.5 : 2.6 ~ 4.8 °C

where RCP means Representative Concentration Pathway, and the number means radiative forcing in 2100 relative to 1750. The unit is W/m^2.

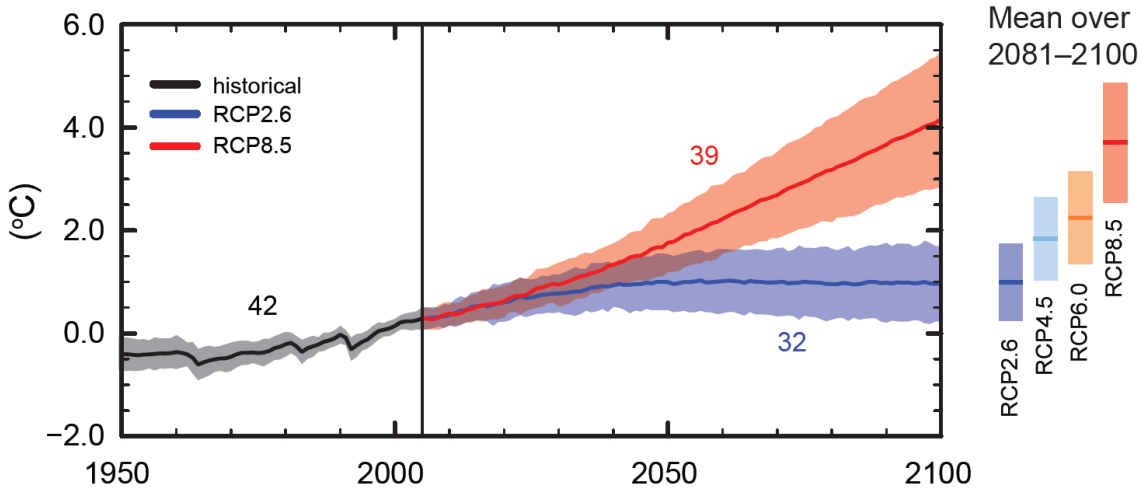

Fig. 1-1 Estimated global mean surface temperature in 4 senarios[1].

(4) Cumulative emissions of CO_2 largely determine the global mean surface warming by the late 21st century and beyond (Fig. 1-2). Most aspects of climate change will persist for many centuries, even if emissions of CO_2 are stopped. This represents a substantial multi-century climate change commitment created by past, present and future emissions of CO_2.

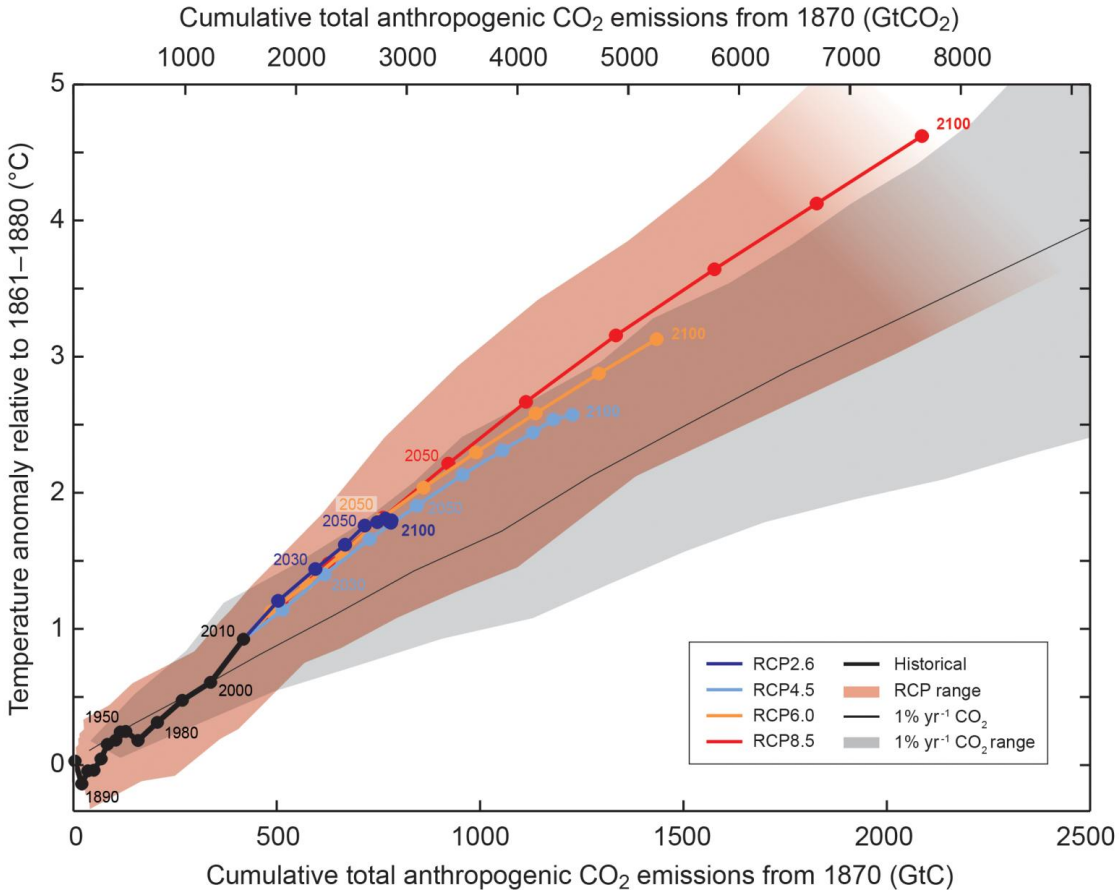

Fig. 1-2 Global mean surface temperature increase as a function of cumulative total global CO_2 emissions from various lines of evidence. Multi-model results from a hierarchy of climate-carbon cycle models for each RCP until 2100 are shown with coloured lines and decadal means (dots). Some decadal means are labeled for clarity (e.g., 2050 indicating the decade 2040−2049). Model results over the historical period (1860 to 2010) are indicated in black[1].

One of the targets that has been suggested is to limit the global warming below 2 °C, relative to the pre-industrial level[4][5]. The 2 °C target was adopted in 2010 by Parties to the United Nations Framework Convention on Climate Change (COP16)[6]. To achieve the target, we need to realize RCP2.6 scenario. the report of WG3 of AR5 of

IPCC shows Fig. 1-3[3], which describe the greenhouse gas emission pathways from 2000 to 2100 of all scenarios. In order to realize RCP2.6, we must to start reducing the greenhouse gas emission immediately, and need to achieve almost zero emission around 2100.

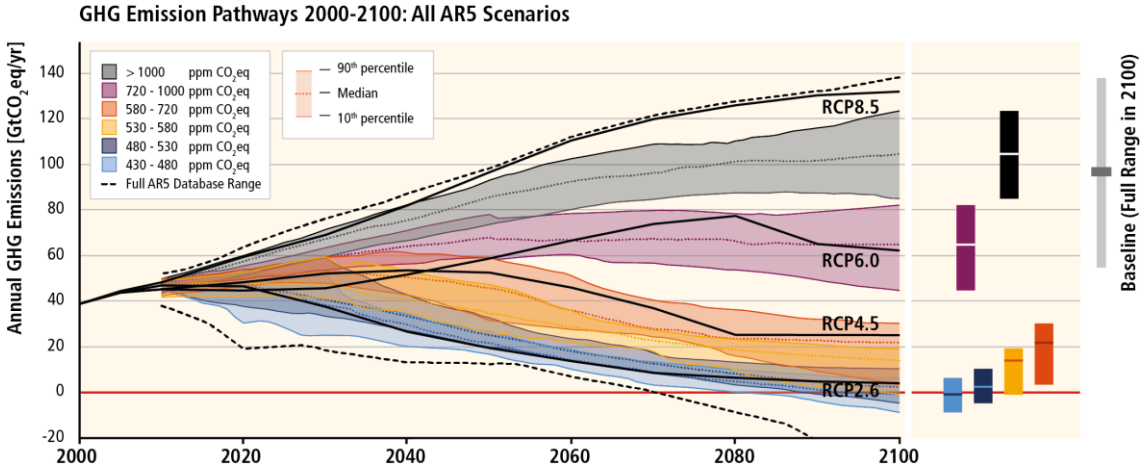

Fig. 1-3 The greenhouse gas emission pathways from 2000 to 2100 in all scenarios.[3]

To reduce the emission of CO_2 gas, we need to utilize renewable energies such as solar power, wind power, geothermal power, biomass power, and so on. According to EPIA, 100GW PV system can reduce CO_2 emission of 53 Mt / Year[7]. (Most of renewable energy sources have similar capability of reducing CO_2 emission[8].) In order to eliminate all CO_2 emission in 2013 (~ 45 $GtCO_2eq/yr$), 85TW PV will be needed by rough calculation. Renewable Energy Policy Network for the 21st Century reported that the cumulative installed renewable power capacity (excluding hydro) reached to 560GW at the end of 2013, and approximate 80GW was installed in 2012[9]. These values are rapidly increasing recently, but they are still much smaller than 85 TW calculated above. Therefore, drastically increasing of renewable power capacity is required.

1.2 Photovoltaic (PV)

Among the renewable power source, photovoltaic (PV) plays an important role. Fig. 1-4 shows the trend of the cumulative installed photovoltaic[9]. The cumulative installed PV all over the world reached at 139GW in 2013, and 39GW was installed in 2013. As described above, we need to accelerate the installation of PV.

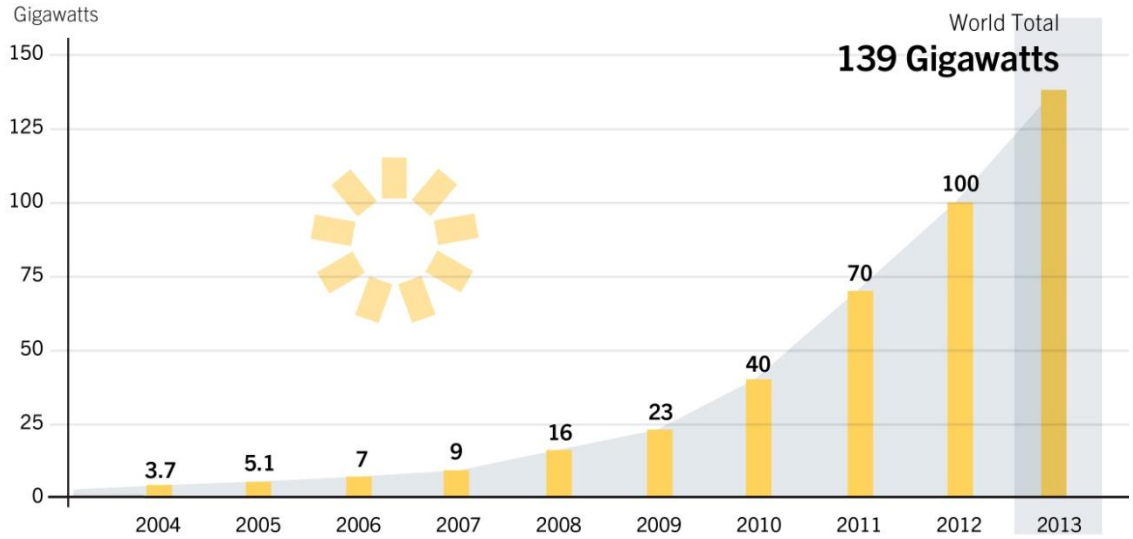

Fig. 1-4 Trend of the cumulative installed photovoltaic power[9].

To accelerate the installation of PV, reducing costs of power generation is a key factor. New Energy and Industrial Technology Development Organization (NEDO : Japanese independent administrative agency) set up a long-term roadmap called “PV2030”[10] in 2004. It was revised in 2009 as “PV2030+”[11] to consider the growth of PV power generation over the extended period toward 2050 from 2030, and to assume volume expansion of PV power generation to the extent that it would contribute to global warming. Fig. 1-5 shows the cost reduction scenario. Targets of power

generation cost are presented as 14Yen/kWh (equivalent to commercial electricity) at 2020, 7Yen/kWh (equivalent to general power source) at 2030, and below 7Yen/kWh (used as general power source) at 2050. To reduce the generation cost, improving efficiency is important. Development targets of solar cells and modules suggested in PV2030+ are shown in Table 1-1. To achieve this target, NEDO has launched some projects of research and development (R&D) on photovoltaic. For example, R&D on "Innovative Solar Cells" launched in 2008, which aims to improve drastically the conversion efficiency of solar cells using new and innovative concepts in long-term. R&D on "Next-generation high performance systems" launched in 2010, which aims to develop high performance PV system technology to reduce cost to 14~7Yen/kWh in middle term (2020~2030).

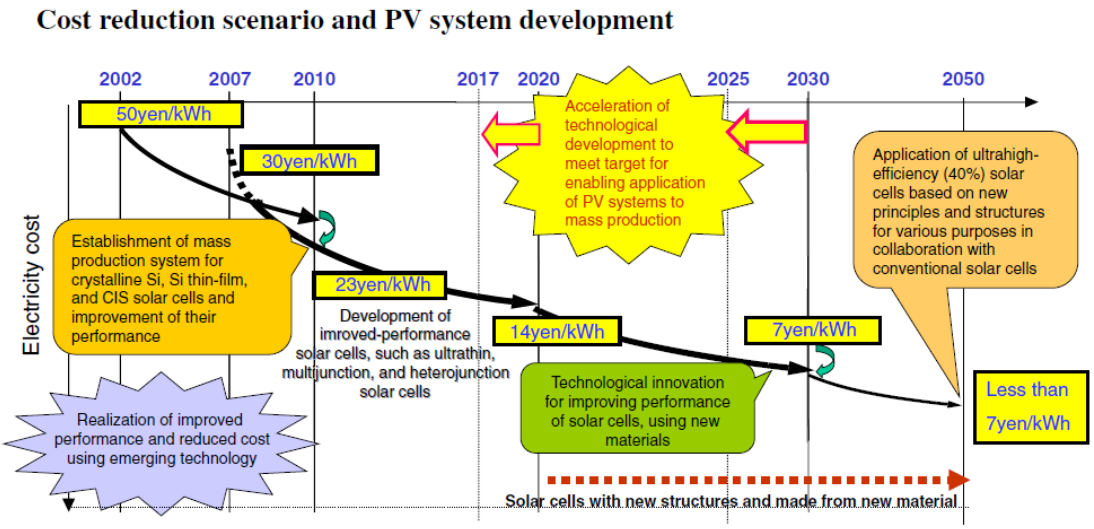

Fig. 1-5 Cost reduction scenario and PV system development in PV2030+[11].

Type	Present status		2017		2025				2050
	Module (%)	Cell (%)	Module (%)	Cell (%)	Module (%)	Cell (%)	Manufacturing cost (Yen/W)	Life time (Year)	Module (%)
Crystalline Si	16	20	20	25	25	30	50	30	Ultra-high 40% efficiency solar cells (additional development)
Thin-film Si	12	15	14	18	18	20	40	30	
CIS	15	20	18	25	25	30	50	30	
Compound	28	40	35	45	40	50	50	30	
Dye-sensitized	8	12	10	15	15	18	<40		
Organic		7	10	12	15	15	<40		

Table 1-1 Development targets of solar cells and modules in PV2030+[11].

As described above, accelerating PV is definitely and urgently required. Industry, government and academia are tackling the development of PV not only in Japan, but also in world wide. Therefore, PV has a promising future.

1.3 Thin-Film Silicon Solar Cells

The world photovoltaic production is mainly dominated by c-Si and poly-Si solar cells as shown in Fig. 1-6. c-Si solar cells are expected to be dominant in near future as shown in Ref [7]. However, the situation will be changed when terawatt level PV is deployed. According to Ref [12], Si material itself is abundant, but the shortage of silver limit the production of terawatt level. CdTe and CIGS are suffered from the shortage of tellurium and indium respectively. On the other hand, thin-film silicon solar cells and dye sensitized thin-film solar cells have capability of fabricating a few tenth of

terawatt if ITO is avoided. Therefore, thin-film silicon solar cells are promising candidate for terawatt level deployment.

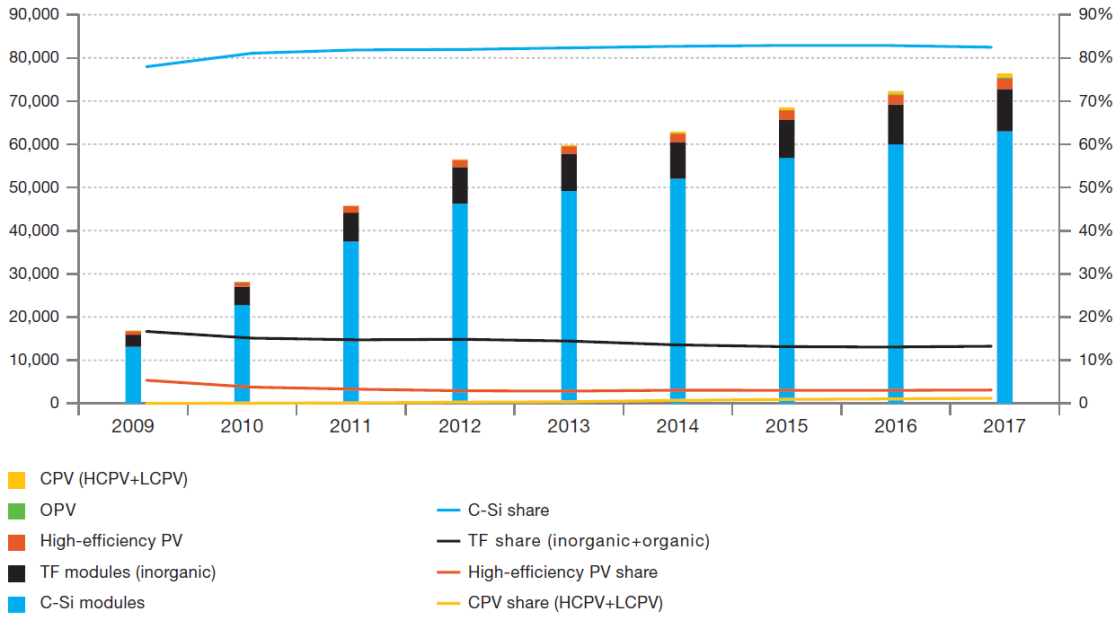

Fig. 1-6 PV modules production capacity until 2017 (MW; %)[7]

However at this moment, the conversion efficiency of thin-film silicon solar cells is still too poor compared to other types of solar cells. The module efficiency of thin-film silicon solar cells is still in the range of 11-13%, whereas the module efficiency for c-Si module is about 20% or more. In order to accelerate the deployment of thin-film silicon solar cells, a remarkable efficiency improvement is needed.

Recently, a multi-junction structure is considered as a promising candidate for the efficiency improvement in thin-film silicon solar cells. This multi-junction structure consists of two or more p-i-n diodes. These solar cells are called tandem or triple solar cells for two or three p-i-n diodes, respectively. For a tandem cell, the p-i-n diode located at the light incident side is usually called as the top cell, and the other diode is

called as the bottom cell. Materials with different band gaps are generally used for each sub-cell. The band gap of the top cell is selected to be wider than that of the bottom cell to utilize the sunlight more effectively. At present, hydrogenated amorphous silicon (a-Si:H) and hydrogenated microcrystalline silicon (μc-Si:H) are employed as materials for tandem cells, and an efficiency of 12.3-13.4% (stabilized efficiency) has been obtained at the research level as shown in Table 1-2.

However, this conversion efficiency is still too low compared to the efficiency targeted in PV2030+ roadmap as previously shown in Table 1-1. A triple junction structure has to be utilized to achieve the final goal of efficiency of 20%. As the structures of cells are changed from a-Si:H single junction to tandem and triple junction, the requirements for TCO substrates are also changed. In the next section, the requirements for TCO are reviewed.

Solar Cell	Eff. (%)	J_{sc} (mA/ cm^2)	V_{oc} (V)	FF (%)	Area (cm^2)	State	Description	Test center (Date: mm/yy)	Ref
Single-junction									
a-Si	10.1	16.75	0.886	67.8	1.036	Stab.	Oerlikon	NREL (07/09)	[13]
μc-Si	10.8	28.24	0.523	73.2	1.045	-	AIST	AIST (09/13)	[14]
Double junction									
a-Si/μc-Si	12.3	12.93	1.365	69.4	0.962	Stab.	Kaneka	AIST (07/11)	
Triple junction									
a-Si/μc-Si/μc-Si	13.4	9.52	1.963	71.9	1.006	Stab.	LGE	NREL (07/12)	[15]

Table 1-2 Present status of conversion efficiency of thin-film silicon solar cells[16].

1.4 Functions of Transparent Conductive Oxide (TCO) for Thin-Film Silicon Solar Cells

Fig. 1-7 shows the schematic of thin-film silicon solar cell. In this thesis, we focus on p-i-n structure (superstrate-type configuration). In p-i-n structure, TCO film is on transparent substrates (glass or film). When light is illuminated, photons are absorbed by the semiconductor material, and pairs of free electrons and holes are generated. The pairs are separated by the internal electric field created by p-i-n structure. Because electrons and holes have charge with opposite polarity, electrons and holes are moved to opposite direction by the internal electric field. Then, the electrons move the metal electrode, and the holes move to TCO. TCO and metal electrode have low resistance so that electrons and holes can be extracted to outside. If the sheet resistance

of TCO or metal electrode is too high, energy dissipated inside the electrode as Joule heat. Therefore, low sheet resistance is required to minimize the loss.

From the viewpoint of optical properties, reflection at interfaces (air/glass, glass/TCO, and TCO/p-a-Si:H) must be low, and the absorption of TCO film must be low. And TCO substrate must have light scattering capability in order to absorb light effectively in i-layer.

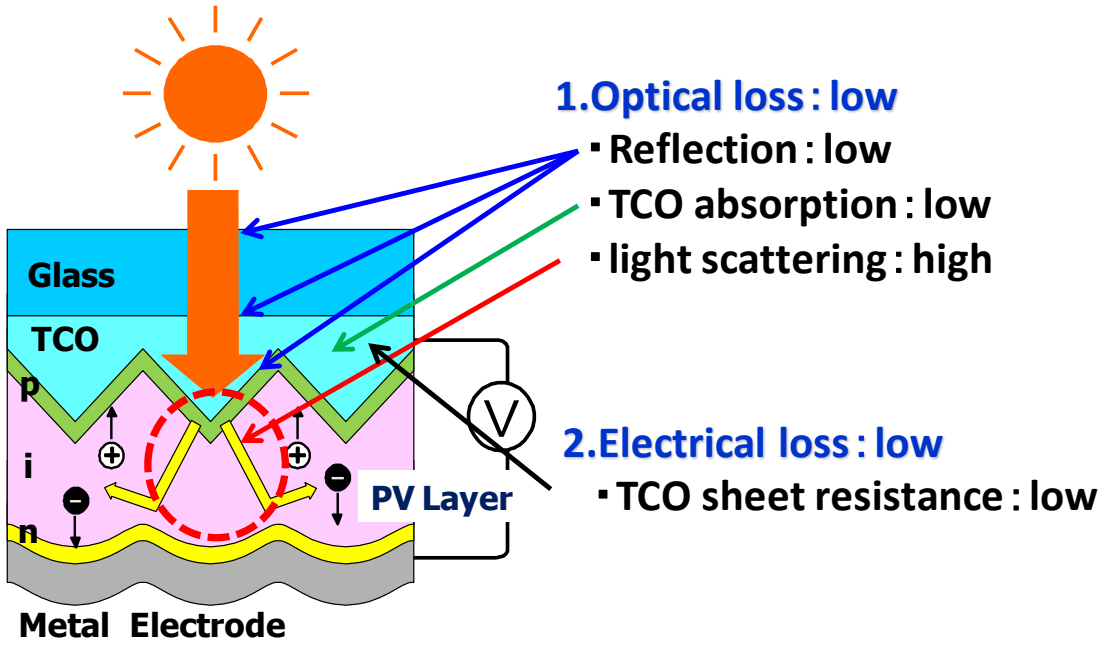

Fig. 1-7 Schematic of thin-film silicon solar cell.

To improve cell efficiency, tandem and triple junction structures are effective. Yunaz et al. performed a theoretical analysis of triple junction. They reported the possibility of achieving efficiency of over 20% as shown in Fig. 1-8. However, the highest stabilized efficiency of thin-film silicon solar cells is 13.4% with a-Si/μc-Si/μc-Si[15]. There is still large gap between the theoretical value and the actual value, and there should be a room to improve the efficiency.

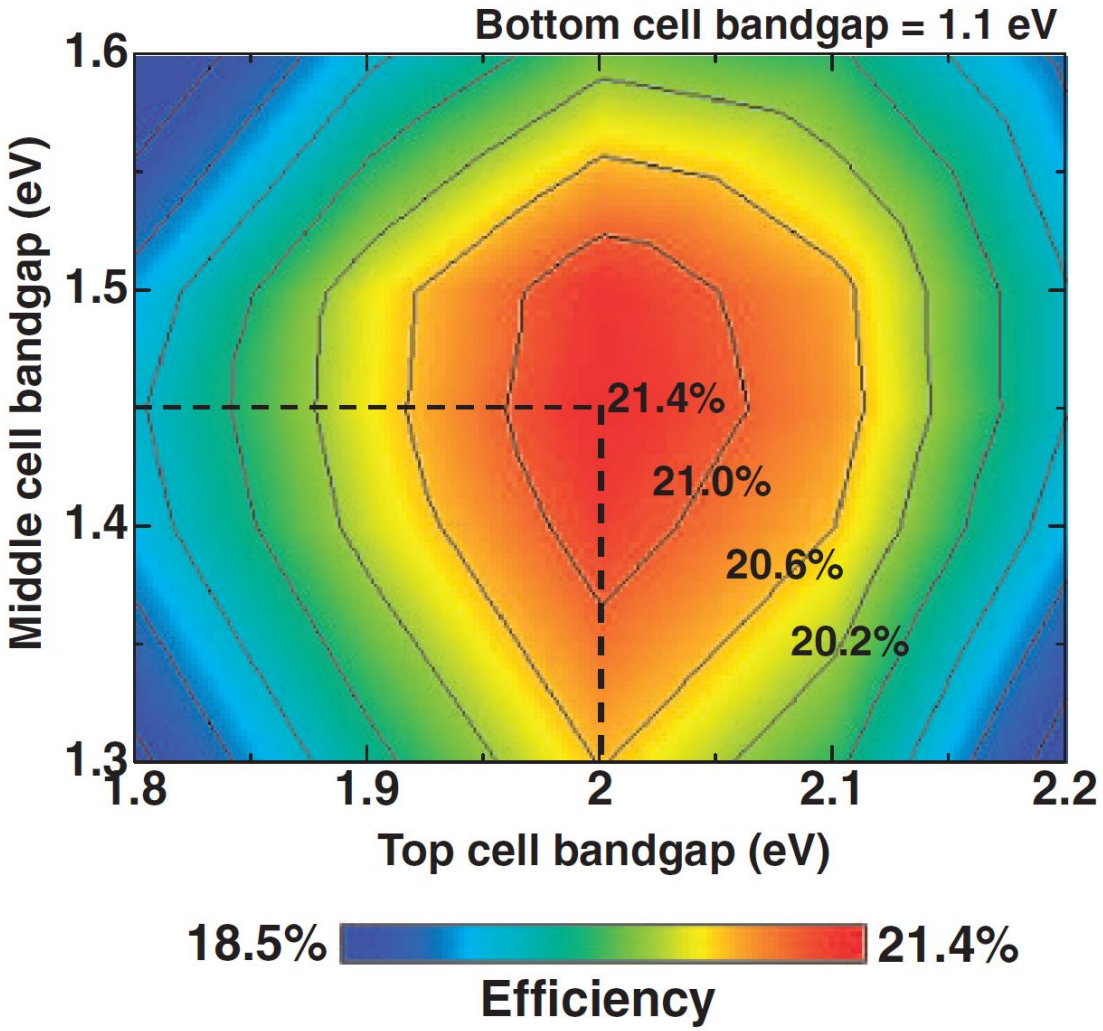

Fig. 1-8 Contour map of calculated efficiency of triple junction cell as a function of i-top and i-middle layer bandgaps. The bandgap of i-bottom layer was assumed to be 1.1 eV. (Ref [17])

In case of a-Si:H single junction solar cell, sun light with wavelength longer than around 800 nm is not absorbed in i-a-Si:H layer. In the tandem and triple junction structures, sun light in near infrared (NIR) region in addition to the visible light region is utilized. Therefore, the requirement for TCO substrates should be fulfilled in both visible light region and NIR region.

1.5 Objectives

As described above, TCO must have both low sheet resistance and high transparency in wide wavelength range. For achieving these properties, the key is to improve the mobility of free carriers.

The first object is to improve the mobility of SnO_2:F substrates, which is commercially and widely used for fabricating thin-film silicon solar cells.

The second object is to give high light scattering capability to the TCO substrates while maintaining the high mobility.

1.6 Outline

The organization of this thesis is summarized in Fig. 1-9. As shown in the figure, this thesis consists of 7 chapters. As the introduction, motivations and objectives of this study are given in this chapter.

In Chapter 2, the fundamental properties of transparent conductive oxide (TCO) are introduced. And the requirements of TCO substrates for thin-film silicon solar cells are explained.

In Chapter 3, the experimental study for improving the mobility of SnO_2:F films using Low Pressure Chemical Vapor Deposition (LPCVD) is reported. We analyzed the dependency of the mobility and the crystalline orientation of SnO_2:F on the deposition temperature, and find one method to improve mobility by introducing

temperature gradient.

In Chapter 4, the study of scattering mechanisms in SnO_2:F films is reported. It is important to understand what scattering mechanisms are dominant in SnO_2:F films. We compared the experimental values and the theoretical values, and we identified that grain barrier scattering is dominant in the range of carrier concentration $10^{18} \sim 10^{19}$ cm^{-3}, and ionized impurity scattering is dominant in the range of carrier concentration above 10^{20} cm^{-3}. We confirmed this difference by changing grain size by experiment.

In Chapter 5, we have succeeded to fabricate SnO_2:F substrates with both very high haze and high mobility. In order to obtain high haze, we deposited SnO_2:F films on the glass whose surface was roughened by reactive ion etching (RIE) technique. It is so-called "W-textured" TCO. We will show the properties of TCO substrates and the cell evaluation results.

In Chapter 6, we proposed new method of measuring transmittance of W-textured TCO. While developing the W-textured TCO, we found that the optical transmittance of W-textured TCO can't be measured accurately by conventional method. Therefore, we adopted new configuration of measuring optical properties, and we confirmed that the transmittance measured by the new method has good correlation with EQE, while the transmittance measured with the conventional method doesn't have correlation.

Chapter 7 concludes this study by providing a brief summary and giving future prospects.

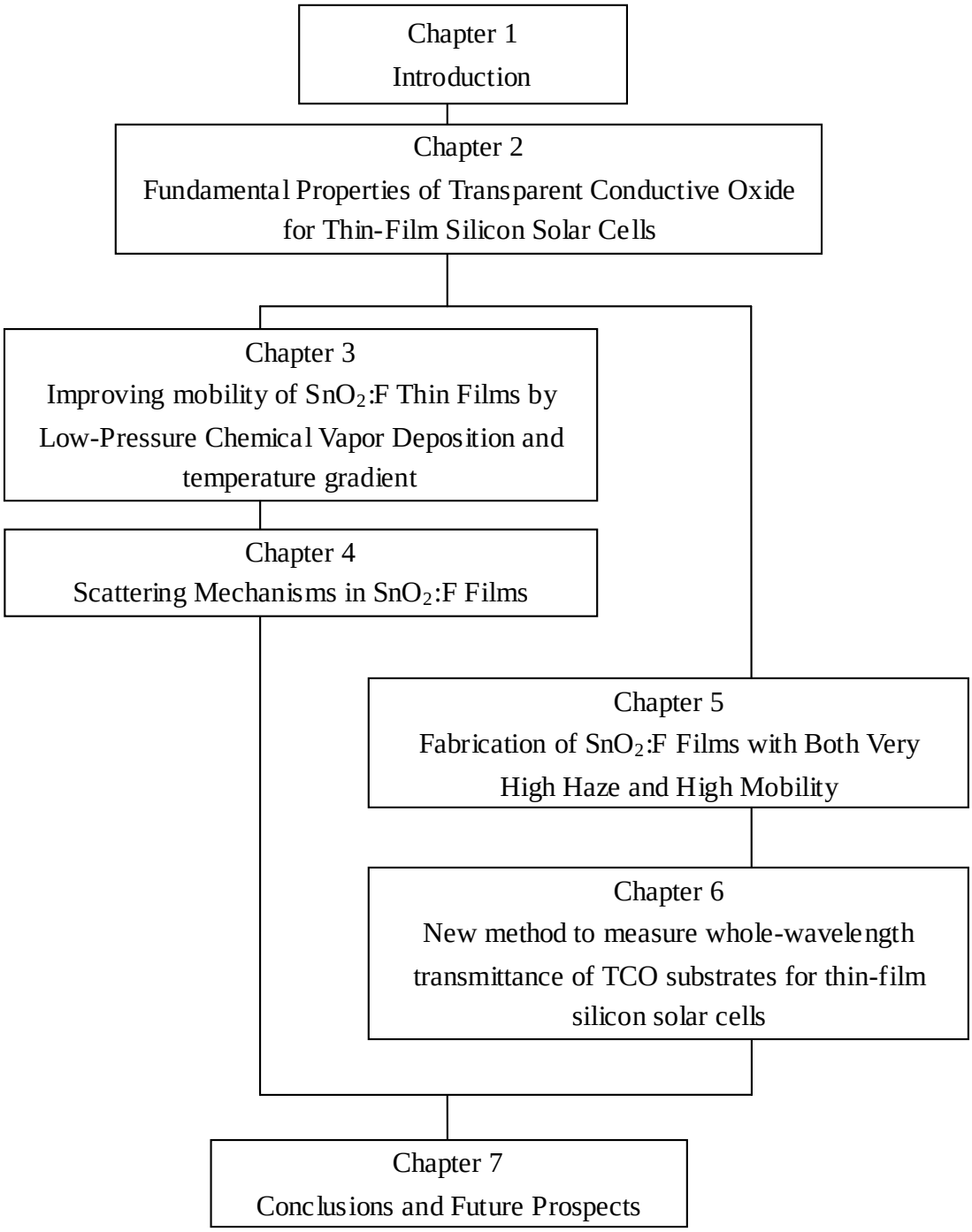

Fig. 1-9 Outline of this thesis.

References

[1] Stocker, T.F., D. Qin, G.-K. Plattner, M. Tignor, S. K. Allen, J. Boschung, A. Nauels, Y. Xia, V. Bex, and P. M. Midgley, "IPCC, 2013: Summary for Policymakers.," in *Climate Change 2013: The Physical Science Basis. Contribution of Working Group I to the Fifth Assessment Report of the Intergovernmental Panel on Climate Change*, Cambridge, United Kingdom and New York, NY, USA.: Cambridge University Press, 2013.

[2] *IPCC, 2014: Summary for policy makers, In Climate Change 2014: Impacts, Adaptation, and Vulnerability. Contribution of Working Group II to the Fifth Assessment Report of the Intergovernmental Panel on Climate Change*, no. March. 2014, pp. 1–44.

[3] Edenhofer, B. O., R. Pichs-Madruga, Y. Sokona, E. Farahani, S. Kadner, K. Seyboth, A. Adler, I. Baum, S. Brunner, P. Eickemeier, and T. Z. and J. C. M. (eds. . Kriemann, J. Savolainen, S. Schlömer, C. von Stechow, *IPCC, 2014: Summary for Policymakers, In: Climate Change 2014, Mitigation of Climate Change. Contribution of Working Group III to the Fifth Assessment Report of the Intergovernmental Panel on Climate Change*. Cambridge, United Kingdom and New York, NY, USA.: Cambridge University Press.

[4] F. R. Rijsberman, "Targets and Indicators of Climatic Change," in *AGGG-WG2 Review Workshop*, 1990.

[5] C. C. Jaeger and J. Jaeger, “Three views of two degrees,” *Reg. Environ. Chang.*, vol. 11, no. S1, pp. 15–26, Dec. 2010.

[6] UNFCCC. Conference of the Parties(COP), “Report of the Conference of the Parties on its sixteenth session, held in Cancun from 29 November to 10 December 2010. Addendum. Part two: Action taken by the Conference of the Parties at its sixteenth session.,” no. March. 2011.

[7] European Photovoltaic Industry Association (EPIA), “GLOBAL MARKET OUTLOOK.” 2013.

[8] “Research Center for Photovoltaic Technologies (RCPVT) in The National Institute of Advanced Industrial Science and Technology (AIST).” [Online]. Available: https://unit.aist.go.jp/rcpvt/ci/about_pv/e_source/RE-energypayback.html.

[9] M. Brower, D. Green, R. Hinrichs-rahlwes, S. Sawyer, M. Sander, R. Taylor, I. Giner-reichl, S. Teske, H. Lehmann, M. Alers, and D. Hales, “Renewables 2014 Global Status Report,” Paris, 2014.

[10] NEDO, “PV roadmap 2030,” 2004. [Online]. Available: http://www.nedo.go.jp/content/100086787.pdf.

[11] NEDO, “PV Roadmap 2030+,” 2009. [Online]. Available: http://www.nedo.go.jp/library/pv2030_index.html.

[12] A. Feltrin and A. Freundlich, “Material considerations for terawatt level deployment of photovoltaics,” *Renew. Energy*, vol. 33, no. 2, pp. 180–185, Feb. 2008.

[13] S. Benagli, D. Borrello, E. Vallat-Sauvain, J. Meier, U. Kroll, J. Hötzel, J. Spitznagel, J. Steinhauser, L. Castens, and Y. Djeridane, “High-efficiency amorphous silicon devices on LPCVD-ZNO TCO prepared in industrial KAI-M R&D reactor,” in *24th European Photovoltaic Solar Energy Conference*, 2009.

[14] H. Sai, K. Saito, N. Hozuki, and M. Kondo, “Relationship between the cell thickness and the optimum period of textured back reflectors in thin-film microcrystalline silicon solar cells,” *Appl. Phys. Lett.*, vol. 102, p. 053509, 2013.

[15] S. Kim, J.-W. Chung, H. H.-M. Lee, J. Park, and Y. Heo, “Remarkable progress in thin-film silicon solar cells using high-efficiency triple-junction technology,” *Sol. Energy Mater. Sol. Cells*, vol. 119, pp. 26–35, Dec. 2013.

[16] M. A. Green, K. Emery, Y. Hishikawa, W. Warta, and E. D. Dunlop, “Solar cell efficiency tables (version 43),” *Prog. Photovoltaics Res. Appl.*, vol. 22, no. 1, pp. 1–9, Jan. 2014.

[17] I. A. Yunaz, A. Yamada, and M. Konagai, “Theoretical Analysis of Amorphous Silicon Alloy Based Triple Junction Solar Cells,” *Jpn. J. Appl. Phys.*, vol. 46, no. No. 47, pp. L1152–L1154, Nov. 2007.

Chapter 2

2 Fundamental Properties of Transparent Conductive Oxide for Thin-Film Silicon Solar Cells

2.1 Introduction

Transparent Conductive Oxide (TCO) is unique materials which have both high transparency and high electrical conductivity. TCO is very important material for various solar cells, flat panel displays, and low emissivity windows. In this chapter, basic properties of TCO materials, typical deposition method, and typical materials are reviewed.

2.2 Properties of Transparent Conductive Oxide (TCO) Materials

2.2.1 Electrical Properties

In order to have high conductivity, the required conditions are (1) the existence of carriers which bring charge, and (2) the path where the carriers can move easily inside the TCO materials. These conditions are expressed in the formula of conductivity.

$$\sigma = ne\mu_n + pe\mu_p \quad (2\text{-}1)$$

where n, p, e, μ_n, and μ_p are electron carrier concentration, hole carrier concentration, electron charge, electron mobility, and hole mobility. For condition (1),

n or p need to be high enough. For condition (2), μ_n or μ_p need to be high enough. As described later, TCO material should have a wide band gap in order to keep transparency in the visible light region. In wide band gap semiconductors, few carriers are excited from the valence band to the conduction band, because thermal energy at room temperature is 30 meV, which is much smaller compared to the band gap around 3eV. Therefore, dopant materials are doped to generate carriers from donor levels near the conduction band edge (or acceptor levels near the valence band edge). The donor (acceptor) levels are formed with some defects, including point defects, line defects, and plane defects.

Kröger-Vink expression is used to describe the status of point defects in ionic crystals as A_B^C. A is chemical element or "V" (Vacancy) in the point concerned. B is the chemical element if there is no defect. C expresses the charge. [.] means the increment of 1 electron charge, ['] means the decrement of 1 electron charge. For example, if Mg^{2+} Al^{3+}, or K^+ is in Ca^{2+} site in CaO crystal (Ca^{2+} O^{2-}), the expressions are Mg_{Ca} , $Al_{Ca}^{\cdot}$, or K_{Ca}'. Example of Kröger-Vink expression and the ionic valence are shown in Fig. 2-1

Ca_{Ca}	O_O	Ca_{Ca}	O_O	Ca_{Ca}		Ca^{2+}	O^{2-}	Ca^{2+}	O^{2-}	Ca^{2+}
O_O	$Al_{Ca}^{\cdot}$	O_O	Mg_{Ca}	O_O		O^{2-}	Al^{3+}	O^{2-}	Mg^{2+}	O^{2-}
Ca_{Ca}	O_O	K_{Ca}'	O_O	Ca_{Ca}		Ca^{2+}	O^{2-}	K^+	O^{2-}	Ca^{2+}
O_O	Ca_{Ca}	O_O	Ca_{Ca}	O_O		O^{2-}	Ca^{2+}	O^{2-}	Ca^{2+}	O^{2-}
Ca_{Ca}	O_O	Ca_{Ca}	O_O	Ca_{Ca}		Ca^{2+}	O^{2-}	Ca^{2+}	O^{2-}	Ca^{2+}
	(a)							(b)		

Fig. 2-1 Example of Kröger-Vink expression and the ionic valence of CaO crystal.

As the example of TCO materials, carrier generation in SnO_2 is described. In

case of SnO_2, Cl and F are doped into O site, and Sb and As are doped into Sn site. Then electron carriers are excited from the site as eq.(2-2), for example.

$$\begin{aligned} F_O &\rightarrow F_O^{\cdot} + e' \\ Sb_{Sn} &\rightarrow Sb_{Sn}^{\cdot} + e' \end{aligned} \tag{2-2}$$

Because resistivity of SnO_2 changes by reducing and oxidizing, vacancy of oxygen is also an important source of carriers. Carriers are generated as eq.(2-3).

$$\begin{aligned} O_O &\rightarrow V_O + \frac{1}{2} O_2(g) \\ V_O &\rightarrow V_O^{\cdot\cdot} + 2e' \end{aligned} \tag{2-3}$$

As described above, 1 electron carrier is generated by 1 dopant atom, and 2 electron carriers are generated by 1 oxygen vacancy.

In order to increase n or p, donor or acceptor materials are doped into the base materials. In case of n-type TCO, donor atoms are doped and electron free carriers are generated in the conduction band. In case of p-type TCO, acceptor atoms are doped and hole free carriers are generated in the valence band. Hole and electron move in different bands, so the characteristics of n-type and p-type are different.

TCO is degenerated semiconductor. Fermi level is shifted into the conduction band in the case of n-type (the valence band in the case of p-type). Currently, most TCOs are n-type, for example, SnO_2, In_2O_3, ZnO, Ga_2O_3, and CdO. The valence band is formed with occupied 2p orbital of oxygen, and the conduction band is mainly formed with unoccupied s orbital of positive ion. Generally, s orbital with $(n-1)d^{10}ns^0$ ($n \geq 4$, n is principal quantum number) expands widely and isotropically, so, the s orbital of neighbor positive ions have large overlap, and it results to form the conduction band with large dispersion[1]. Therefore, electron carriers can move easily through the overlap of s orbital. Effective mass is defined as

$$m^* = \left[\left(\frac{2\pi}{h}\right)^2 \frac{\partial^2 E}{\partial k^2}\right]^{-1} \quad (2\text{-}4)$$

Large dispersion means large $\frac{\partial^2 E}{\partial k^2}$. So, this leads to smaller effective mass. Actually, effective mass of electron of SnO_2, In_2O_3, and ZnO are small (Reported as 0.275, 0.35, and 0.28, respectively[2]).

On the other hand, doping hole is not easy. As described above, the valence band is formed with 2p orbital of oxygen. This orbital has nonbonding characteristics. Therefore, the 2p orbital has small overlap with orbital of neighbor atoms. If hole is doped, this hole can't move. That's why there is few p-type TCO. Recently, a few kind of p-type TCO have been developed[3]–[6]. But in this thesis, we will focus on the conventional n-type TCO. Therefore, we will neglect the contribution of holes and eq.(2-1) are changed to $\sigma = ne\mu$, where μ is the mobility of electrons.

2.2.2 Optical Properties

"Transparent" usually means transparency for visible light. Visible light is around 380 ~ 780 nm in wavelength, and 1.6 ~ 3.3 eV in energy. Therefore, TCO materials are basically required to have band gap larger than 3.3 eV. Generally, band gap tend to be larger as the atoms are ionic bonded. Oxides and halides have this character. So, most TCO materials are oxides.

As described in the previous subsection, TCO is degenerately doped in order to increase carrier concentration. The high concentration of free carriers affects the transparency of TCO. Drude model can simulate the optical properties of free carriers well[7], [8] In this model, free carriers are assumed to oscillate in response to the electric field. The equation of motion of the oscillating electron is shown as eq.(2-5)

$$m^* \frac{d^2x}{dt^2} + \frac{m^*}{\tau}\frac{dx}{dt} = -eE(t) \tag{2-5}$$

where m^*, τ, e, E, and x are effective mass of free carrier, relaxation time of free carriers, electron charge, applied electric field, and the displacement of free carrier. By solving eq.(2-5), eq.(2-6) are obtained.

$$\begin{aligned} x &= \frac{eE}{m^*}\frac{1}{\omega^2 + i\frac{\omega}{\tau}} \\ v &= \frac{dx}{dt} = \frac{eE}{m^*}\frac{-i\omega}{\omega^2 + i\frac{\omega}{\tau}} \\ J &= -nev = \frac{ne^2E}{m^*}\frac{i\omega}{\omega^2 + i\frac{\omega}{\tau}} \\ \sigma &= \frac{J}{E} = \frac{ne^2}{m^*}\frac{i\omega}{\omega^2 + i\frac{\omega}{\tau}} \end{aligned} \tag{2-6}$$

where n, J, and σ are free carrier concentration, current density, and frequency dependent conductivity. This yields DC conductivity $\sigma_0 = \frac{ne^2\tau}{m^*}$ by substituting $\omega = 0$. Electric polarization P (average dipole moment per unit volume) due to the displacement of free carriers is described as eq.(2-7).

$$P = -nex = \frac{ne^2E}{m^*}\frac{-1}{\omega^2 + i\frac{\omega}{\tau}} \tag{2-7}$$

Electric flux density, permittivity $\varepsilon_1 - i\varepsilon_2$ are described as eq.(2-8),(2-9).

$$D = (\varepsilon_1 - i\varepsilon_2)E = \varepsilon_\infty\varepsilon_0 E + P = \left(\varepsilon_\infty\varepsilon_0 - \frac{ne^2}{m^*}\frac{1}{\omega^2 + i\frac{\omega}{\tau}}\right)E \tag{2-8}$$

$$\varepsilon_1 = \varepsilon_\infty\left(1 - \frac{{\omega_p}^2}{\omega^2 + \frac{1}{\tau^2}}\right), \varepsilon_2 = \frac{\varepsilon_\infty{\omega_p}^2}{\omega\tau\left(\omega^2 + \frac{1}{\tau^2}\right)} \tag{2-9}$$

where $\omega_p = \sqrt{\frac{e^2 n}{\varepsilon_\infty \varepsilon_0 m^*}}$ and ε_∞ are plasma frequency and high-frequency permittivity. ε_∞ is the permittivity with high frequency where free carrier and lattice vibration cannot respond. Therefore, ε_∞ is including the effect of band to band transition. ε_∞ is sometimes called as optical permittivity, because it usually corresponds the permittivity in the visible light wavelength region, and $\varepsilon_\infty \sim n^2$ in case of TCO materials. Calculated transmittance, reflectance, and absorption of free carriers are shown Fig. 2-2, with different carrier concentration. Absorption becomes larger towered the plasma frequency where absorption show peaks. As carrier concentration becomes higher, the absorption in the visible to NIR region becomes larger. Therefore, carrier concentration should be as low as possible in order to suppress absorption. In order to keep resistivity low with low carrier concentration, high mobility is required.

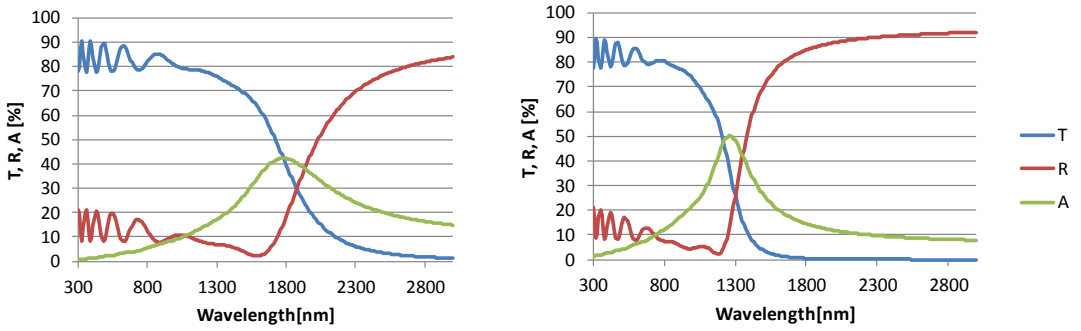

(a) (b)

Fig. 2-2 Calculated transmittance, reflectance, and absorption of free carriers by Drude model. Parameters are $\mu = 50\ \mathrm{cm^2/Vs}$, $m^* = 0.4$, $\varepsilon_\infty = 4$, and thickness=500 nm. The difference of (a) and (b) is (a) $n = 5\mathrm{x}10^{20}\ \mathrm{cm^{-3}}$ and (b) $n = 1\mathrm{x}10^{21}\ \mathrm{cm^{-3}}$. Corresponding plasma frequency are (a) 0.66 eV (1.9 μm) and (b) 0.93 eV (1.3μm).

Fig. 2-3 shows simulation results of free carrier absorption by fixing sheet

resistance to 12Ω/□. In Fig. 2-3(a), mobility μ is fixed to 80 cm^2/Vs, carrier concentration n and thickness d are varied. In Fig. 2-3(b), carrier concentration n is fixed to $1x10^{20}$ cm^{-3}, mobility μ and thickness d are varied. From Fig. 2-3 (a), the absorption is almost the same in various carrier concentrations if the mobility and the product of carrier concentration and film thickness $(n \times d)$ are fixed. From Fig. 2-3(b), the absorption becomes higher rapidly as mobility decreases. So, higher mobility is very important to achieve lower absorption, especially in the near-infrared region. In this study, we set our target of mobility as $80cm^2/Vs$.

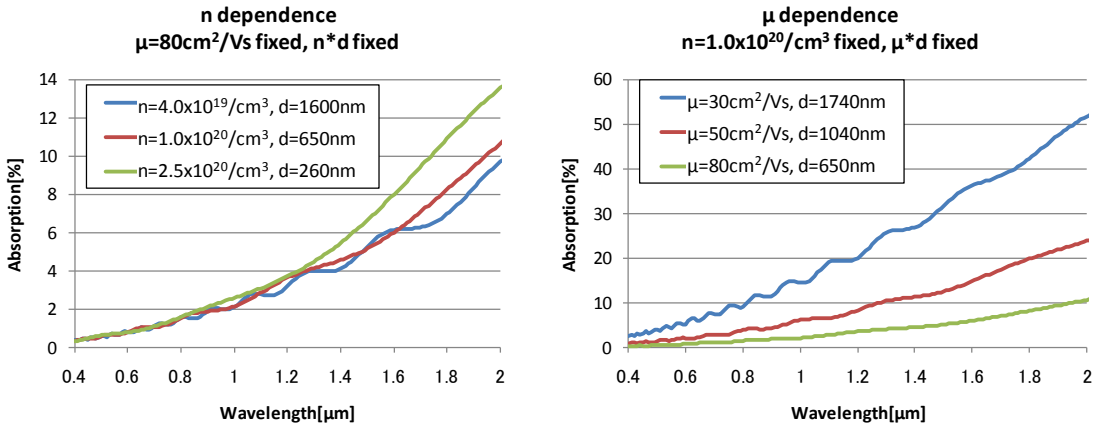

(a) (b)

Fig. 2-3: (a) n dependence. μ is fixed. $(n \times d)$ is fixed constant. (b) μ dependence. n is fixed. So, $(\mu \times d)$ is fixed.

Light trapping is very important function for thin-film silicon solar cells [9]. Haze ratio is considered to one measure of light trapping capability. In case of TCO films fabricated by Chemical Vapor Deposition (CVD), surface textures adequate for thin-film silicon solar cells are formed[10], [11], and films with high haze can be obtained. In case of TCO films deposited by sputtering, surface are flat and haze ratio is

low. In that case, additional processes (ex. etching ZnO films) are adopted to increase haze ratio[12]. For very high haze, the technique combined with reactive ion etched glass substrates and MOCVD ZnO:B was reported[13]. It is so-called "W-textured" TCO. Fig. 2-4 shows the spectral haze of W-textured ZnO:B. By adopting RIE etched glass substrates, haze ratio is drastically increased. By this technique, haze ratio in visible wavelength region can be fabricated to be high enough.

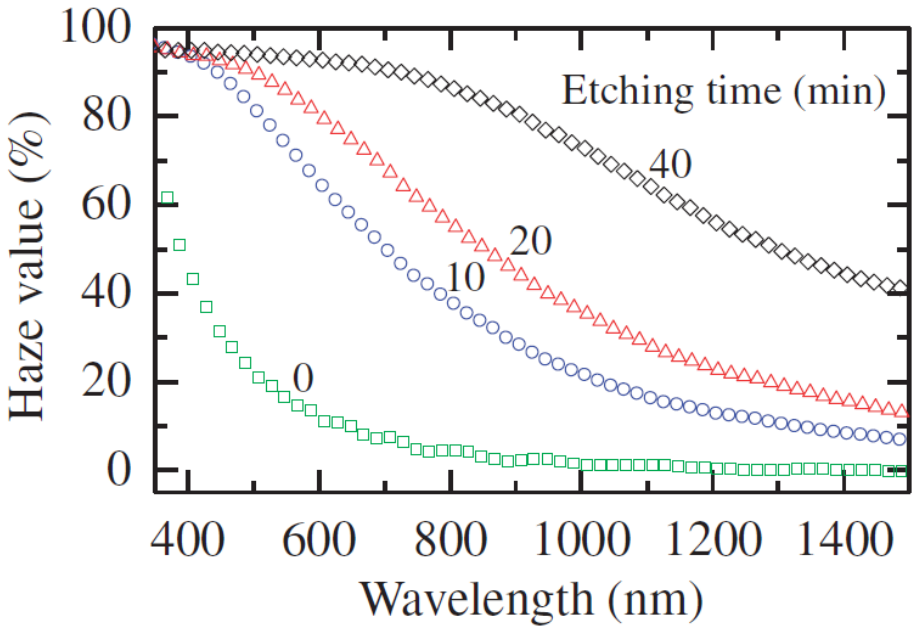

Fig. 2-4 Spectral haze ratio of W-textured ZnO:B. ([13] Copyright 2010 The Japan Society of Applied Physics.)

As explained in Chapter 1, high transparency and high haze ratio in NIR region is important for tandem or triple junction thin-film silicon solar cells. Therefore, we need to achieve high mobility and high haze ratio simultaneously. We set our target of mobility as 80cm^2/Vs, and that of haze ratio as 90% at wavelength 1000 nm.

2.3 Film Deposition Methods

Film deposition methods (here, Vapor deposition method only) can be categorized to Physical Vapor Deposition (PVD) and Chemical Vapor Deposition (CVD)[14]. These method are reviewed in this section.

2.3.1 Physical Vapor Deposition

In PVD, the source materials are changed to atomic or molecular species by adding energy, and these species are condensed on substrates. The temperature of substrates is lower than the temperature of the atomic or molecular spices, and the spices are cooled rapidly on the substrates. Therefore, PVD process is considered to be non-equilibrium process. PVD is usually categorized to Evaporation, Sputtering, and Ion-Plating methods.

Evaporation is a process that source materials are evaporated by heating and the evaporated materials are attached to the substrates. The methods of heating are resistance heating, electron beam (EB) heating, pulsed laser heating (PLD), etc.

Sputtering is a process that atoms are ejected from a solid target material due to bombardment of the target by ionized noble gas (typically, Ar+). The ejected atoms are attached to the substrates nearby. Using ceramic target, film with the same composition as the target can be fabricated. By using metal target and adding O_2, N_2, or CO_2, oxides, nitrides, or carbide can be fabricated. Sputtering can be adopted for a wide variety of materials.

In Ion plating, the coating material is vaporized and ionized by an electric arc, then accelerated to high speed towards the substrates. By utilizing the chemical activity

of the ions, some chemical reaction or creation of atomic bond is promoted.

2.3.2 Chemical Vapor Deposition

In the CVD process, the source materials are vaporized and these gases are chemically reacted on the surface of the heated substrates, then films are deposited on the substrates. In this method, the temperature of gases is lower than that of the substrate. When gases reached on the substrates, the gases are heated to the temperature of the substrates. Therefore, the deposition process is considered to be thermally equilibrium. CVD process is categorized to Atmospheric Pressure CVD (APCVD), Low Pressure CVD, Plasma Enhanced CVD (PECVD), etc. Various kinds of films can be deposited, for example, semiconductor films (Si, GaAs, etc), dielectric films (SiO_2, Si_3N_4, etc), metal films (W, Ti, Mo, etc), and metal compounds (TiN, SnO_2, etc).

APCVD is the most common CVD process. The chamber pressure is kept as 1 atm. Source gases are introduces to the camber with carrier gases (N_2, Ar, H_2, He, etc). In case of TCO, APCVD is industrially used for fabricating SnO_2:F, and SnO_2:Sb.

In LPCVD, the chamber pressure is kept at 10^2~10^4 Pa. It has the advantages that thickness uniformity and purity of films are better. If Metal-Organic (MO) material is used as source material, it is called as Metal Organic CVD (MOCVD). In case of TCO, MOCVD is used for fabricating ZnO:B in industrial and research fields. Compared to APCVD, LPCVD has the advantages of the excellent uniformity of thickness and purity[15].

In PECVD, the temperature of the substrates is kept to low, so that source materials can't receive enough energy from the substrates. Instead the substrate heating, plasma is introduced into the gases. PECVD is not used for TCO, but it is widely used

for fabricating thin-film silicon films.

2.4 Transparent Conductive Oxide Materials

2.4.1 Tin Oxide (SnO_2)

SnO_2 is widely used for low emission window coatings, thin film solar cells, gas sensors, etc due to its high stability.

SnO_2 has the rutile crystal structure as shown in Fig. 2-5. The structure has a tetragonal unit cell ($(P4_2/mnm)$, a = b = 0.4738 nm, and c = 0.3188 nm[16].

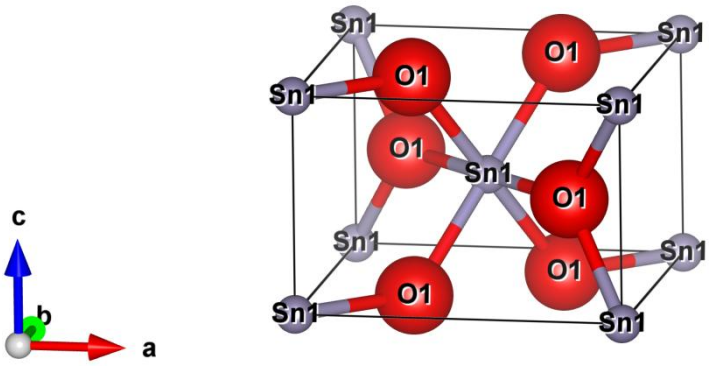

Fig. 2-5 Crystal structure of SnO_2.

Observed band gap was reported 3.57 (⊥ c) and 3.93 (∥ c) [17]. Band structure calculation shows that the high dispersion of the density states near the conduction band edge, formed with 5s orbital of Sn atoms. This high dispersion indicates a low conduction effective mass, in other words, a high electron mobility. Calculated effective masses are reported as 0.26 (⊥ c) and 0.20 (∥ c) [18]. These values agree with experimental value. This can be understood that c-axis is shorter than a- and b-axis, overlap of Sn 5s orbital is large for c-axis direction.

For dopants, F[10], Sb[19], Ta[20], W[21], etc are used. SnO_2 is fabricated by

RF magnetron sputtering, reactive DC sputtering, APCVD, LPCVD, electron beam (EB) evaporation, spray coating, etc.

2.4.2 Indium Oxide

Sn doped In_2O_3 (ITO) is a critical component for flat panel display devices, touch panels, etc for its high transmittance, high conductivity, and good etching ability.

In_2O_3 has two different crystal structures. One is cubic, the other is hexagonal. In most conditions, the cubic structure is formed. Crystal structure of the cubic is shown in Fig. 2-6. Lattice constant is 1.0118 nm. Inside one unit cell, 32 In atoms and 48 O atoms are included.

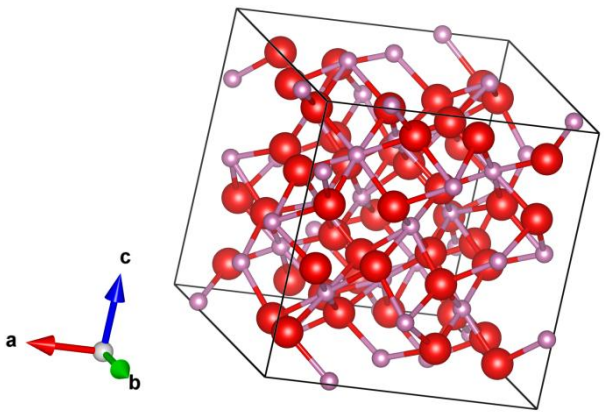

Fig. 2-6 Crystal structure of In_2O_3. Small balls are In, and large balls are O.

In_2O_3 has band gap of 3.75 eV[22]. The conduction band is formed with 5s orbital of In atoms, and the valence band is formed with 2p orbital of O atoms[23], [24]. Sn is the most widely used for dopant. But various dopants (Ti[25], W[26], [27], Zr[28], H[29], etc) are reported. In_2O_3 films are fabricated by RF magnetron sputtering, EB evaporation.

2.4.3 Zinc Oxide

ZnO has been used for various purpose, such as white paints, green phosphors for display, surface-acoustic wave (SAW) devices, sensors, varistor, etc. As TCO, ZnO is used to thin film silicon solar cells and CIGS solar cells.

ZnO has the hexagonal wurtzite structure. Lattice constants are a = 0.32498 nm, c = 0.52066 nm. Crystal structure of ZnO is shown in Fig. 2-7.

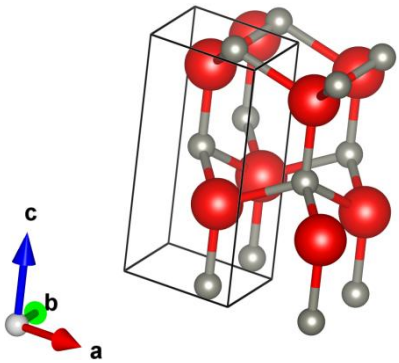

Fig. 2-7 Crystal structure of ZnO.

ZnO is a direct semiconductor with a band gap energy of 3.4 eV. The top of the valence band is formed with 2p orbital of oxygen. The bottom of the conduction band is formed with 4s orbital of zinc[30], [31].

ZnO can be fabricated by many kinds of methods. Oxidation of evaporated metallic Zn film, Metal-organic chemical vapor deposition (MOCVD)[32], RF magnetron sputtering, Pulsed laser deposition, etc.

2.4.4 Other materials

There are many other TCO materials. Among them, CdO, Cd_2SnO_4, $CdIn_2O_4$, etc have good electric properties. For example, the resistivity of CdO are reported as $3x10^{-5}$ Ωcm, which is much smaller than other TCOs. However, these TCOs are not

used widely due to the toxicity of Cd.

2.4.5 Comparison among TCO materials

We'll compare the properties of SnO_2, In_2O_3, and ZnO from the viewpoint of the application for thin-film silicon solar cells.

Regarding to optical properties, SnO_2, In_2O_3, ZnO have wide band gap more than 3.3 eV. So, they are transparent at visible wavelength region. However, the band gap of ZnO (3.4eV) is slightly lower than SnO_2 (3.6eV) and In_2O_3 (3.75eV), and the absorption in ultra violet (UV) region of ZnO is higher than others. Recently, the study for increasing the band gap of ZnO by adding MgO into ZnO has been done[33]. This could overcome the weak point of ZnO, but it is not applied industrially yet. As described in subsection 2.2.2, high mobility is required to suppress the free carrier absorption (FCA). The reported mobility of In_2O_3-, SnO_2-, and ZnO-based materials deposited on glass substrates spread widely. In In_2O_3 based material, higher mobility than 100 cm^2/Vs are reported[29], [34]. In SnO_2 based materials, 136cm^2/Vs is reported in W-doped SnO_2 by PLD with help of $Ti_{1-x}Nb_xO_2$ undercoat[35] whose lattice constant is exactly tuned same as that of SnO_2. This value is exceptionally high in case of SnO_2 based materials. Except the report, the reported mobility of SnO_2:W and SnO_2:Ta are around 80cm^2/Vs by PLD with help of TiO_2 undercoat[20], [21]. In case of SnO_2:F, 60 cm^2/Vs is the highest mobility reported (deposited by APCVD)[36]. In ZnO based materials, 44.2 cm^2/Vs in ZnO:Al by RF sputtering[37].

Next, we'll compare the chemical stability of these TCOs. SnO_2 has high resistance to atmospheric influence, to chemical (acid, alkaline), and it has high stability up to 800°C[38]. However, it doesn't have enough durability against atomic hydrogen.

Therefore, Thin protecting layer is adopted[39][40]. ITO has low resistance to high temperature [41], to chemical (in other words, it has good etching ability), and to atomic hydrogen[9]. ZnO has good durability against atomic hydrogen, although the resistance to damp-heat test is low[42].

The other important factors are availability of materials and toxicity. Indium is a rare element and ranks 61st in abundance in the Earth's crust[43]. And Indium is suspected of inducing pulmonary fibrosis[44].

As described above, SnO_2 based materials have relatively high mobility, wide band gap, and high stability to chemicals. In this thesis, we focus on the study of SnO_2:F deposited by LPCVD.

References

[1] H. S. Randhawa, M. D. Matthews, and R. F. Bunshah, "SnO_2 films prepared by activated reactive evaporation," *Thin Solid Films*, vol. 83, no. 2, pp. 267–271, Sep. 1981.

[2] K. Ellmer, "Transparent Conductive Zinc Oxide and Its Derivatives," in *Handbook of Transparent Conductors*, D. S. Ginley, Ed. Boston, MA: Springer US, 2011, pp. 193–264.

[3] H. Kawazoe, M. Yasukawa, H. Hyodo, M. Kurita, H. Yanagi, and H. Hosono, "P-type electrical conduction in transparent thin films of $CuAlO_2$," *Nature*, vol. 389, pp. 939–942, 1997.

[4] H. Yanagi, H. Kawazoe, A. Kudo, M. Yasukawa, and H. Hosono, "Chemical design and thin film preparation of p-type conductive transparent oxides," *J. Electroceramics*, vol. 4, pp. 407–414, 2000.

[5] H. Kawazoe, H. Yanagi, K. Ueda, and H. Hosono, "Transparent p-Type Conducting Oxides: Design and Fabrication of p-n Heterojunctions," *MRS Bulletin*, vol. 25. pp. 28–36, 2000.

[6] A. N. Banerjee and K. K. Chattopadhyay, "Recent developments in the emerging field of crystalline p-type transparent conducting oxide thin films," *Prog. Cryst. Growth Charact. Mater.*, vol. 50, pp. 52–105, 2005.

[7] P. Drude, “Zur Elektronentheorie der Metalle,” *Ann. Phys.*, vol. 306, no. 3, pp. 566–613, 1900.

[8] P. Drude, “Zur Elektronentheorie der Metalle; II. Teil. Galvanomagnetische und thermomagnetische Effecte,” *Ann. Phys.*, vol. 308, no. 11, pp. 369–402, 1900.

[9] A. V. Shah, H. Schade, M. Vanecek, J. Meier, E. Vallat-Sauvain, N. Wyrsch, U. Kroll, C. Droz, and J. Bailat, “Thin-film silicon solar cell technology,” *Prog. Photovoltaics Res. Appl.*, vol. 12, no. 23, pp. 113–142, Mar. 2004.

[10] K. Sato, Y. Gotoh, Y. Hayashi, and K. Adachi, “Improvement of textured SnO_2: F TCO films for a-Si solar cells,” *Res. Lab. Asahi Glas. Co., Ltd*, 1990.

[11] A. Yamada, W. W. Wenas, M. Yoshino, M. Konagai, and K. Takahashi, “Low-resistive textured ZnO thin films grown by MOCVD and photo-MOCVD at very low-temperature of 150 degrees,” in *The Conference Record of the Twenty-Second IEEE Photovoltaic Specialists Conference - 1991*, 1991, pp. 1236–1241.

[12] H. Kuramochi, R. Akiike, H. Iigusa, K. Tamano, K. Utsumi, T. Shibutami, P. Sichanugrist, and M. Konagai, “Development of Novel Aluminum-Doped Zinc Oxide Film and Its Application to Solar Cells,” *Jpn. J. Appl. Phys.*, vol. 51, p. 10NB13, Oct. 2012.

[13] A. Hongsingthong, T. Krajangsang, I. A. Yunaz, S. Miyajima, and M. Konagai, “ZnO Films with Very High Haze Value for Use as Front Transparent

Conductive Oxide Films in Thin-Film Silicon Solar Cells," *Appl. Phys. Express*, vol. 3, no. 5, p. 051102, May 2010.

[14] 131st Committee on thin film, *Hakumakukougaku (Engineering of Thin Film) [in Japanese]*, 2nd ed. Tokyo: Maruzen, 2003.

[15] R. Curley, T. Mccormack, and M. Phipps, "Low-pressure CVD and Plasma-Enhanced CVD." [Online]. Available: http://www.ece.umd.edu/class/enee416/GroupActivities/LPCVD-PECVD.pdf. [Accessed: 17-Jun-2014].

[16] Z. Jarzebski and J. Marton, "Physical Properties of SnO Materials I. Preparation and Defect Structure," *J. Electrochem. Soc.*, no. 13, pp. 199–205, 1976.

[17] R. Summitt, J. A. Marley, and N. F. Borrelli, "The ultraviolet absorption edge of stannic oxide (SnO_2)," *J. Phys. Chem. Solids*, vol. 25, no. 12, pp. 1465–1469, Dec. 1964.

[18] Y. Mi, H. Odaka, and S. Iwata, "Electronic Structures and Optical Properties of ZnO, SnO_2 and In_2O_3," *Jpn. J. Appl. Phys.*, vol. 38, no. Part 1, No. 6A, pp. 3453–3458, Jun. 1999.

[19] C. Körber, P. Ágoston, and A. Klein, "Surface and bulk properties of sputter deposited undoped and Sb-doped SnO_2 thin films," *Sensors Actuators B Chem.*, vol. 139, no. 2, pp. 665–672, Jun. 2009.

[20] S. Nakao, N. Yamada, T. Hitosugi, Y. Hirose, T. Shimada, and T. Hasegawa, "High Mobility Exceeding 80 cm^2V^{-1} s^{-1} in Polycrystalline Ta-Doped SnO_2 Thin Films on Glass Using Anatase TiO 2 Seed Layers," *Appl. Phys. Express*, vol. 3, no. 3, p. 031102, Feb. 2010.

[21] S. Nakao, N. Yamada, T. Hitosugi, Y. Hirose, T. Shimada, and T. Hasegawa, "Fabrication of transparent conductive W-doped SnO_2 thin films on glass substrates using anatase TiO_2 seed layers," *Phys. Status Solidi*, vol. 8, no. 2, pp. 543–545, Feb. 2011.

[22] I. Hamberg and C. Granqvist, "Evaporated Sn-doped In_2O_3 films: Basic optical properties and applications to energyâ€ • efficient windows," *J. Appl. Phys.*, 1986.

[23] H. Odaka, S. Iwata, and N. Taga, "Study on electronic structure and optoelectronic properties of indium oxide by first-principles calculations," *Jpn. J. Appl. Phys.*, vol. 36, pp. 5551–5554, 1997.

[24] H. Odaka and Y. Shigesato, "Electronic structure analyses of Sn-doped In_2O_3," *Jpn. J. Appl. Phys.*, vol. 40, no. 5, pp. 3231–3235, 2001.

[25] M. F. a. M. van Hest, M. S. Dabney, J. D. Perkins, D. S. Ginley, and M. P. Taylor, "Titanium-doped indium oxide: A high-mobility transparent conductor," *Appl. Phys. Lett.*, vol. 87, no. 3, p. 032111, 2005.

[26] X. Li, Q. Zhang, W. Miao, L. Huang, Z. Zhang, and Z. Hua, "Development of novel tungsten-doped high mobility transparent conductive In_2O_3 thin films," *J. Vac. Sci. Technol. A Vacuum, Surfaces, Film.*, vol. 24, no. 5, p. 1866, 2006.

[27] X. Li, Q. Zhang, W. Miao, L. Huang, and Z. Zhang, "Transparent conductive oxide thin films of tungsten-doped indium oxide," *Thin Solid Films*, vol. 515, no. 4, pp. 2471–2474, Dec. 2006.

[28] T. Koida and M. Kondo, "Improved near-infrared transparency in sputtered In_2O_3-based transparent conductive oxide thin films by Zr-doping," *J. Appl. Phys.*, vol. 101, no. 6, p. 063705, 2007.

[29] T. Koida, M. Kondo, K. Tsutsumi, A. Sakaguchi, M. Suzuki, and H. Fujiwara, "Hydrogen-doped In_2O_3 transparent conducting oxide films prepared by solid-phase crystallization method," *J. Appl. Phys.*, vol. 107, no. 3, p. 033514, 2010.

[30] P. Erhart, K. Albe, and A. Klein, "First-principles study of intrinsic point defects in ZnO: Role of band structure, volume relaxation, and finite-size effects," *Phys. Rev. B*, vol. 73, no. 20, p. 205203, May 2006.

[31] J. Pollmann, D. Vogel, and P. Kru, "Self-interaction and relaxation-corrected pseudopotentials for II-VI semiconductors," vol. 54, no. 8, pp. 5495–5511, 1996.

[32] W. W. Wenas, A. Yamada, K. Takahashi, M. Yoshino, and M. Konagai, "Electrical and optical properties of boron-doped ZnO thin films for solar cells

grown by metalorganic chemical vapor deposition," *J. Appl. Phys.*, vol. 70, pp. 7119–7123, 1991.

[33] A. Ohtomo, M. Kawasaki, T. Koida, K. Masubuchi, H. Koinuma, Y. Sakurai, Y. Yoshida, T. Yasuda, and Y. Segawa, "$Mg_xZn_{1-x}O$ as a II–VI widegap semiconductor alloy," *Appl. Phys. Lett.*, vol. 72, no. 19, p. 2466, 1998.

[34] R. Hashimoto, Y. Abe, and T. Nakada, "High Mobility Titanium-Doped In_2O_3 Thin Films Prepared by Sputtering/Post-Annealing Technique," *Appl. Phys. Express*, vol. 1, no. 1, p. 015002, Jan. 2008.

[35] S. Nakao and T. Hasegawa, "Indium-free TCOs for various applications," in *The 9th International Conference on Coating on Glass and Plastics (ICCG9)*, 2012, pp. 5–05.

[36] K. Sato, Y. Gotoh, Y. Wakayama, Y. Hayasahi, K. Adachi, and H. Nishimura, "Highly Textured SnO_2:F TCO Films for a-Si solar cells," *Res. Reports Asahi Glas. Co., Ltd.*, vol. 42, pp. 129–137, 1992.

[37] C. Agashe, "Efforts to improve carrier mobility in radio frequency sputtered aluminum doped zinc oxide films," *J. Appl. Phys.*, vol. 95, no. 4, p. 1911, 2004.

[38] J. W. Grate, S. J. Martin, and R. M. White, "Acoustic Wave Microsensors," *Anal. Chem.*, vol. 65, no. 21, p. 940A–948A, Nov. 1993.

[39] A. Masuda, K. Imamori, and H. Matsumura, "Influence of atomic hydrogen on transparent conducting oxides during hydrogenated amorphous and

microcrystalline Si preparation by catalytic chemical vapor deposition," *Thin Solid Films*, vol. 411, no. 1, pp. 166–170, May 2002.

[40] M. Kambe, K. Sato, D. Kobayashi, Y. Kurokawa, S. Miyajima, M. Fukawa, N. Taneda, A. Yamada, and M. Konagai, "TiO_2 -Coated Transparent Conductive Oxide (SnO_2 :F) Films Prepared by Atmospheric Pressure Chemical Vapor Deposition with High Durability against Atomic Hydrogen," *Jpn. J. Appl. Phys.*, vol. 45, no. No. 10, pp. L291–L293, Mar. 2006.

[41] T. Kawashima, H. Matsui, K. Goto, and N. Tanabe, "Heat Resistant Double-Layered TCO," *Fujikura Tech. Rev.*, vol. 33, 2004.

[42] F. J. Pern, R. Noufi, X. Li, C. Dehart, and B. To, "Damp-Heat Induced Degradation of Transparent Conducting Oxides for Thin-Film Solar Cells," in *Proceedings of 33rd IEEE Photovoltaic Specialists Conference*, 2008.

[43] D. KEMPTHORNE and M. D. Myers, "MINERAL COMMODITY SUMMARIES 2008," Washington, 2008.

[44] T. Homma, T. Ueno, K. Sekizawa, A. Tanaka, and M. Hirata, "Interstitial Pneumonia Developed in a Worker Dealing with Particles Containing Indium-tin Oxide," *J. Occup. Health*, vol. 45, pp. 137–139, 2003.

Chapter 3[1]

3 Improving mobility of SnO_2:F Thin Films by Low-Pressure Chemical Vapor Deposition and temperature gradient

3.1 Introduction

Tin oxide (SnO_2) is one of the most common transparent conductive oxide (TCO) materials used as a front-side electrode for thin-film silicon-based solar cells. TCO films absorb sunlight because of free carriers in the near-infrared (NIR) region. Free carriers transport electrical charge, but they also cause the absorption of light in the NIR region, which suppresses the quantum efficiency (QE) at longer wavelengths in thin-film silicon solar cells[2]. Currently, a thin-film quintuple-junction solar cell is under development with the aim of converting the full spectrum of sunlight (UV to NIR) to achieve an ultrahigh efficiency[3]. For this purpose, the absorption of NIR wavelengths is critical, and low-level absorption is strongly desired.

High mobility is a key factor for suppressing free-carrier absorption. The optical properties of TCO films in the NIR region are well described by the Drude theory[4], [5]. If free-carrier concentration decreases, free-carrier absorption and conductivity decrease, because conductivity and carrier concentration are related by the equation $\sigma = en\mu$, where σ, e, n, and μ are the conductivity, electron charge, carrier concentration, and mobility, respectively. Therefore, if we want to maintain a high

conductivity with a decreased carrier concentration, a higher free-carrier mobility is required.

High-mobility TCO films were reported in In_2O_3-based materials (Sn-, Ti-, Zr-, Mo-, W-, and H-doped.)[6]–[16] However, In_2O_3 is not suitable for superstrate-type thin-film silicon solar cells, because indium oxide is reduced to In^0 when a Si layer is deposited with hydrogen plasma[17], [18]. Therefore, high-mobility TCO materials with a high durability for hydrogen plasma are valuable for superstrate-type thin-film silicon solar cells, such as SnO_2 and ZnO.

Recently, high-mobility TCO films of SnO_2-based materials have been reported for Ta-doped (83 cm^2/Vs)[19] and W-doped (84 cm^2/Vs)[20] films fabricated using pulsed laser deposition (PLD). However, large-area deposition is difficult using PLD[21]. On the other hand, F-doped SnO_2 (FTO) deposited on large-area glass substrates has been commercially fabricated using atmospheric-pressure chemical vapor deposition (APCVD). The mobilities of the FTO films thus fabricated were reported to be 35- 60 cm^2/Vs,[22]–[24] which were lower than the mobility of Ta-doped SnO_2 fabricated using PLD.

In the case of APCVD, various kinds of precursor materials have been used such as tetramethyltin (TMT), monobutyltinchloride (MBTC), and tin tetrachloride (TTC)[25], [26]. Among these materials, TTC has the highest mobility (60 cm^2/Vs) reported[24].

Compared with APCVD, LPCVD can be used to deposit films with high purity[27]. There are many reports on FTO using LPCVD[28]–[30]. In these reports, the precursor is TMT and the reported mobilities are 31 - 40 cm^2/Vs, which are lower than the mobility of FTO using APCVD with TTC. We can expect FTO films with a high

purity (and possibly high mobility) if FTO is fabricated using LPCVD with TTC, but there is as yet no such report to the best of our knowledge. Therefore, we have studied FTO films using LPCVD with TTC.

In this study, we investigated the mobility, carrier concentration, and crystallite orientation of FTO fabricated using LPCVD at various deposition temperatures and film thicknesses. Furthermore, we discuss the relationship between mobility and crystallite orientation and describe a method of improving the mobility of FTO films.

3.2 Fabrication of SnO_2:F Thin Films

3.2.1 Low Pressure Chemical Vapor Deposition System

FTO films were deposited using LPCVD on 0.7-mm-thick alkaline-free glass substrates (Asahi Glass AN100). Fig. 3-1 shows the configuration of the LPCVD chamber.

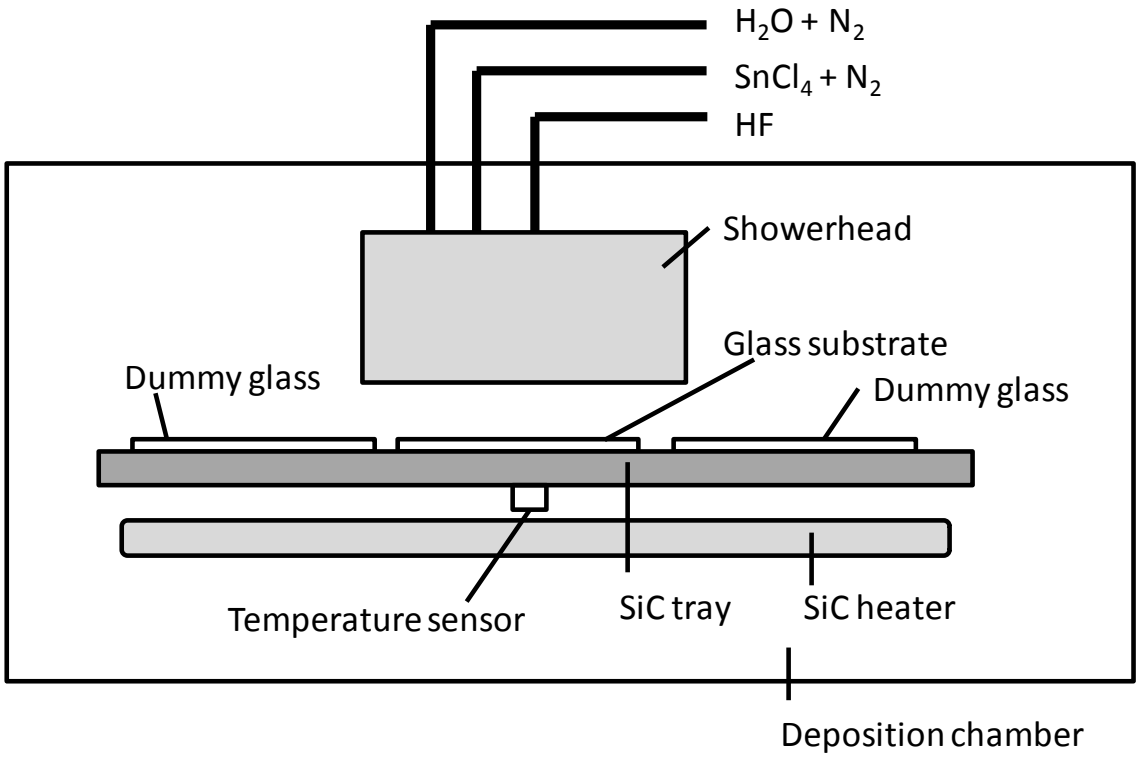

Fig. 3-1 Schematic diagram of LPCVD chamber.

A glass substrate was placed on a SiC tray, which was placed under a showerhead and heated from underneath using SiC heaters. The temperature of the chamber is controlled with a temperature sensor positioned below the SiC tray. The correlation between glass temperature and chamber temperature was measured in advance, using glass on which thermocouples were attached. $SnCl_4$, H_2O, and HF gases were supplied into the chamber through the showerhead. $SnCl_4$ and H_2O were vaporized using the bubbling method. N_2 was used as the carrier gas. HF, which was used to dope fluorine into SnO_2, was vaporized directly from liquid HF. These three gases were mixed downstream of the showerhead to avoid clogging the pipe. The flow rates (excluding that of the carrier N_2 gas) of $SnCl_4$, H_2O, and HF were set at 2, 200, and 8 sccm, respectively. The deposition period was varied from 2-30 min. In all the

experiments, the chamber pressure was kept at 100 Pa during deposition. During deposition, the temperature of the glass substrate was maintained between 350 and 600 °C. All the samples were annealed at 400 °C in 100% N_2 (1 atm) for 10 min before evaluation.

Film thickness was measured using a DEKTAK M6, which is a common stylus apparatus. The electrical resistivity ρ, the carrier concentration n, and the mobility μ of the films were obtained by Hall measurements in the van der Pauw configuration using BioRad HL5500. The crystallite structures of the films were analyzed using an X-ray diffraction (XRD) spectrometer (Rigaku RU-200) in θ/2θ scan. The films showed peaks corresponding to the (110), (101), (200), (210), (211), (220), (310), (301), and (321) planes of rutile SnO_2. The fraction of (hkl)-oriented crystallites f_{hkl} was determined as follows:

$$f_{hkl} = \frac{I_{hkl}}{F_{hkl}} \Big/ \sum_{h'k'l'} \frac{I_{h'k'l'}}{F_{h'k'l'}}$$

where F_{hkl} is a scattering correction factor defined in Powder Diffraction File (PDF) 41-1445 and I_{hkl} is the intensity of each diffraction peak after background subtraction. Crystallite size is estimated using Scherrer's equation assuming spherical crystallite specimens[31] as follows:

$$L_{hkl} = \frac{K\lambda}{B_{hkl}\cos\theta_{hkl}}$$

where L_{hkl}, K, λ, B_{hkl}, and θ_{hkl} are the crystallite size with (hkl) orientation, Scherrer constant 1.333, wavelength of X-ray, integral width of the (hkl) diffraction peak, and incident angle of the (hkl) diffraction peak. Cross-sectional SEM images were observed with Hitachi SU-70. Samples were cleaved and coated with osmium and platinum before SEM observation. The thicknesses of osmium and platinum were

approximately 3 and 1 nm, respectively.

3.2.2 Dependence of mobility and crystallite orientation on thickness

Figures Fig. 3-2 and Fig. 3-3 show the dependences of mobility, carrier concentration, fraction of (hkl)-oriented crystallites f_{hkl}, fraction of (301)-oriented crystallites f_{301}, and crystallite size with (301) orientation L_{301} on film thickness. Film thickness was controlled by changing the deposition time from 2 to 30 min. During the deposition, the glass temperature was held constant at 380°C. In thin films (less than 200 nm), the mobility is much lower than that in thick films. With increasing thickness, mobility, f_{301}, and L_{301} increase, but carrier concentration decreases monotonically. Figure Fig. 3-4 shows cross-sectional SEM images of the same samples shown in Fig. 3-3. It is clear that grains grow larger as film thickness increases.

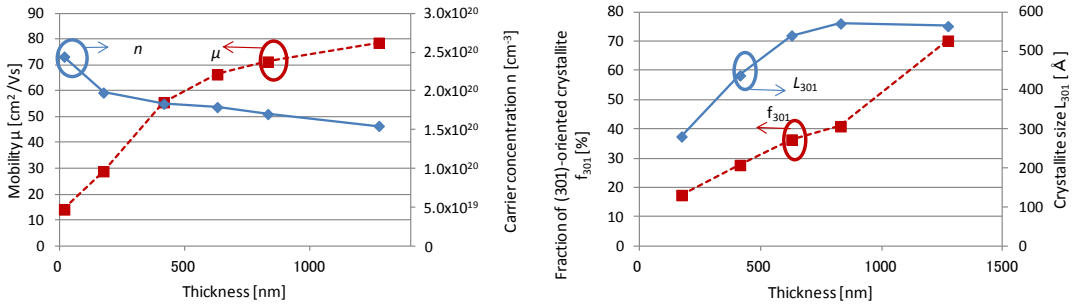

(a) (b)

Fig. 3-2 Dependences of (a) mobility μ and carrier concentration n, (b) fraction of (301)-oriented crystallites f_{301} and crystallite size with (301) orientation L_{301} on film thickness.

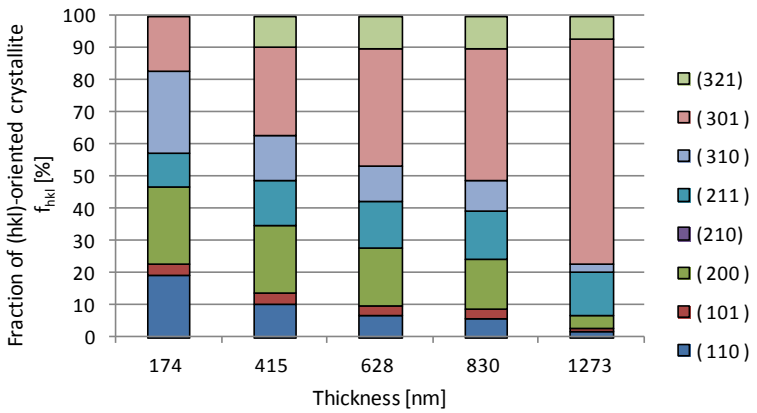

Fig. 3-3 Dependence of fraction of (hkl)-oriented crystallites f_{hkl} on film thickness.

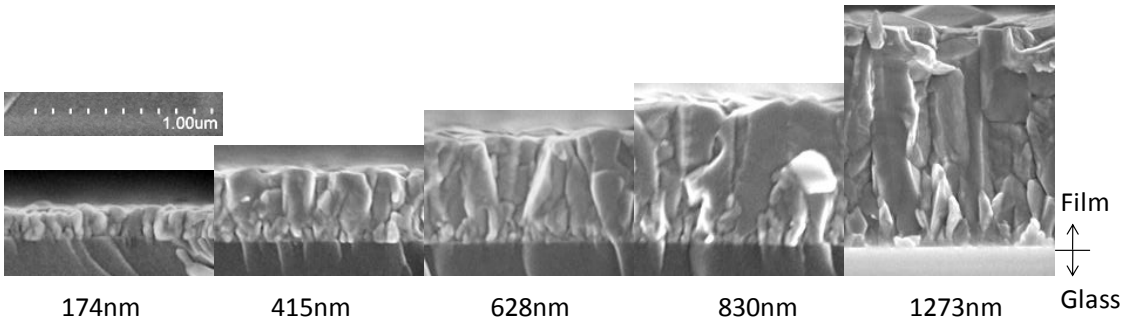

Fig. 3-4 Cross-sectional SEM images of various-thickness samples.

The above-mentioned dependence on film thickness can be explained as follows: At the beginning of the deposition, precursors attach to the glass substrate. At this stage, many surface orientations have similar formation energies, and thus no preferred orientation is observed. Consequently, many small grains with various crystallite orientations grow. This behavior can be seen in Fig. 3-3 and Fig. 3-4. Small grains with a random crystallite orientation result in a lower mobility. As film thickness increases, precursors attach to the SnO_2 surface. Under these experimental conditions, the (301) surface has the lowest formation energy and grains with (301)-oriented crystallites tend to grow larger. Larger grains and/or a larger f_{hkl} results in an increased mobility.

As shown in Fig. 3-2(a), mobility strongly depends on film thickness. In thick films (i.e., more than 800 nm thick), the mobility exceeded 70 cm^2/Vs. However, the bottom part of these thick films should have a lower mobility because thin films have a lower mobility, as Fig. 3-2(a) shows. This means that the mobility of the upper part should be higher than the measured mobility of a thick film. The electrical properties of a thick film can be modeled such that two layers are stacked, as shown in Fig. 3-5.

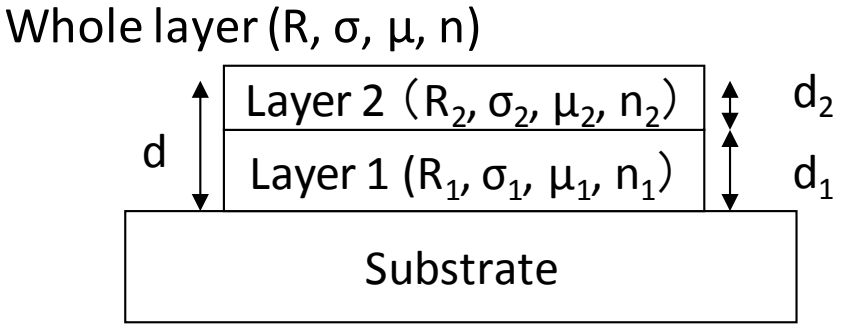

Fig. 3-5 Schematic of two-layer stack model. R, σ, μ, n, and d respectively represent the Hall coefficient, conductivity, mobility, carrier concentration, and thickness of the films. No suffix indicates the whole layer. The suffixes 1 and 2 indicate

layers 1 and 2, respectively.

Layer 1 (bottom part) has a lower mobility, and layer 2 (upper part) has a higher mobility. Petritz presented the Hall coefficient and conductivity of a two-layer stack model[32]. The formula of the Hall coefficient and conductivity is shown in eq(3-1). The definition of the symbols are given in Fig. 3-5.

$$R = \frac{(R_2\sigma_2{}^2 d_2 + R_1\sigma_1{}^2 d_1)d}{(\sigma_2 d_2 + \sigma_1 d_1)^2}, \quad \sigma = \frac{\sigma_2 d_2 + \sigma_1 d_1}{d} \tag{3-1}$$

Converting the formulas of R and σ to those of μ and n, we obtain eq.(3-2).

$$\mu_2 = \frac{n\mu^2 d - n_1\mu_1{}^2 d_1}{(n\mu d - n_1\mu_1 d_1)^2}, \qquad n_2 = \frac{(n\mu d - n_1\mu_1 d_1)^2}{(n\mu^2 d - n_1\mu_1{}^2 d_1)d_2} \tag{3-2}$$

Using these formulas, we calculated the mobility and carrier concentration of each stacked layer. For example, data of a 628-nm-thick film is used as the whole layer (μ and n), and data of a 415-nm-thick film is used as layer 1 (μ_1 and n_1). Then, the properties (μ_2 and n_2) of layer 2 (415 - 628 nm) are calculated. Figure Fig. 3-6 shows the calculated mobility of each stacked layer. A cross-sectional SEM image of a 1273-nm-thick sample is also shown. It is clear that the calculated mobility of each layer strongly correlates with grain size. Note that the calculated mobility of the top layer (830 - 1273 nm) exceeds 90 cm^2/Vs. It shows the possibility that FTO can achieve a higher mobility of over 90 cm^2/Vs.

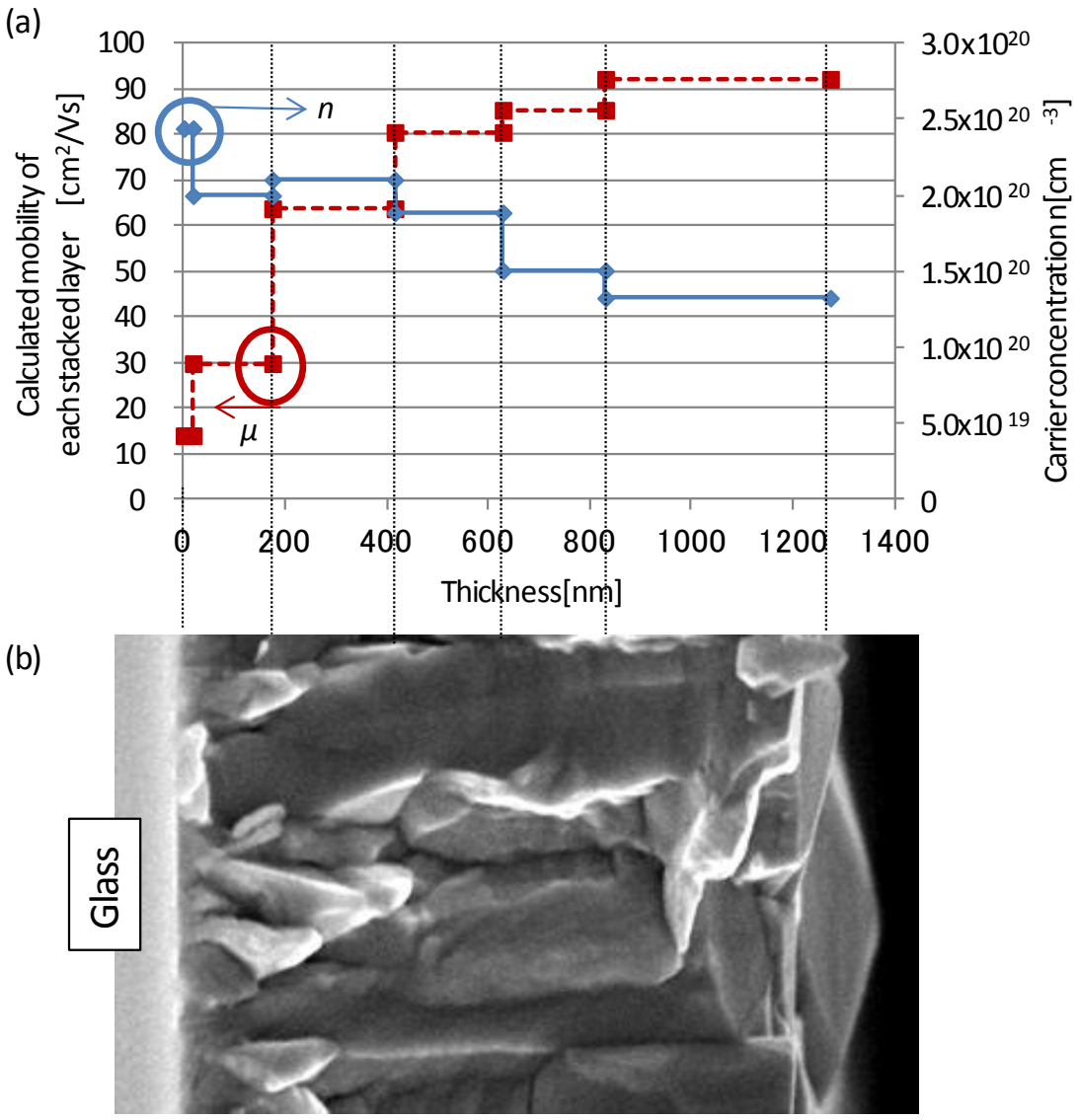

Fig. 3-6 (a) Calculated mobility of each stacked layer. (b) Cross-sectional SEM image of sample with 1273 nm thickness.

3.2.3 Dependence of mobility and crystallite orientation on deposition temperature

Fig. 3-7 shows the dependences of mobility, carrier concentration, fraction of (301)-oriented crystallites $f_{\{301\}}$, and crystallite size with (301) orientation $L_{\{301\}}$ on

deposition temperature for thick (20 min deposition, ~ 800 nm thick) and thin (5 min deposition, ~ 200 nm thick) films. Figure Fig. 3-8 shows the dependence of the fraction of (hkl)-oriented crystallites f_{hkl} on the deposition temperature of the thick samples (20 min deposition). The mobility peaks at approximately 380 °C for the thick films, and at approximately 410 °C for the thin films. f_{301} peaks at a slightly higher temperature than the mobility for both the thick and thin films. Carrier concentration is almost constant below 480 °C and decreases above 480 °C for the thick films. The crystallite size with (301) orientation L_{301} is almost constant for the thin films, and increases monotonically for the thick films as temperature increases below 450 °C. In the samples deposited above 500 °C, no (301) peak is observed. Although L_{200} and L_{110} are plotted for reference, it is difficult to compare the crystallite size with the size of the samples below 450 °C.

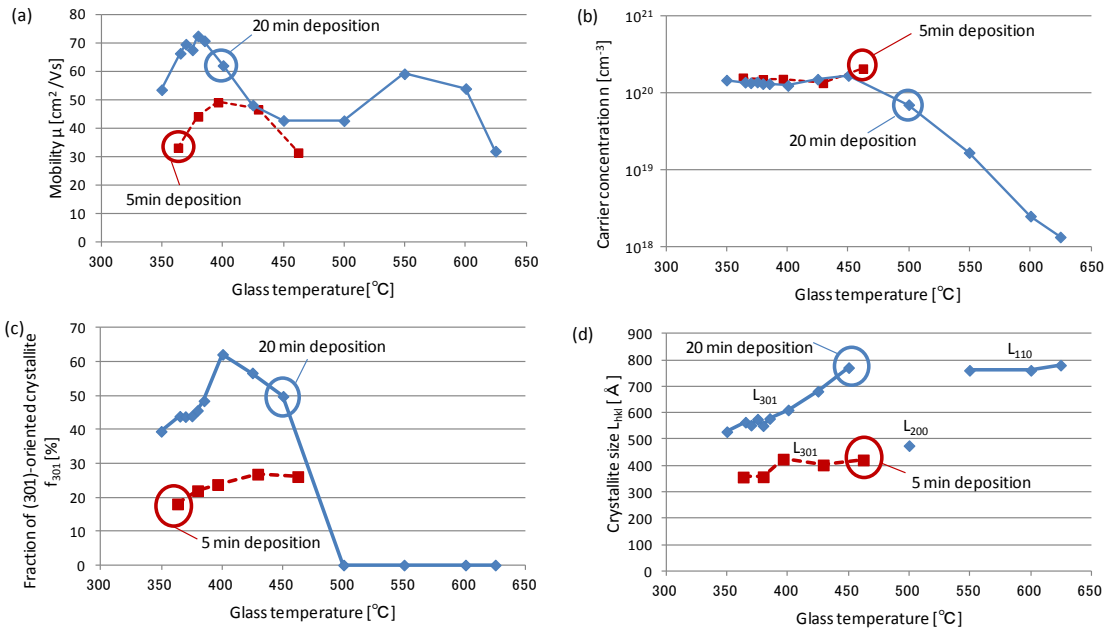

Fig. 3-7 Dependences of (a) mobility μ, (b) carrier concentration n, (c) fraction of (301)-oriented crystallites f_{301}, and (d) crystallite size with (301) orientation L_{301} on deposition temperature for thick and thin films. Regarding the crystallite size of the

thick samples deposited above 500°C, L_{200} and L_{110} are plotted for reference because no (301) peak is observed.

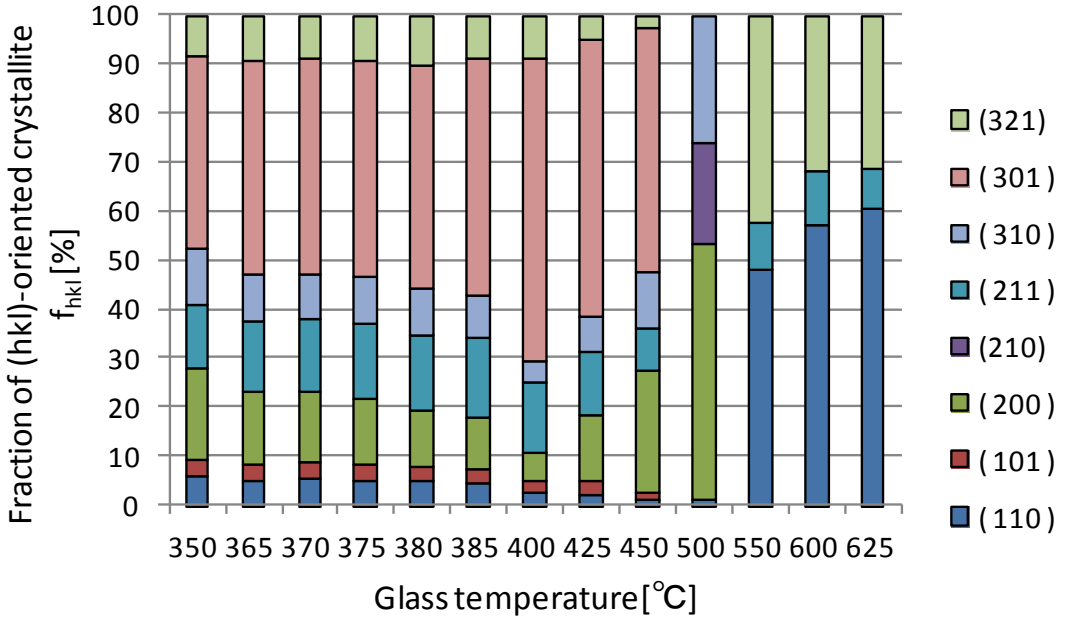

Fig. 3-8 Dependence of fraction of (hkl)-oriented crystallites f_{hkl} on deposition temperature.

Cross-sectional SEM images of the samples with various deposition temperatures are shown in Fig. 3-9. Below 400°C, the cross-sectional images are similar. Columnar grains are observed at the middle and top parts, and small grains are observed at the bottom part. However, there is a tendency that the bottom thickness where small grains are observed increases as deposition temperature decreases. The film surface is flat. Corresponding to the flat surface, the appearances of the films are not hazy. In the samples deposited at 425 - 450 °C, the widths of columnar grains at the middle and top are larger than that in samples deposited below 400 °C. The surfaces of the top side are

textured, and their appearance is more hazy. In the samples deposited above 500 °C, no (301) peak is observed, and the width of columnar grains decreases compared with that of the samples deposited below 450 °C. The film surface is flat and not hazy.

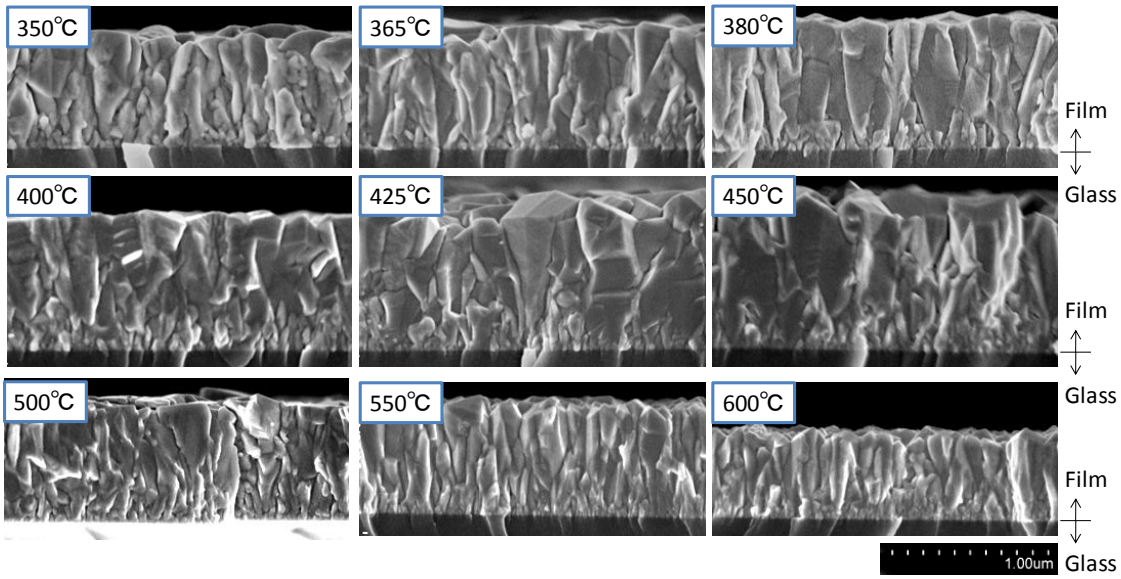

Fig. 3-9 Cross-sectional SEM images at various deposition temperatures.

We now discuss the relationship between mobility, fraction of crystallite orientation, and grain size. As described above, mobility and f_{301} both peak at similar temperatures, and both increase with increasing film thickness. Therefore, mobility and f_{301} have a strong positive correlation. Comparing the samples deposited at 380 and 400 °C with those deposited at 350 and 365 °C, the thickness of the bottom part with small grains is smaller, and f_{301} is slightly larger, as shown in Fig. 3-7(c) and Fig. 3-9. This can be understood to indicate that (301) is more preferred, and (301) becomes dominant at the earlier stage of deposition at 380 and 400 °C than at 350 and 365 °C. The columnar grain size observed by cross-sectional SEM seems to increase as temperature increases up to 450 °C.

Samples deposited above 500 °C have smaller grain size. The crystallite size with (301) orientation L_{301} increases up to 450 °C. This shows a similar tendency to columnar grain size. Therefore, the correlation between grain size and mobility is not clear.

On the basis of the above results, it seems reasonable to conclude that increasing f_{301} is one way to increase mobility. From the viewpoint of crystal structure, electrons can move more easily parallel to the c-axis than parallel to the ab-plane because the lattice constant c is smaller than a[33]. However, because the (301) plane is not parallel to the c-axis, it is not clear why a larger f_{301} is favorable for high mobility, at this moment. In addition, the (200) plane is preferable for APCVD[34] in contrast to the results reported herein. Note that this study is the first investigation of the properties of (301)-preferred-orientation films.

3.3 Introduction of temperature gradient ⊿T to improve mobility

We reported that the mobility of the bottom part is lower than that of the upper part. We also found that the temperature at which the mobility peaks depended on film thickness. Therefore, to improve the mobility of both the bottom and upper parts, we varied the glass temperature from a higher value to a lower value during deposition. Figure Fig. 3-10 shows a schematic of the resulting temperature profile. The temperature at the end of deposition was fixed at 380 °C, which was the temperature at which the mobility was maximum in the thick film. The temperature at the start of the deposition was varied from 380 to 480 °C. We use ΔT to represent the temperature

difference between the start and end of the deposition.

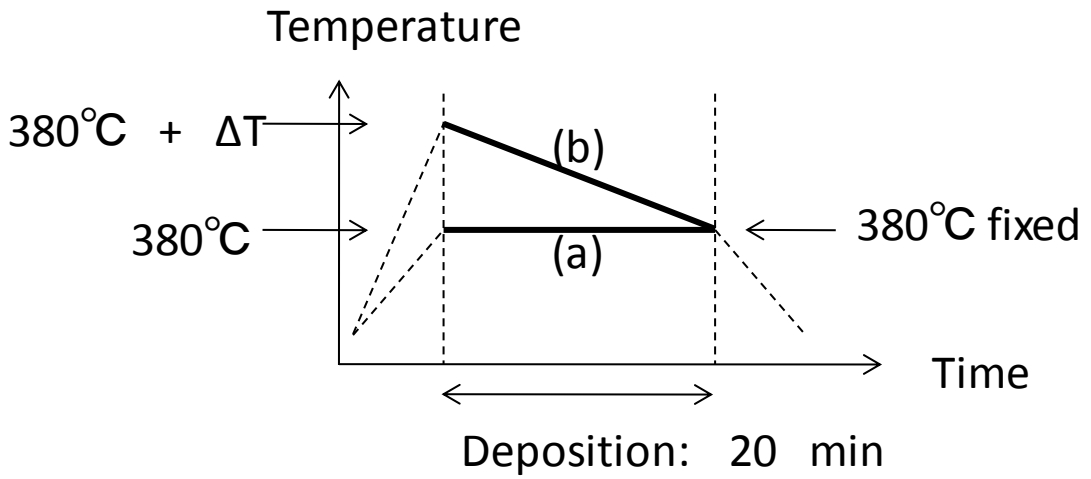

Fig. 3-10 Schematic of glass temperature profile during deposition with temperature gradient ΔT. (a) Conventional and (b) new profiles with ΔT.

Fig. 3-11 shows the ΔT dependences of mobility and carrier concentration. As we have expected, mobility increases from 72.5 cm^2/Vs at ΔT = 0 °C to 77.5 cm^2/Vs at ΔT = 55 °C. Carrier concentration decreases monotonically over this same range of ΔT values. Cross-sectional SEM images of samples with various ΔT values are also shown in Fig. 3-12.

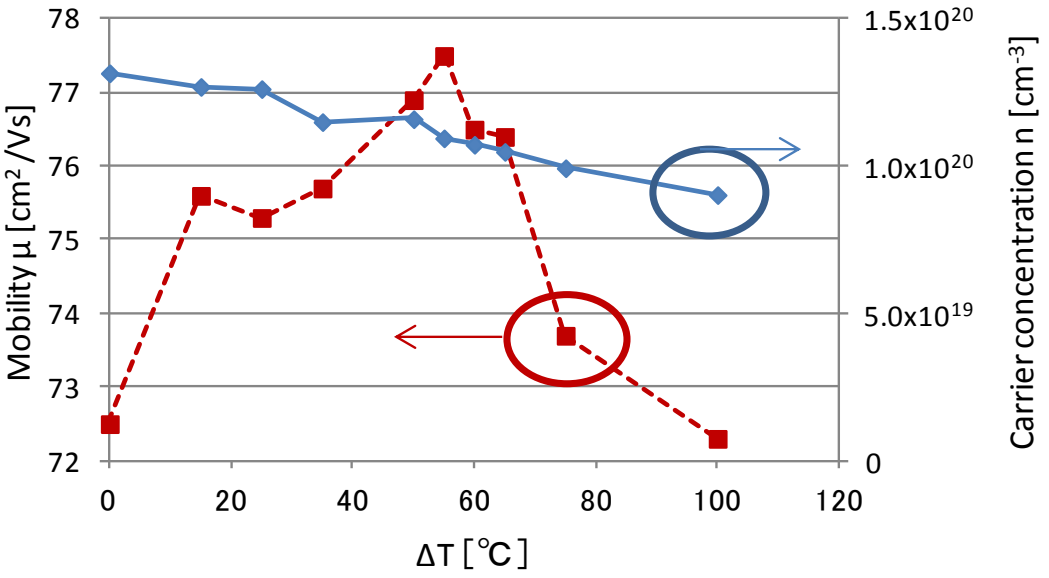

Fig. 3-11 ΔT dependences of mobility and carrier concentration. The horizontal axis ΔT is explained in Fig. 3-10.

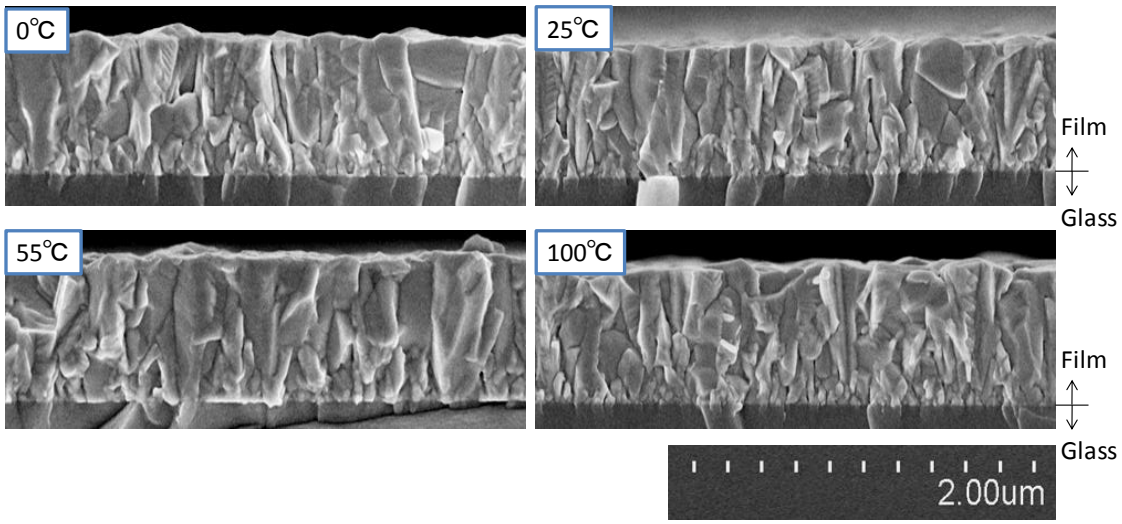

Fig. 3-12 Cross-sectional SEM images of samples with various ΔT values.

The dependence of mobility on ΔT can be explained as follows: For ΔT = 55 °C, the bottom part of the film was deposited at temperatures above 380 °C. As

shown in Fig. 3-7(a), mobility peaks at 410 °C in thin films (5 min deposition). Therefore, the mobility of the bottom part of the film was improved because of the higher deposition temperature introduced by the temperature gradient ΔT. In this scenario, the orientation fraction f_{301} of the bottom part of the film should increase with the temperature gradient ΔT in a manner similar to that found for the 5 min deposition, which is shown in Fig. 3-7(c). However, we observed no difference in f_{301} between ΔT= 55 °C and ΔT = 0 °C (data not shown). We think that, with ΔT = 55 °C, f_{301} increased at the start of the deposition, but the variation in f_{301} for the bottom part of the film was too small to be observed by the XRD analysis of the thick films (the samples used to study the effect of varying ΔT were thick films with a 20 min deposition time). From cross-sectional SEM images, we can see the tendency that the sample with ΔT =55 °C has a thinner bottom part with small grains than the samples deposited at other ΔT values. This supports our understanding described above.

3.4 Conclusion

We investigated how the electrical properties and crystallite orientation of FTO films fabricated by LPCVD depend on film thickness and deposition temperature. We found that, depending on film thickness, mobility peaked at different deposition temperatures. The temperature at which the mobility peaked for a thin film was higher than that for a thick film. On the basis of this result, we introduced a temperature gradient ΔT during deposition, which improved the mobility of FTO to 77.5 cm^2/Vs.

References

[1] M. Isshiki, T. Ikeda, J. Okubo, T. Oyama, and E. Shidoji, "Improving Mobility of F-Doped SnO_2 Thin Films by Introducing Temperature Gradient during Low-Pressure Chemical Vapor Deposition," *Jpn. J. Appl. Phys.*, vol. 51, p. 095801, 2012.

[2] J. Krc, B. Lipovsek, M. Bokalic, A. Campa, T. Oyama, M. Kambe, T. Matsui, H. Sai, M. Kondo, and M. Topic, "Potential of thin-film silicon solar cells by using high haze TCO superstrates," *Thin Solid Films*, vol. 518, no. 11, pp. 3054–3058, Mar. 2010.

[3] M. Konagai, "Present Status and Future Prospects of Silicon Thin-Film Solar Cells," *Jpn. J. Appl. Phys.*, vol. 50, p. 030001, Mar. 2011.

[4] P. Drude, "Zur Elektronentheorie der Metalle," *Ann. Phys.*, vol. 306, no. 3, pp. 566–613, 1900.

[5] P. Drude, "Zur Elektronentheorie der Metalle; II. Teil. Galvanomagnetische und thermomagnetische Effecte," *Ann. Phys.*, vol. 308, no. 11, pp. 369–402, 1900.

[6] Y. Kanai, "Electrical properties of In_2O_3 single crystals doped with metallic donor impurity," *Jpn. J. Appl. Phys.*, vol. 23, p. 127, 1984.

[7] Y. Meng, X. Yang, H. Chen, J. Shen, Y. Jiang, Z. Z. U, and Z. Hua, "A new transparent conductive thin film In_2O_3:Mo," *Thin Solid Films*, vol. 394, pp. 219–223, 2001.

[8] Y. Yoshida, D. M. Wood, T. a. Gessert, and T. J. Coutts, "High-mobility, sputtered films of indium oxide doped with molybdenum," *Appl. Phys. Lett.*, vol. 84, no. 12, p. 2097, 2004.

[9] C. Warmsingh, "High-mobility transparent conducting Mo-doped In_2O_3 thin films by pulsed laser deposition," *J. Appl. Phys.*, vol. 95, no. 7, p. 3831, 2004.

[10] a. E. Delahoy and S. Y. Guo, "Transparent and semitransparent conducting film deposition by reactive-environment, hollow cathode sputtering," *J. Vac. Sci. Technol. A Vacuum, Surfaces, Film.*, vol. 23, no. 4, p. 1215, 2005.

[11] T. Koida and M. Kondo, "Comparative studies of transparent conductive Ti-, Zr-, and Sn-doped In_2O_3 using a combinatorial approach," *J. Appl. Phys.*, vol. 101, no. 6, p. 063713, 2007.

[12] M. F. a. M. van Hest, M. S. Dabney, J. D. Perkins, D. S. Ginley, and M. P. Taylor, "Titanium-doped indium oxide: A high-mobility transparent conductor," *Appl. Phys. Lett.*, vol. 87, no. 3, p. 032111, 2005.

[13] P. F. Newhouse, C.-H. Park, D. a. Keszler, J. Tate, and P. S. Nyholm, "High electron mobility W-doped In_2O_3 thin films by pulsed laser deposition," *Appl. Phys. Lett.*, vol. 87, no. 11, p. 112108, 2005.

[14] T. Koida and M. Kondo, "High-mobility transparent conductive Zr-doped In_2O_3," *Appl. Phys. Lett.*, vol. 89, no. 8, p. 082104, 2006.

[15] T. Koida and M. Kondo, "Improved near-infrared transparency in sputtered In_2O_3-based transparent conductive oxide thin films by Zr-doping," *J. Appl. Phys.*, vol. 101, no. 6, p. 063705, 2007.

[16] T. Koida, M. Kondo, K. Tsutsumi, A. Sakaguchi, M. Suzuki, and H. Fujiwara, "Hydrogen-doped In_2O_3 transparent conducting oxide films prepared by solid-phase crystallization method," *J. Appl. Phys.*, vol. 107, no. 3, p. 033514, 2010.

[17] a I. Martínez, L. Huerta, J. M. O.-R. De León, D. Acosta, O. Malik, and M. Aguilar, "Physicochemical characteristics of fluorine doped tin oxide films," *J. Phys. D. Appl. Phys.*, vol. 39, no. 23, pp. 5091–5096, Dec. 2006.

[18] M. Kambe, N. Taneda, A. Takahashi, and T. Oyama, "Coated Glass Substrates for Silicon Based Thin Film Solar Cells," *Res. Reports Asahi Glas. Co., Ltd.*, vol. 60, 2010.

[19] S. Nakao, N. Yamada, T. Hitosugi, Y. Hirose, T. Shimada, and T. Hasegawa, "High Mobility Exceeding 80 $cm^2V^{-1}s^{-1}$ in Polycrystalline Ta-Doped SnO_2 Thin Films on Glass Using Anatase TiO_2 Seed Layers," *Appl. Phys. Express*, vol. 3, no. 3, p. 031102, Feb. 2010.

[20] S. Nakao, N. Yamada, T. Hitosugi, Y. Hirose, T. Shimada, and T. Hasegawa, "Fabrication of transparent conductive W-doped SnO_2 thin films on glass substrates using anatase TiO2 seed layers," *Phys. Status Solidi*, vol. 8, no. 2, pp. 543–545, Feb. 2011.

[21] J. a. Greer, “Large-area pulsed laser deposition: Techniques and applications,” *J. Vac. Sci. Technol. A Vacuum, Surfaces, Film.*, vol. 13, no. 3, p. 1175, May 1995.

[22] M. Mizuhashi, Y. Gotoh, K. Adachi, and Y. Gotoh, “Texture Morphology of SnO_2:F films and cell reflectance,” *Jpn. J. Appl. Phys.*, vol. 27, no. 11, pp. 2053–2061, 1988.

[23] M. Kambe, K. Sato, D. Kobayashi, Y. Kurokawa, S. Miyajima, M. Fukawa, N. Taneda, A. Yamada, and M. Konagai, “TiO_2 -Coated Transparent Conductive Oxide (SnO_2 :F) Films Prepared by Atmospheric Pressure Chemical Vapor Deposition with High Durability against Atomic Hydrogen,” *Jpn. J. Appl. Phys.*, vol. 45, no. No. 10, pp. L291–L293, Mar. 2006.

[24] K. Sato, Y. Gotoh, Y. Wakayama, Y. Hayasahi, K. Adachi, and H. Nishimura, “Highly Textured SnO_2:F TCO Films for a-Si solar cells,” *Res. Reports Asahi Glas. Co., Ltd.*, vol. 42, pp. 129–137, 1992.

[25] Y. Gotoh and M. Mizuhashi, “Effect of methanol addition on formation of tin oxide films by CVD,” *Res. Reports Asahi Glas. Co., Ltd.*, 1984.

[26] J. van Deelen, T. van Mol, P. Poodt, F. Grob, and K. Spee, “Development of APCVD process for high quality TCO,” *2009 34th IEEE Photovolt. Spec. Conf.*, pp. 000271–000275, Jun. 2009.

[27] R. Curley, T. Mccormack, and M. Phipps, “Low-pressure CVD and Plasma-Enhanced CVD.” [Online]. Available:

http://www.ece.umd.edu/class/enee416/GroupActivities/LPCVD-PECVD.pdf. [Accessed: 17-Jun-2014].

[28] T. a. Gessert, J. Burst, X. Li, M. Scott, and T. J. Coutts, "Advantages of transparent conducting oxide thin films with controlled permittivity for thin film photovoltaic solar cells," *Thin Solid Films*, vol. 519, no. 21, pp. 7146–7148, Aug. 2011.

[29] C. Wan, R. McGrath, W. Keenan, and S. Frank, "LPCVD of Tin Oxide from Tetramethyltin and Oxygen," *J. Electrochem. Soc.*, vol. 136, no. 5, p. 1459, 1989.

[30] X. Li, T. Gessert, C. DeHart, and T. Barnes, "A Comparison of Composite Transparent Conducting Oxides Based on the Binary Compounds CdO and SnO2," *NCPV Progr. Rev. ...*, no. October, 2001.

[31] A. Patterson, "The Scherrer formula for X-ray particle size determination," *Phys. Rev.*, vol. 56, pp. 978–982, 1939.

[32] R. Petritz, "Theory of photoconductivity in semiconductor films," *Phys. Rev.*, vol. 104, no. 6, p. 1508, 1956.

[33] 166th Comittee on Photonic and Electronic Oxide, *Tomei Dodenmaku no Gijutsu (Technology of Transparent Conductive Oxide Thin-Films)*, 2nd ed. Tokyo: Ohmsha, 2006, p. 51.

[34] T. Ikeda, K. Sato, and Y. Hayashi, "Surface microstructures of ZnO coated SnO_2: F films," *PVSEC*, 1993.

Chapter 4

4 Scattering Mechanisms in SnO_2:F Films

4.1 Introduction

TCO materials are needed to have two important properties. One is the high transparency in visible to near-infrared wavelength region by having wide band gap and adequately low carrier concentration. The other is the conductivity by having enough many carriers and high mobility. As described in Chapter 2, if carrier concentration is too high, absorption of TCO film in NIR region becomes higher. This is bad situation for solar cells which use the sunlight of NIR region. To suppress the absorption in NIR region by keeping conductivity high, high mobility is key parameter. Therefore, many researchers have studied scattering mechanisms of TCO materials. In this chapter, the studies of scattering mechanisms of various TCO are reviewed and we report our study about SnO_2:F thin films.

4.2 Theories of Scattering Mechanisms

Carriers are scattered by various mechanisms. Many researchers studied the scattering mechanisms in case of In_2O_3 and ZnO based TCO[1]–[14]. In this section, theories of various scattering mechanisms are reviewed and discussed. Theories for phonon scattering (4.2.1), ionized impurity scattering (4.2.2), and neutral impurity scattering (4.2.3) were summarized by Ellmer[15] as shown in this section. We will

discuss the theories for grain boundary scattering.

4.2.1 Phonon Scattering

There are three modes of lattice scattering. Optical phonon scattering, acoustic phonon scattering, and piezoelectric mode scattering which is caused by the electric field associated with acoustic phonons. In case of piezoelectric materials as ZnO etc, we need to consider the piezoelectric mode scattering. However in this thesis, we focus on SnO_2 which is not piezoelectric material. Therefore, we don't consider this mode here.

Ellmer summarized the mobility limited by phonon scattering as follows. *Optical mode scattering is due to the interaction of electrons with the electric field, induced by the lattice vibration polarization (polar longitudinal-optical phonons) occurring in polar semiconductors with partial ionic bonding.According to Devlin [16] the optical Hall mobility can be calculated by*

$$\mu_{Hopt} = r_{Hopt}\phi\frac{e}{2\alpha\omega_0 m^*}\left[exp\left(\frac{\hbar\omega_0}{kT}\right)-1\right] \qquad (4\text{-}1)$$

where the polaron coupling constant α *is given by*

$$\alpha = \left(\frac{1}{\varepsilon_\infty}-\frac{1}{\varepsilon_s}\right)\sqrt{\frac{m^* E_H}{m_e\hbar\omega_0}} \qquad (4\text{-}2)$$

ε_∞ *and* ε_s *are the high frequency and the static dielectric constants and* E_H *is the first ionization energy of the hydrogen atom (13.595 eV).* m^* *and* m_e *are the effective and the vacuum electron masses, while* $\hbar\omega_0$ *is the energy of the longitudinal optical phonons.* r_{Hopt} *is the Hall coefficient factor for optical mode scattering and* Φ *is a slowly varying function of the temperature. Usually it is assumed that* $r_{Hopt}\Phi$ *is equal to 1. [17][16]*

Acoustic mode scattering is a lattice deformation scattering process due to a

local enrgetic shift of the band edges originating from acoustic phonons. According to Bardeen and Schockley[18] the acoustical lattice mode Hall mobility is

$$\mu_{Hac} = r_{Hac}\frac{\sqrt{8\pi}\hbar^4 c_l e}{3E_1^2\sqrt{m^{*5}(kT)^3}} \qquad (4\text{-}3)$$

where c_l *is the averaged longitudinal elastic constant.* E_1 *is the deformation potential (energy shift of the conduction band per unit dilation).* $r_{Hac} = 3\pi/8 = 1.178$ *is the Hall coefficient for acoustic phonon scattering[19].* Various properties of TCO materials are shown in Table 4-1[20]

Property(unit)	ZnO	In_2O_3	SnO_2	Si
Band gap E_g(300k) [eV]	3.4 (dir)	2.7 (indir) 3.75 (dir)	3.6 (dir)	1.12 (indir) 4.18(dir)
Pressure coefficient of E_g dE_g/dp [meV/GPa]	23.5			-14.1(dir)
Temperature coefficient of E_g dE_g/dT [meV/K]	-0.3		-1.2	-0.47
Static dielectric constant ε_s or ε_r	∥ c:8.75 ⊥ c:7.8	≈9	∥ c:9.6 ⊥ c:13.5	11.9
High frequency permittivity ε_∞		4.18~4.26[2]	3.7~4.1[21]	
Density of states effective electron mass m_n^*/m_e	0.28	0.35	0.275 (∥ c:0.23 ⊥ c:0.3)	0.337
Density of states effective hole mass m_p^*/m_e	0.59	0.6	1.0	0.55
Nonparabolicity parameter β [eV^{-1}]	0.29; 0.14; 1.04	0.18	0.96	0.27; 0.5
Effective conduction band density of states (300K) N_C [cm^{-3}]	$3.7x10^{18}$	$4.1x10^{18}$	$3.7x10^{18}$	$4.9x10^{18}$
Exciton binding energy [meV]	59-65		130	14.3
Energy of the longitudinal optical phonon $\hbar\omega_0$ [meV]	73.1	41; 45; 51	34.1; 45.1; 86.8; 95.1	50.8; 51.9; 64.3
Deformation potential E_1 [eV]	31.4; 3.8; 18.9; 1.4; 3.5	33.3	8	9.5
Longitudinal elastic constant c_l [GPa]	204.7; 207.2; 185.3; 204.5	159	326	156
Piezoelectric coefficients $P_\perp; P_\parallel$	0.21; 0.36			
Extrinsic dopants	B, Al, Ga, In, Si, Ge, Sn, Y, Sc, Ti, Zr, Hf, F, Cl	Sn, Ti, Zr, F, Cl, Sb, Ge, Zn, Pb	Sb, As, P, F, Cl	B, Al, Ga, In, P, As, Sb

Table 4-1 Properties of TCO materials in comparison to that of silicon (Taken from [20])

4.2.2 Ionized Impurity Scattering

The mobility limited by ionized impurity scattering is summarized by Ellmer as follows[15]. *This scattering process is caused by the ionized dopant atoms and dominates for carrier concentrations above 5x10^{18} cm^{-3}. An analytical expression for the mobility μ_{ii} of degenerately doped semiconductors, taking into account the non-parabolicity of the conduction band, was given by Zawadzki and refined by Pisarkiewicz et al.[22].*

$$\boldsymbol{\mu_{ii}^{ZP} = \frac{3(\varepsilon_r\varepsilon_0)^2h^3}{Z^2m^{*2}e^3}\frac{n}{N_i}\frac{1}{F_{ii}^{np}(\xi_d)}} \text{ with } \boldsymbol{\xi_d = (3\pi^2)^{1/3}\frac{\varepsilon_r\varepsilon_0h^2n^{1/3}}{m^*e^2}} \qquad (4\text{-}4)$$

where n, N_i, and Z are carrier concentration, concentration of ionized impurity, and the valence number of the ionized impurity, and *the screening function* F_{ii}^{np} *is given by*

$$F_{ii}^{np} = \left[1 + \frac{4\xi_{np}}{\xi_d}\left(1 - \frac{\xi_{np}}{8}\right)\right] \cdot ln(1+\xi_d) - \frac{\xi_d}{1+\xi_d} - 2\xi_{np}\left(1 - \frac{5\xi_{np}}{16}\right) \qquad (4\text{-}5)$$

with the parameter $\xi_{np} = 1 - m_0^*/m^*$, *which describes the non-parabolicity of the conduction band (*m^*, m_0^* *refer to effective masses in the conduction band and at the conduction band edge, respectively). The non-parabolicity is described by the dependence* $m^*/m_0^* = 1 + 2\beta(E - E_C)$, *where* β *is the non-parabolicity parameter shown in Table 4-1,* E *and* E_C *are the energies of the carriers in the conduction band and at its edge. The prefactor in eq.(4-4) shows, that the ionized impurity limited mobility depends as* $\mu_{ii} \sim (\varepsilon_r/m^*)^2$ *on the material constants of the semiconductor and as* $\mu_{ii} \sim Z^{-2}$ *on the charge of the dopants* (for example, $Z = 1$ corresponds to group III donors for ZnO and group V donors for SnO_2, etc. $Z = 2$ corresponds to oxygen vacancies). In this thesis, Z is assumed to be 1 and n/N_i to be 1. This means that all free carriers are generated from singly charged donors. This condition is ideal for

achieving high mobility, because $n/N_i Z^2$ is maximum.

4.2.3 Neutral Impurity Scattering

The mobility limited by neutral impurity scattering is summarized by Ellmer as follows[15]. *The mobility due to neutral impurity scattering was first calculated by Erginsoy[23] who scaled the electron scattering at hydrogen atoms to a semiconductor by using its dielectric constant and carrier effective mass, which leads to:*

$$\mu_n = \frac{m^* e^3}{A(T) 4\pi\varepsilon\varepsilon_0 \hbar^3 N_n} \qquad (4\text{-}6)$$

Here $A(T)$ is the generally temperature-dependent scattering cross-section factor and N_n is the density of neutral scattering centers. However, this scattering process is considered to less dominant, because the shallow donors in TCO materials have ionization energies around 50 meV and most donors should be ionized. Therefore, we don't consider the neutral impurity scattering in this thesis.

4.2.4 Grain Barrier Scattering

[Barrier height]

In case of polycrystalline films, scattering at grain barrier is considered to be important in addition to phonon scattering and ionized impurity scattering. Seto described carrier transport in polycrystalline silicon film[24]. In his model, carriers are trapped at grain boundary, and the grain boundary is charged. Therefore, potential barrier is generated as shown in Fig. 4-1.

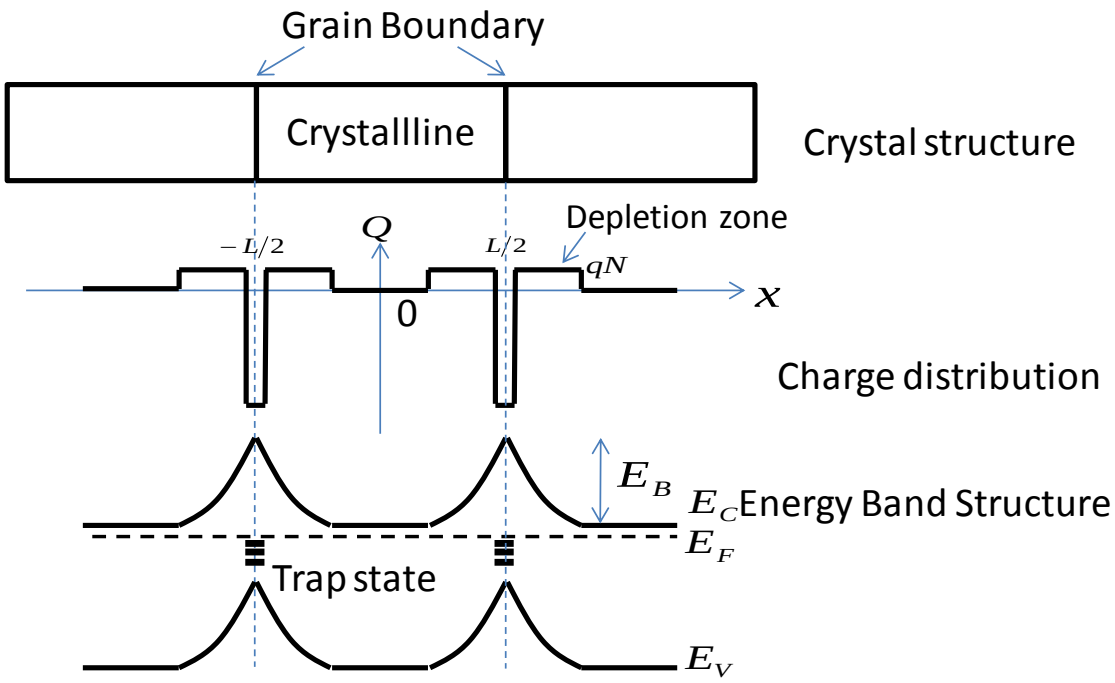

Fig. 4-1 Model for the grain structure in case of non-degenerated semiconductor.

The barrier height E_B measured from conduction band energy E_C (in case of non-degenerated) can be calculated by the Poisson's equation.

$$E_B = \frac{e^2 N_t^2}{8\varepsilon_r \varepsilon_0 n} \quad for\ Ln > N_t \tag{4-7}$$

$$E_B = \frac{e^2 L^2 n}{8\varepsilon_r \varepsilon_0} \quad for\ Ln < N_t$$

where e is the electron charge, N_t is the charge trap density at the grain boundary, $\varepsilon_r \varepsilon_0$ is the static dielectric constant, n is the carrier density in the bulk of the grain and L is the grain size. For $Ln < N_t$, the traps are only partially filled and the grains are completely depleted. For $Ln > N_t$, only part of the grains is depleted and the traps are filled completely. In this condition, the depletion width w is N_t/n.

In case of degenerated semiconductors, some researchers considered that barrier is formed on the conduction band edge[13], [25], [26]. They treated barrier

height for carriers as $E_B - (E_F - E_C)$. Therefore, barrier height can be negative in some case. However, negative barrier height means the top of barrier is located under Fermi level, and there is no depletion region. This contradicts with the concept of barrier model shown in Fig. 4-1. Therefore, the origin of barrier height should be set to the Fermi energy as shown in Fig. 4-2. We will adopt this concept in this thesis.

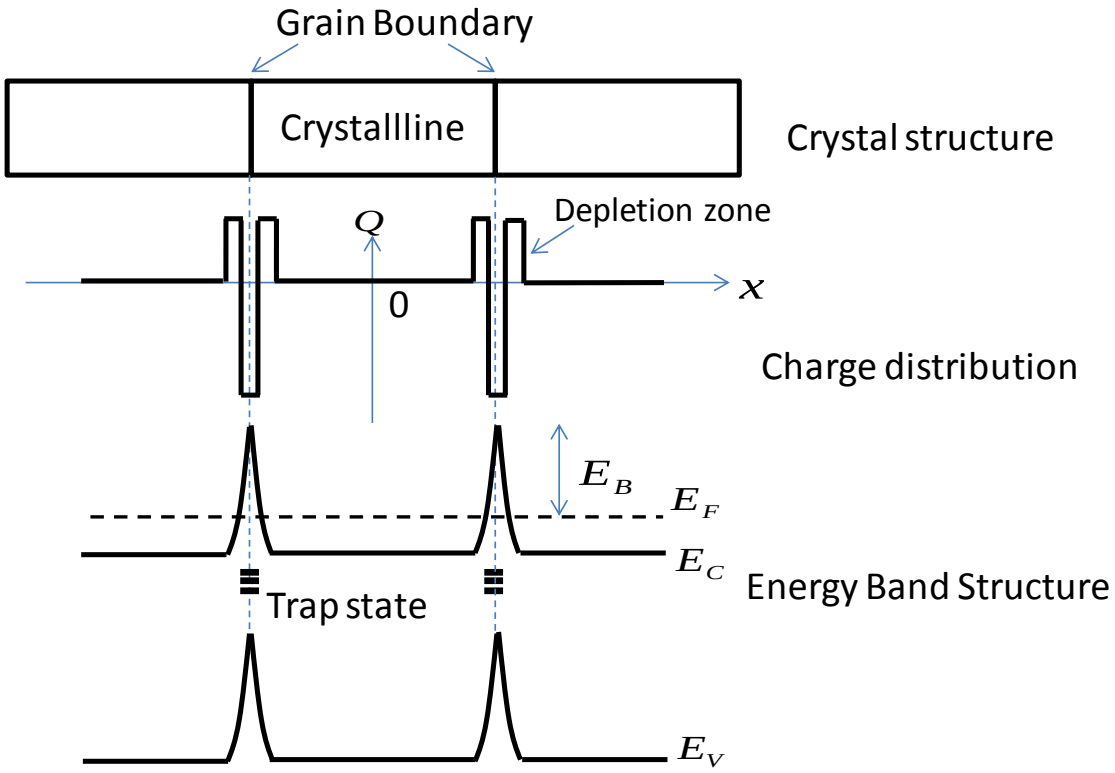

Fig. 4-2 Model for the grain structure in case of degenerated semiconductor.

[Thermionic emission current]

There are two processes that carriers go through the grain barriers. One is thermionic emission that carriers which have energy higher than E_B go beyond the barrier. The other is tunneling current by quantum mechanism. Seto formulated the mobility of thermionic emission process as eq.(4-8) in case of non-degenerated semiconductors. In his paper, tunneling current was neglected.

$$\mu_{th} = Le\left(\frac{1}{2\pi m^* kT}\right)^{1/2} exp\left(-\frac{E_B}{kT}\right) \quad (4\text{-}8)$$

Bruneaux et al. described the formula of thermionic emission by applying Fermi-Dirac distribution instead of Maxwell-Boltzmann approximation as eq.(4-9)[13].

$$\mu_{Bruneaux} = \frac{A^* LT}{nk} exp\left(-\frac{E_B}{kT}\right) \quad (4\text{-}9)$$

where A^* is Richardson constant $\frac{4\pi emk^2}{h^3}$, and E_B is the barrier height measured from E_F. (Note that the definition of E_B in eq.(4-9) is different from Ref [13], because they considered the barrier height from E_c as explained above.) Although the derivation of eq.(4-9) was not described in Ref [13], the formula seems to be derived from eq.(4-10) which describes thermionic emission current in Schottky diode[27]. However, Maxwell-Boltzmann approximation is involved in the derivation of eq.(4-10). Therefore, verification is needed. Furthermore, this formula eq.(4-9) is referred and adopted for analyzing TCO properties in some papers[28][29][6][30], but the temperature dependence of the mobility was inversed to $\propto \frac{1}{T}\ exp\left(-\frac{E_B}{kT}\right)$ by mistake.

$$J = A^* T^2 exp\left(-{E_B}/{kT}\right)\left(exp\left({V}/{kT}\right) - 1\right) \quad (4\text{-}10)$$

[Tunneling current]

The general formula of tunneling current across metal-insulator-metal(MIM) barrier is derived by Simmons[31]. He derived eq.(4-11) in case that applied voltage is small.

$$J_{tun} = \frac{3\sqrt{2m^* E_B}}{2w}\left(\frac{e}{h}\right)^2 exp\left(-\frac{4\pi w}{h}\sqrt{2m^* E_B}\right)V \quad (4\text{-}11)$$

where J_{tun} is current density across the barrier, V is the applied voltage across the

barrier. The schematic of this MIM barrier is shown in Fig. 4-3.

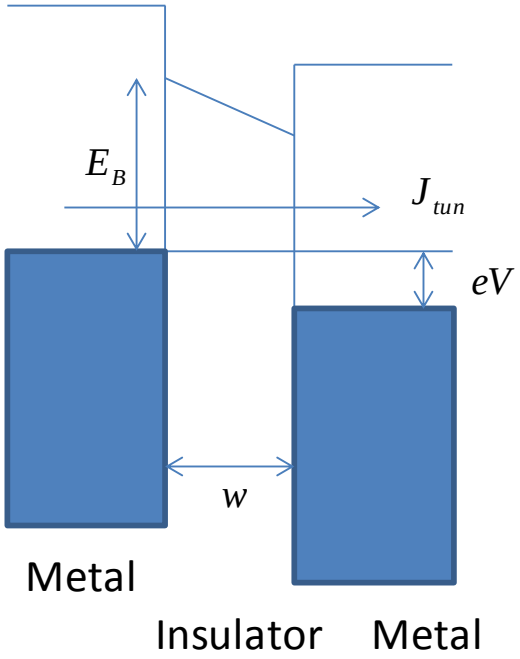

Fig. 4-3 Schematic of the Metal-Insulator-Metal barrier.

From eq.(4-11)(4-11), resistivity and mobility of the insulator can be calculated as

$$\rho_{tun\_MIM} = 1/\frac{3\sqrt{2m^*E_B}}{2}\left(\frac{e}{h}\right)^2 exp\left(-\frac{4\pi w}{h}\sqrt{2m^*E_B}\right) \quad (4\text{-}12)$$

$$\mu_{tun\_MIM} = \frac{3\sqrt{2m^*E_B}}{2en}\left(\frac{e}{h}\right)^2 exp\left(-\frac{4\pi w}{h}\sqrt{2m^*E_B}\right) \quad (4\text{-}13)$$

Steinhauser applied partially the concept of Simmons to explain the mobility dependence on carrier concentration[32]. However, another parameter l_{tun} (mean free path of electron for tunneling) was introduced to adjust the tunneling current, but the physical meaning of l_{tun} is not clear.

Jones et al. analyzed grain barrier scattering for degenerate polycrystalline Si films by considering tunneling current [25]. However, they considered the barrier is located under Fermi level as explained previously.

4.2.5 Mobility combined all scattering mechanisms

To compare the measured electrical properties and theories, we need to combine all scattering mechanisms. For this purpose, Matthiessen's rule is generally adopted.

$$\frac{1}{\tau_{\text{bulk}}} = \sum_i \frac{1}{\tau_i}, \qquad \frac{1}{\mu_{\text{bulk}}} = \sum_i \frac{1}{\mu_i} \tag{4-14}$$

where τ_{bulk}, μ_{bulk}, τ_i and μ_i are scattering relaxation time combined all scattering mechanisms, mobility combined them, relaxation time of each scattering mechanisms (except grain barrier scattering), and mobility limited by each scattering mechanisms (except grain barrier scattering). However, scattering inside grain and at grain barrier occur in different position. So, Matthiessen's rule can't be adopted for them. To calculate the combined mobility, equivalent circuit as shown in Fig. 4-4 is considered. Grain barrier scattering can occur in the depletion area only, and scattering inside bulk occur inside bulk only except the depletion area. The combined mobility μ_{total} can be described as (4-15).

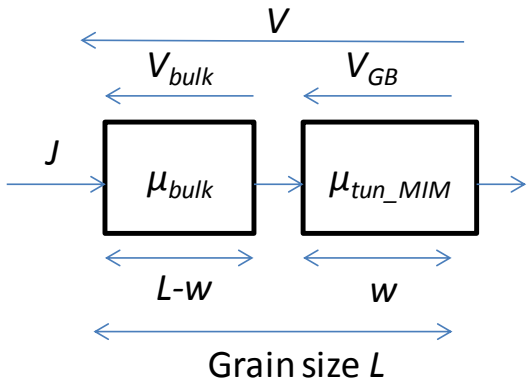

Fig. 4-4 Schematic of electrically connected bulk and grain barrier.

$$\mu_{total} = \frac{L}{\frac{L-w}{\mu_{bulk}} + \frac{w}{\mu_{tun\_MIM}}} \quad (4\text{-}15)$$

4.2.6 Review of the prior studies of scattering mechanisms

Koida et al. analyzed the scattering mechanisms of In_2O_3:H. They reported that the measured mobility shows good agreement with the mobility limited by ionized impurity scattering in carrier concentration 1.7 ~ 4.6x10^{20} cm^{-3}[2].

Ellmer et al. analyzed the dependence of mobility on carrier concentration in case of polycrystalline ZnO:Al and ITO[4], [11]. They used the empirical curve (eq.(4-16)) that Masetti et al. proposed[33], for describing the bulk mobility. In addition to that, Seto model was adopted to describe the grain barrier scattering. They concluded that ionized impurity scattering is dominant in higher carrier concentration than 10^{20} cm^{-3}, and grain barrier scattering is dominant in lower carrier concentration region, in both ZnO and ITO. But the grain barrier scattering becomes dominant in rather higher carrier concentration (10^{18}~10^{19} cm^{-3}) in case of ZnO than ITO (10^{17} cm^{-3}). This difference was attributed to the trap density of grain boundaries.

$$\mu^{Ma} = \mu_{min} + \frac{\mu_{max} - \mu_{min}}{1 + \left(n/n_{ref}\right)^{\alpha_1}} - \frac{\mu_1}{1 + \left(n_{ref2}/n\right)^{\alpha_2}} \quad (4\text{-}16)$$

However, the empirical formula of Masetti (eq.(4-16)) was made for device simulation, and it doesn't have physical meaning. And as described in subsection 4.2.4, it is questionable to apply Seto model to degenerated semiconductors.

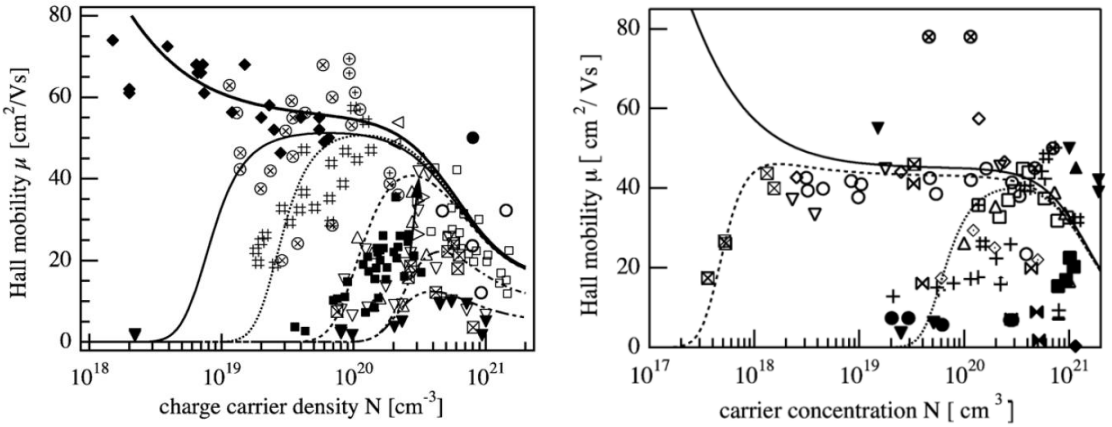

(a) (b)

Fig. 4-5 Hall mobilities of (a) undoped and doped ZnO films, and (b) ITO films. The detail of symbols are described in the paper[11].

Steinhauser analyzed the properties of ZnO:B[32] in similar to Ellmer et al[4], [11], but tunneling current was considered in addition to Seto model. As described in subsection 4.2.4, they used a parameter l_{tun} to adjust the tunneling current. However, the physical meaning of l_{tun} is not clear.

Minami et al. explained $\mu - n$ relationship of ZnO:Al in higher carrier concentration region using Brooks-Herring theory with considering degeneracy and non-parabolicity of the conduction band (same as eq.*(4-4)*)[34]. They also explained $\mu - n$ relationship in lower carrier concentration region using Seto formula[35] which is not applicable to degenerated semiconductors, as shown in Fig. 4-6. Abdolahzadeh et al. reported similar results[36].

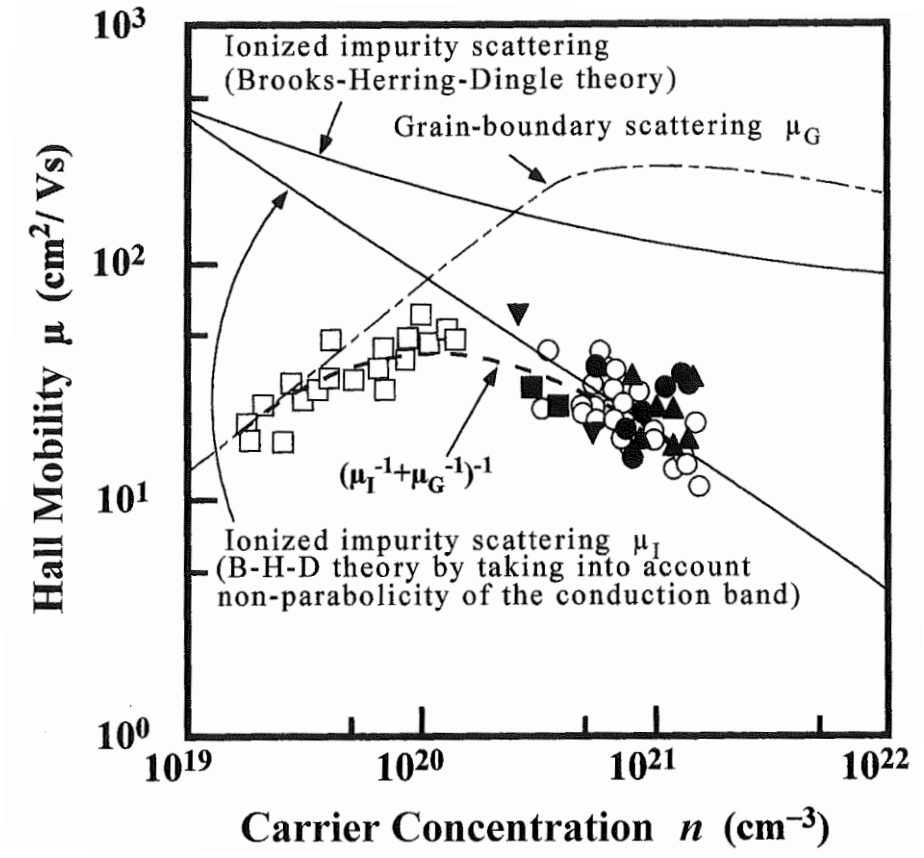

Fig. 4-6 Measured Hall mobility versus carrier concentration of undoped ZnO films (□) and impurity-doped ZnO films: ZnO:Al(○,●), ZnO:Ga(▲), ZnO:B(■), and ZnO:other(▼). The upper solid line represents ionized impurity scattering using the Brooks-Herring-Dingle (B-H-D) theory; the lower solid line shows the ionized impurity scattering $\mu_i - n$ relationship, and the dashed line shows the grain-boundary scattering $\mu_G - n$ relationship.[35]

In case of SnO_2, many researchers compared measured mobility and theoretically calculated mobility to explain the scattering mechanisms. Recently, Rey et al. analyzed scattering mechanisms by considering ionized impurity scattering, grain barrier scattering, and twin boundary scattering[21]. They concluded that grain barrier scattering or ionized impurity scattering can prevail over the other depending on the

grain size and doping level. However, they recognized barrier height is $E_B - (E_F - E_C)$. As explained in the subsection 4.2.4, this contradicts with the concept of barrier model shown in Fig. 4-1.

The dominant scattering mechanisms of In_2O_3, ZnO, and SnO_2 based TCO are summarized in Table 4-2. In case of In_2O_3 and ZnO, scattering mechanisms are understood as Table 4-2. However, the scattering mechanisms is not established yet in case of SnO_2[37]. In this thesis, we will analyze the dependence of mobility of SnO_2:F on both carrier concentration and temperature, theoretically, and study which scattering mechanisms are dominant.

	High n region ($>10^{20}$ cm^{-3})	Low n region (10^{18} ~$10^{19}$$cm^{-3}$)	Note
In_2O_3	Ionized impurity	Grain barrier scattering is not dominant	Grain barrier scattering becomes dominant in 10^{17} cm^{-3}
ZnO	Ionized impurity	Grain barrier(*1)	(*1) The formula for non-degenerated is used.
SnO_2	Ionized impurity (*2)	Grain barrier(*3)	(*2)It is not established yet[21], [37]. (*3) The formula for degenerated[13] is not established.

Table 4-2 The dominant scattering mechanisms of various TCO are shown.

4.3 Comparison with Experiments and Theories

As shown in Chapter 3, Hall mobility and fraction of (301)-oriented crystallite have strong positive correlation. And the fraction of (301)-oriented crystallite tends to be large if deposition temperature is set around 380 °C. Therefore in this subsection, we will analyze the scattering mechanisms of FTO samples which were deposited at between 340 and 420 °C in order to minimize the difference of crystallite orientation. Deposition period were fixed to 20 min, and thickness were around 800nm. $SnCl_4$ and H_2O were fed to LPCVD chamber by bubbling method using N_2 carrier gas. The flow rate of $SnCl_4$ and H_2O were set to 2 sccm and 100 ~ 400 sccm respectively, excluding carrier N_2 gas. HF was directly vaporized and fed to chamber. The flow rate of HF was set to 1 ~ 48 sccm. The pressure of the chamber was kept 100 Pa. All samples were annealed at 400 °C and N_2 1atm, for 10 min before evaluation.

4.3.1 Dependence of Mobility on Carrier Concentration (Experimental data)

Fig. 4-7 shows the relation of Hall mobility and carrier concentration of FTO samples fabricated by LPCVD (this work), APCVD(Ref [38][39]). At carrier concentration around $1x10^{20}$ cm^{-3}, the highest mobility 81.3 cm^2/Vs was observed. At lower carrier concentration less than $1x10^{20}$ cm^{-3}, mobility drops rapidly. And at higher carrier concentration higher than $1x10^{20}$ cm^{-3}, mobility also drops.

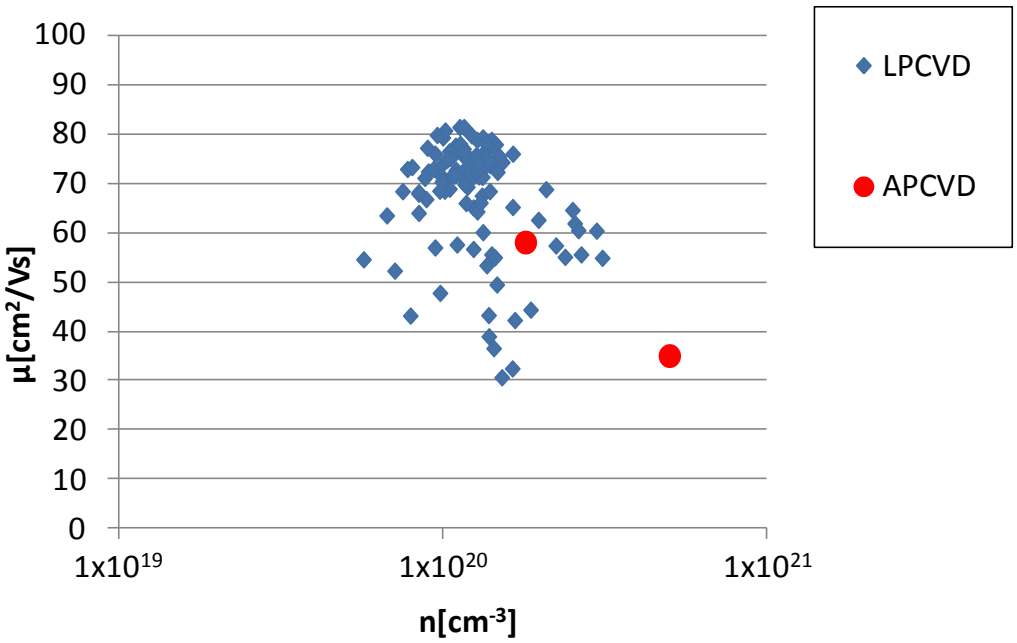

Fig. 4-7. Hall mobility versus carrier concentration plot of FTO films deposited by LPCVD and APCVD[38][39]. All LPCVD samples were deposited between 340 to 400 °C, deposition period is 20 min, and HF flow rate was not equal to 0 sccm. (In these conditions, (301) is dominant.)

4.3.2 Dependence of Mobility on Temperature (Experimental Data)

Temperature dependence provides important information about scattering mechanisms. So, we measured dependence of mobility on temperature. Two sets of samples were measured. One is the samples (named "HF-dependence") which HF flow rate was varied. Other conditions were kept same, so that the fraction of crystallite orientation were almost same. The other is the samples (named "T-dependence") which deposition temperatures were varied in order to make wide carrier concentration range. But the preferred orientation of crystallite were not same. The list of these samples are shown in Table 4-3. The fraction of (hkl)-oriented crystallite measured by XRD are shown in Fig. 4-9. As described above, the samples of HF-dependence have similar

crystallite orientation.

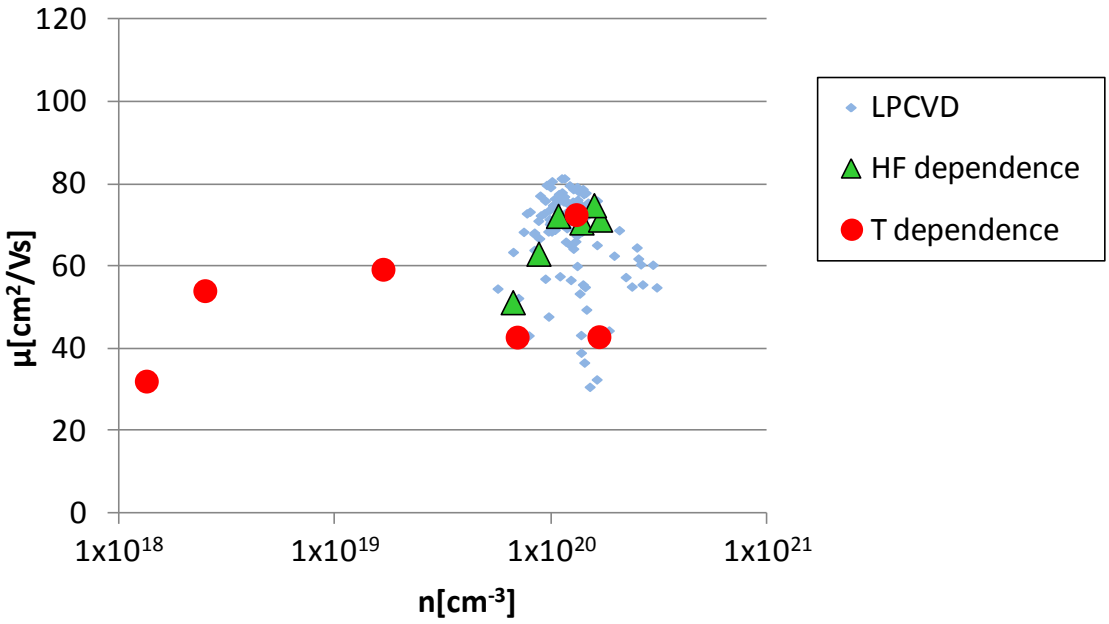

Fig. 4-8 Samples measured the dependence of mobility on temperature.

	Deposition temperature	HF/SnCl4	Thickness [nm]	n[x$10^{19}$$cm^{-3}$]	μ[cm^2/Vs]
HF-dependence	380	1	832.9	6.70	51.2
	380	2	865.2	8.81	63.0
	380	4	876.1	10.9	72.2
	380	8	824.2	13.9	70.6
	380	16	830.3	17.0	71.3
	380	24	858.7	15.9	74.8
T- dependence	380	4	850.2	13.2	72.5
	450	4	1007.1	16.8	42.8
	500	4	786.6	7.02	42.7
	550	4	759.0	1.68	59.2
	600	4	575.1	0.252	54.0
	625	4	696.6	0.135	32.0

Table 4-3 The properties of the samples measured at room temperature.

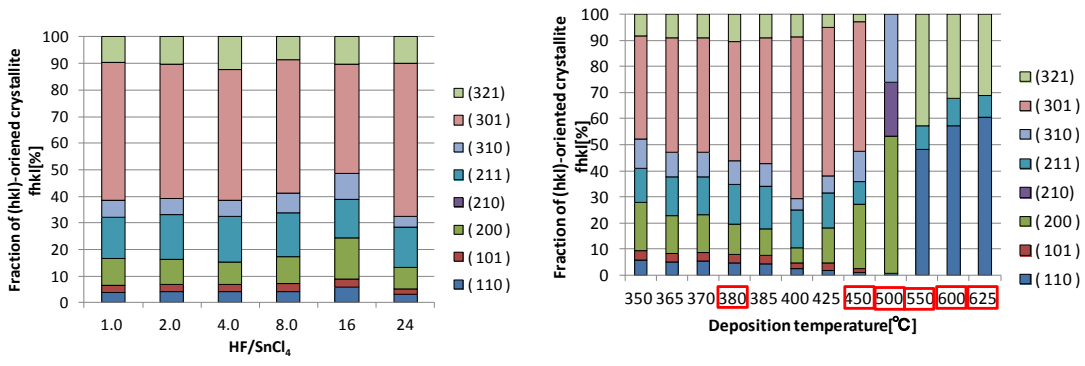

(a) (b)

Fig. 4-9 Fraction of (hkl)-oriented crystallite f_{hkl}(%) of the sample sets of (a)

HF-dependence and (b) T-dependence. In T-dependence, red box means the samples which were measured the dependence on temperature.

The temperature dependence of mobility and carrier concentration on temperature are shown in Fig. 4-10 for HF-dependence, and Fig. 4-11 for T-dependence. From Fig. 4-10, all samples are found to be degenerated semiconductors because carrier concentrations are constant in all temperature. The mobility of all samples monotonically decrease as temperature increases. From Fig. 4-11, carrier concentrations weakly depend on temperature in case that deposition temperature is higher than 550 °C. In this case, carrier concentration is less than $2x10^{19}$ cm^{-3}. The mobility with carrier concentration less than $2x10^{19}$ cm^{-3} increase as temperature increases, while other samples have opposite dependence.

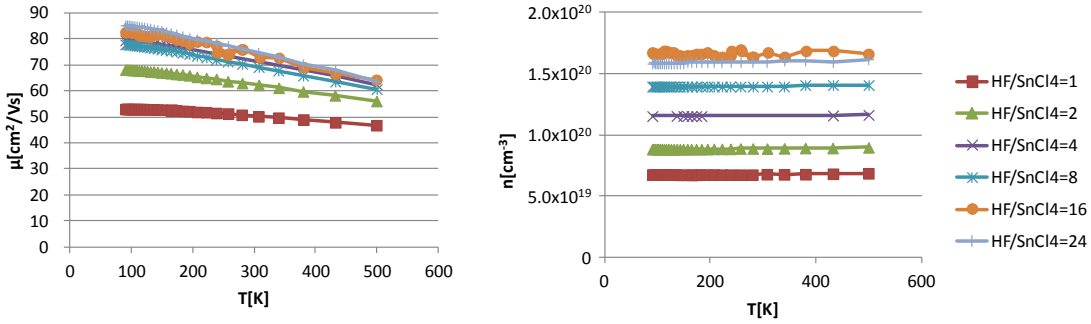

(a) (b)

Fig. 4-10 The dependence of (a) mobility and (b) carrier concentration on temperature. The samples were deposited with various HF flow rate. (HF-dependece)

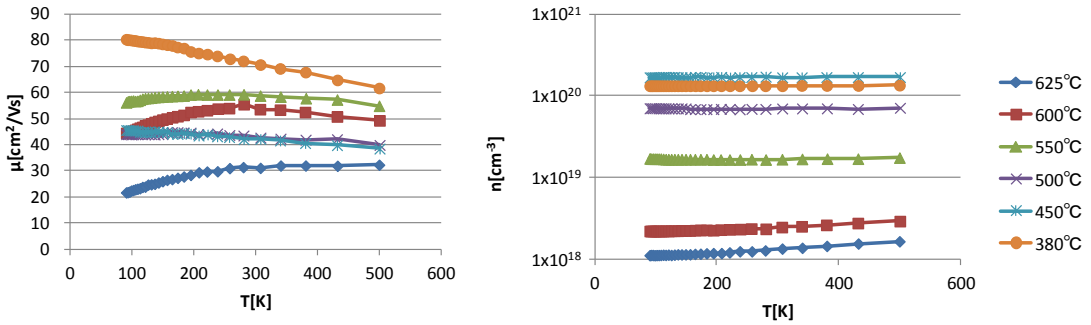

(a) (b)

Fig. 4-11 The dependence of (a) mobility and (b) carrier concentration on temperature. The samples were deposited in various temperature. (T-dependence)

4.3.3 Comparison with Theoretical Curves and Experimental Value

From Fig. 4-10(a), the mobility of all "HF-dependence" samples decrease as temperature increases. If thermionic emission current is dominant, mobility should increase as temperature increases, although there is no established theory of thermionic emission current in degenerated semiconductors. Therefore, we can understand that thermionic emission is negligibly small, and we consider the tunneling current only for

grain barrier scattering.

Theoretical curves and experimental data are plotted in Fig. 4-12. Theoretical curves are calculated by eq.*(4-1)*(μ_{Hopt}), eq.*(4-3)*(μ_{Hac}), eq.*(4-4)*(μ_{ii}), eq.(4-13) ($\mu_{\mathrm{tun\_MIM}}$), and eq.(4-15) (μ_{total}). In this calculation, all parameters are described in Table 4-1 except grain size L and trap density N_t. Static dielectric constant ε_s is averaged for $\parallel$ c and $\perp$ c. High frequency permittivity ε_∞ are varied around 4, so we set $\varepsilon_\infty = 4.0$. L is set to 200 nm roughly decided from SEM image (as described in 4.3.4). N_t is set to 4.5x10^{12} cm^{-2} to adjust the calculation to the experimental data. Trap density of various TCO were reported as Table 4-4. The values are scattered, but 4.5x10^{12} cm^{-2} may be adequate range, although most reports adopted the formula of Seto(eq.(4-8)), which is not applicable to degenerated semiconductors, to derive the trap density N_t.

Theoretical calculation roughly agrees with the sample properties, although there is only one parameter N_t. We can understand what scattering mechanism limit the mobility. At lower carrier concentration region below 1x10^{20} cm^{-3}, grain barrier scattering limits the total mobility. At higher carrier concentration region above 1x10^{20} cm^{-3}, ionized impurity scattering limits the total mobility.

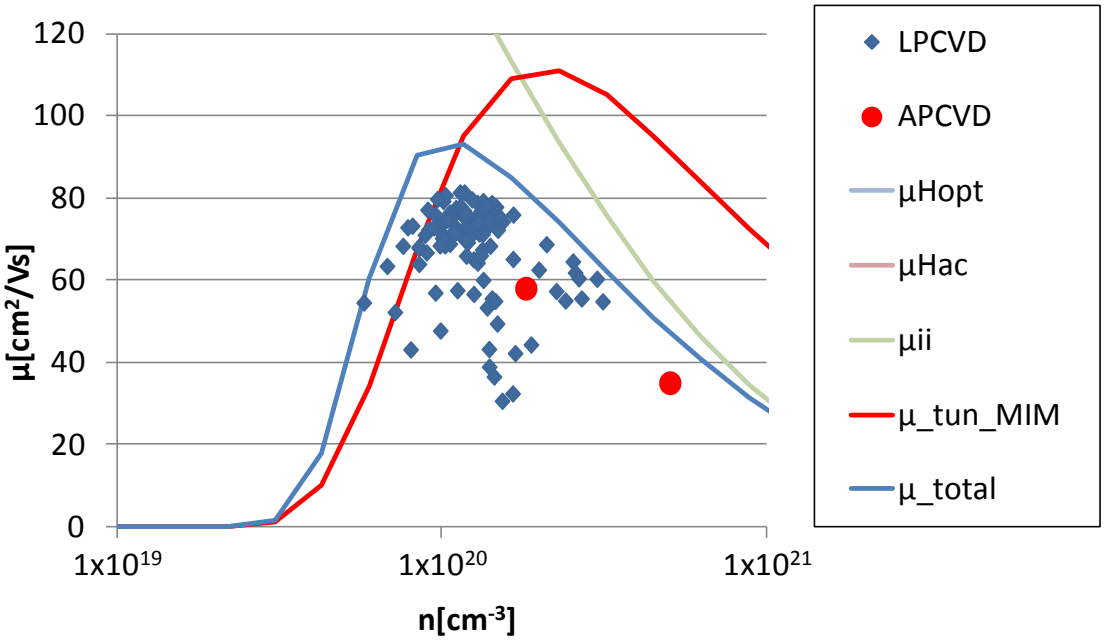

Fig. 4-12 Comparison with theoretical curves and experimental data. Eq.*(4-1)*(μ_{Hopt}), eq.*(4-3)*(μ_{Hac}), eq.*(4-4)*(μ_{ii}), eq.(4-13) ($\mu_{\text{tun\_MIM}}$), and eq.(4-15) (μ_{total}) are used. μ_{Hopt}(=310 cm^2/Vs) and μ_{Hac}(9230 cm^2/Vs) are located outside the graph.

Film:dopant	Growth	Method	Excitation (U_{dis} [V])	Q_t [cm^{-2}]
ZnO:Al	Epitaxial	MS	RF (200)	1.3×10^{13}
ZnO:Al	On glass	RMS	DC (425)	3×10^{13}
ZnO:Al	On glass	RMS	MF (340)	3×10^{13}
ZnO	On glass	MS*	RF	7×10^{12}
ZnO:Al,Ga	Epitaxial	PLD	–	5×10^{12}
ZnO	Epitaxial	PLD	–	1.5×10^{13}
In_2O_3:Sn	On glass	RMS/MS	DC (400) RF (250)	1.5×10^{12}
In_2O_3:Sn	On glass	MS	RF-diode (2000)	2.5×10^{13}
SnO_2:F,Cl	On glass	SP	–	4×10^{12}
$CdIn_2O_4$	On glass	RMS	DC (2000)	1.5×10^{13}

Table 4-4 Trap density Q_t (=N_t), deposition method and discharge voltage V_{dis} of epitaxial and polycrystalline TCO films. (Taken from Ref.[11])

Fig. 4-13 shows the dependence of mobility of "HF-dependence" samples on temperature. Both experimental and theoretical data have similar dependence on temperature that mobility decrease as temperature increases. As carrier concentration decreases, the dependence on temperature becomes flatter. Fig. 4-14 shows the dependence of the calculated mobility of each scattering mechanism and the measured mobility on temperature in case of (a) HF/$SnCl_4$=24 (Carrier concentration is 1.59x10^{20} cm^{-3}) and (b) HF/$SnCl_4$=1 (Carrier concentration is 5.83x10^{19} cm^{-3}). The temperature dependence can be attributed to optical phonon scattering, because lattice vibration increases as temperature increases, while ionized impurity scattering and tunneling are constant against temperature. We can understand that μ_{total} is limited by μ_{ii} from Fig. 4-14(a), and μ_{total} is limited by μ_{tun_MIM} from (b).

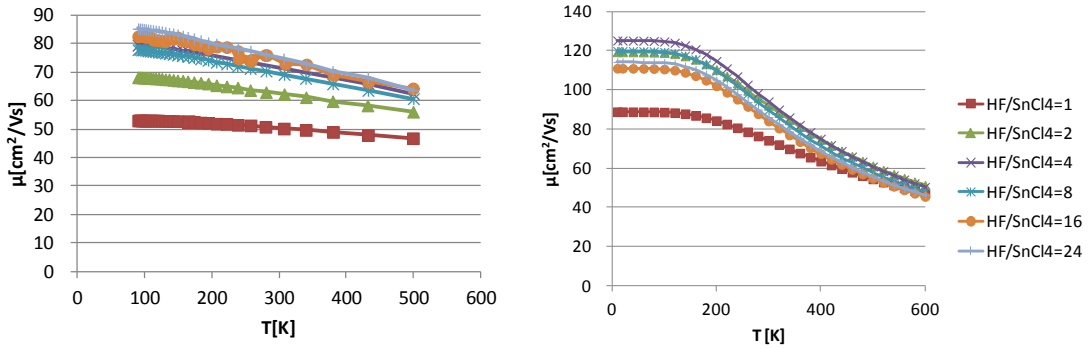

(a) (b)

Fig. 4-13 Dependence of mobility of "HF-dependece" samples on temperature. (a) Experimental results, and (b) Theoretical calculated results.

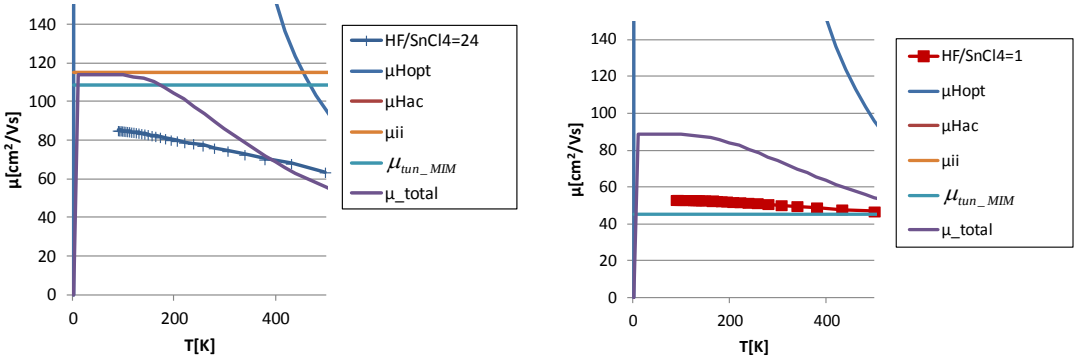

(a) (b)

Fig. 4-14 The dependence of the calculated mobility and the measured mobility on temperature in case of (a) $HF/SnCl_4$=24 and (b) $HF/SnCl_4$=1.

Despite the difference of crystallite orientation of the "T-dependence" samples, we also compare the dependence of mobility of the samples on temperature as shown in Fig. 4-15. In samples with carrier concentration above $7x10^{19}$ cm^{-3} (Deposition temperature is lower than 500°C), dependence of mobility on temperature of both experimental and theoretical data show similar tendency as "HF-dependence" samples. On the other hand, samples with carrier concentration below $2x10^{19}$ cm^{-3} (Deposition temperature is higher than 550°C), the observed mobility increase as temperature increases, while the calculated mobility are almost 0. These observed dependence can't be explained by the tunneling current. Other conduction mechanisms such as thermionic emission should be considered. However, crystallite orientation are varied in "T-dependence samples" as shown in Fig. 4-9 and Chapter 3, it is difficult to analyze the dependence of mobility of "T-dependence" samples.

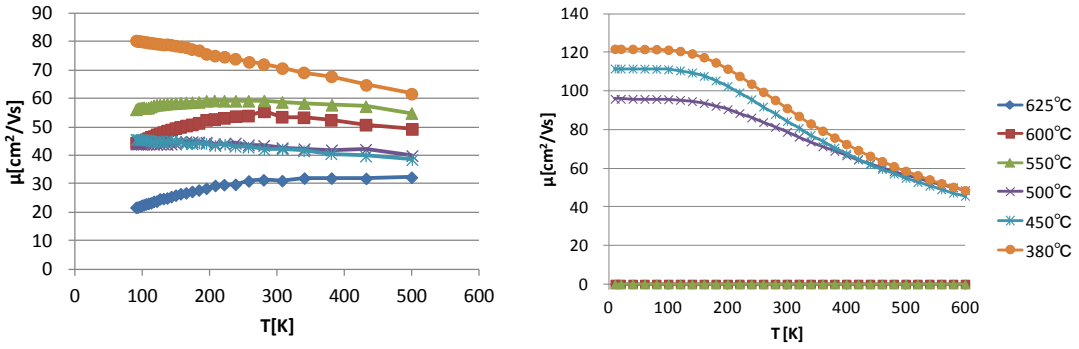

(a) (b)

Fig. 4-15 Dependence of mobility of "T-dependece" samples on temperature. (a) Experimental results, and (b) Theoretical calculated results.

Watching Fig. 4-8, the mobility decreases as carrier concentration decreased from $1x10^{20}$ cm^{-3} to $5x10^{19}$ cm^{-3}, and shows bottom around $5x10^{19}$ cm^{-3}. This bottom also reported by Toyosaki et al.[14] for epitaxial SnO_2:Ta and by Ellmer et al.[4] for ZnO:Al. Ellmer explained this bottom that grain barrier height becomes maximum in this point by using Seto model[24]. In this explanation, whole grain should be depleted where the barrier height is max. However, carrier concentration is still higher than 10^{19} cm^{-3} and degenerately doped. Therefore this explanation is questionable. Beside the explanation, the dependence of mobility and carrier concentration on temperature changes around $n=5x10^{19}$ cm^{-3} as shown in Fig. 4-11. Above $n=5x10^{19}$ cm^{-3}, mobility decreases and carrier concentration doesn't change as temperature increases. Below $n=5x10^{19}$ cm^{-3}, mobility and carrier concentration increase as temperature increases. In order to explain the dependency below $n=5x10^{19}$ cm^{-3}, considering thermionic emission may be needed. However, theory of thermionic emission in degenerated semiconductors has not been established.

4.3.4 Dependence of Mobility on Grain Size using Thick Non-doped Layer

As discussed above, scattering mechanisms of SnO_2:F thin films are analyzed, and we found that (1) ionized impurity scattering is dominant in higher carrier concentration than $1x10^{20}$ cm^{-3}, (2) grain barrier scattering through tunneling is dominant in lower carrier concentration than $1x10^{20}$ cm^{-3}. Simulation results of various trap density N_t and grain size L are shown in Fig. 4-16. As trap density N_t decreases or grain size L increases, the mobility in lower carrier concentration will increase.

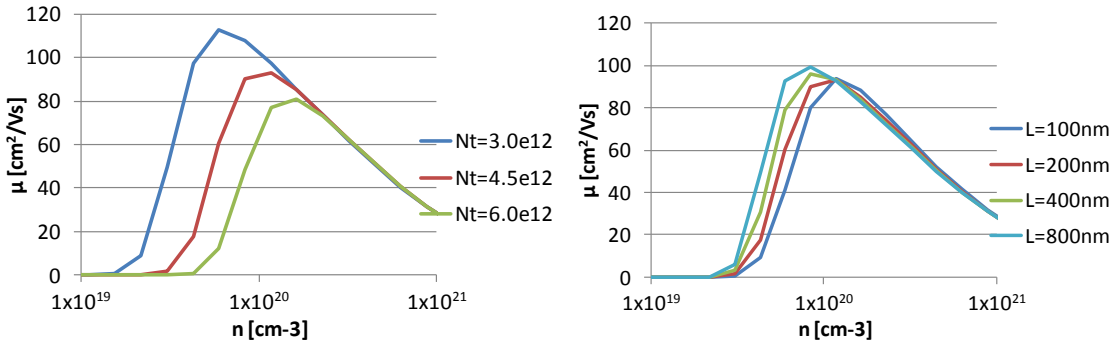

(a) (b)

Fig. 4-16 Simulation results of (a) various trap density N_t where L=200 nm and (b) various grain size L where N_t=4.5x10^{12} cm^{-2}.

To confirm the simulation result, we performed the experiment of changing grain size. The concept of the experiment is shown in Fig. 4-17. As shown in Chapter 3, the fraction of (301) orientated crystallite becomes larger as film is thicker. This means that (301) oriented crystallite is dominant in the top part of the films thicker than the certain thickness. And thin film has smaller grain size, and thick film has larger grain size. By comparing the properties of the top of the films of thin film and thick film, we can observe the dependence on grain size while the crystallite orientation is kept to

(301). However, non-doped layer also has certain amount of carriers of unintentionally doped. To subtract the contribution of the non-doped layer, we used the formula of Petritz[40] as explained in Chapter 3. By this method, we can change the grain size but keep the preferred crystallite orientation same.

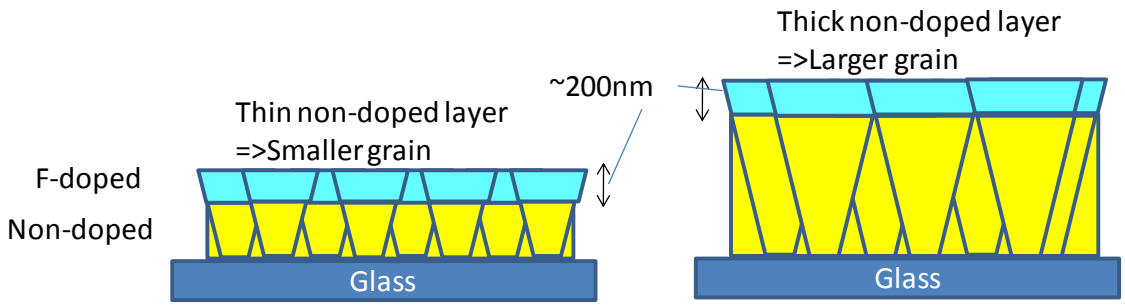

Fig. 4-17 Schematic of the experiment of changing grain size.

Non-doped layer is deposited on glass, and then F-doped layer is deposited without any interval. Deposition period of non-doped layer are 5, 10, and 20 min. Deposition period of F-doped layer are fixed to 5 min. The experimental conditions and the properties of non-doped / F-doped stacked samples are shown in Table 4-5. In this experiment, film thickness was measured by spectropic ellispometry using Semilab GES5E to minimize the measurement error.

Non-doped layer		5 min	10 min	20 min
		193.4 nm, 24.5 cm^2/Vs $7.9x10^{14}$ cm^{-2}	400.5 nm 23.3 cm^2/Vs $9.9x10^{14}$ cm^{-2}	795.3 nm 32.1 cm^2/Vs $1.4x10^{15}$ cm^{-2}
HF/SnCl4 (Non-doped layer + 5 min deposited Doped layer)	0.5	404.5 36.8 $2.2x10^{15}$	603.3 48.3 $2.1x10^{15}$	1028.6 52.9 $2.3x10^{15}$
	1	380.6 42.2 $2.8x10^{15}$	583.3 51.4 $2.6x10^{15}$	1003.6 60.5 $2.6x10^{15}$
	2	388.0 50.6 $3.3x10^{15}$	595.5 62.3 $3.3x10^{15}$	1004.5 68.7 $3.2x10^{15}$
	4	396.4 57.1 $3.8x10^{15}$	595.1 65.9 $3.8x10^{15}$	1027.7 72.3 $4.4x10^{15}$
	8	387.6 55.1 $3.9x10^{15}$	598.0 60.0 $4.3x10^{15}$	1013.5 69.2 $4.7x10^{15}$
	16	388.9 40.2 $4.6x10^{15}$	601.3 44.3 $4.7x10^{15}$	1022.3 55.2 $5.5x10^{15}$
	24	385.5 33.3 $5.1x10^{15}$	606.2 34.0 $5.5x10^{15}$	1026.4 43.0 $5.7x10^{15}$

Table 4-5 The properties of the non-doped / F-doped stacked samples.

The fraction of (hkl) oriented crystallite f_{hkl} of non-doped layer samples with deposition period 5,10 and 20 min are shown in Fig. 4-18. As expected, f_{301} increases monotonically as film becomes thicker. Fig. 4-19 shows the fraction of (hkl) oriented crystallite f_{hkl} of non-doped/F-doped stacked samples. Deposition period of F-doped layer is fixed to 5min. Deposition period of non-doped are (a) 5min, (b) 10min, and (c)

20min. It can be seen that the fraction of crystallite orientation doesn't depend on $HF/SnCl_4$ ratio.

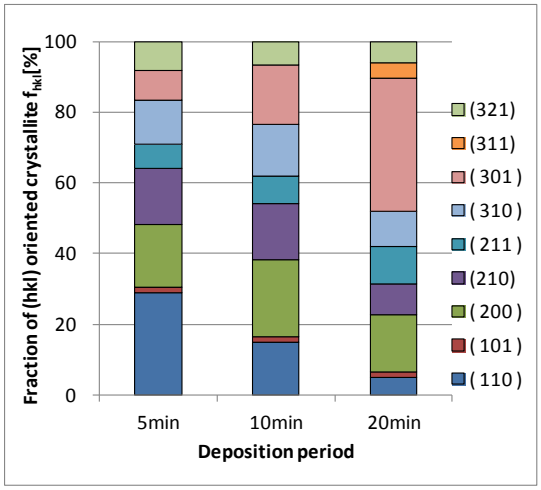

Fig. 4-18 The fraction of (hkl) oriented crystallite f_{hkl} of non-doped layer samples with deposition period 5,10 and 20 min.

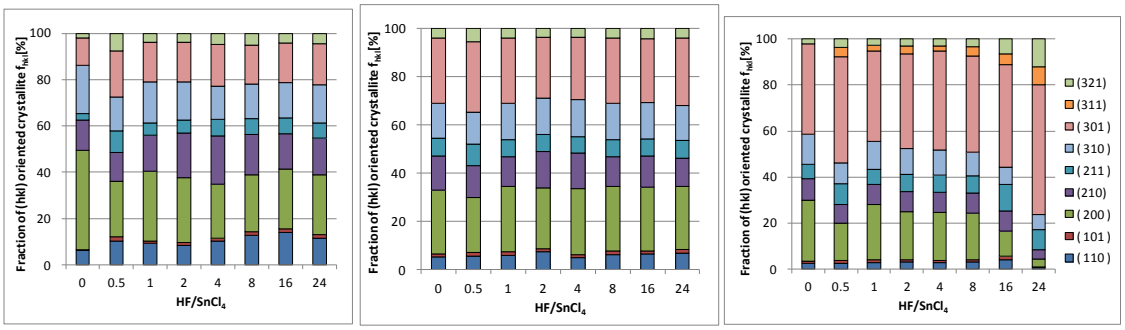

(a) (b) (c)

Fig. 4-19 The fraction of (hkl) oriented crystallite f_{hkl} of non-doped/F-doped stacked samples. Deposition period of F-doped layer is fixed to 5min. Deposition period of non-doped are (a) 5min, (b) 10min, and (c) 20min.

Using SEM images of non-doped / F-doped stacked samples shown in Fig. 4-20, grain size are measured based on BS EN 623-3:2001 which define the test method of grain size of ceramics. The result is shown in Fig. 4-21. The grain size are around 110,

150, and 220 nm for 5 , 10, and 20 min deposition of non-doped layer, respectively.

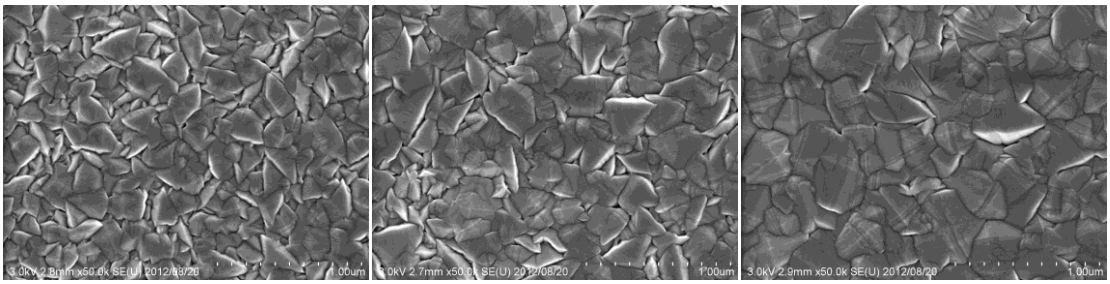

(a) (b) (c)

Fig. 4-20 Example of SEM images (top view) of non-doped / F-doped stacked samples of HF/SnCl4=1. Deposition time of non-doped layer are (a) 5 min, (b) 10 min, and (c) 20 min.

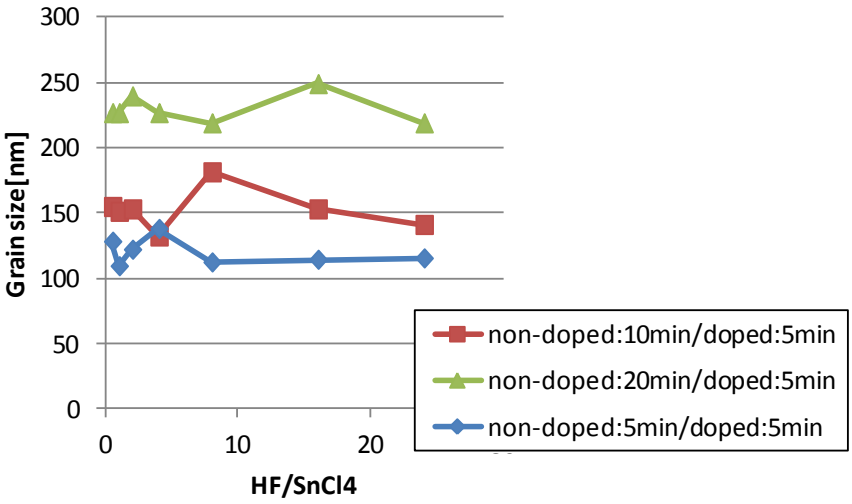

Fig. 4-21 Measured Grain size based on BS EN 623-3:2001 using SEM images.

The calculated mobility of the thin F-doped layer are shown in Fig. 4-22. It is clearly seen that the calculated mobility in lower carrier concentration region increase as the grain size increases, while the mobility in higher carrier concentration don't depend on the grain size. This behavior coincide our understanding of scattering mechanisms.

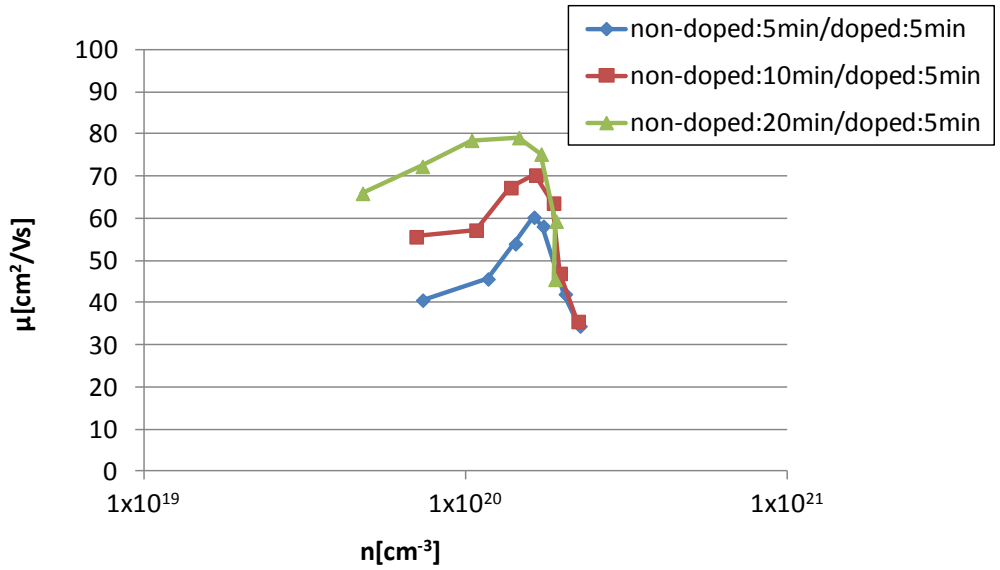

Fig. 4-22 The calculated mobility of the thin F-doped layer.

4.4 Conclusion

We have succeeded to simulate the dependence of the mobility both on carrier concentration and on temperature. With only one parameter, all properties can be roughly reproduced. From these results, we can understand the scattering mechanisms of SnO_2:F thin films as (1) ionized impurity scattering is dominant at higher carrier concentration than $1x10^{20}$ cm^{-3}, (2) grain barrier scattering through tunneling is dominant at lower carrier concentration than $1x10^{20}$ cm^{-3}. By using non-doped / F-doped stacked structure, we confirmed that the mobility at lower carrier concentration increase as the grain size become larger, while the mobility at higher carrier concentration don't depend on the grain size.

References

[1] S. Myong, J. Steinhauser, R. Schluchter, S. Fay, E. Vallatsauvain, a Shah, C. Ballif, and a Rufenacht, "Temperature dependence of the conductivity in large-grained boron-doped ZnO films," *Sol. Energy Mater. Sol. Cells*, vol. 91, no. 14, pp. 1269–1274, Sep. 2007.

[2] T. Koida, M. Kondo, K. Tsutsumi, A. Sakaguchi, M. Suzuki, and H. Fujiwara, "Hydrogen-doped In_2O_3 transparent conducting oxide films prepared by solid-phase crystallization method," *J. Appl. Phys.*, vol. 107, no. 3, p. 033514, 2010.

[3] T. Makino, Y. Segawa, a. Tsukazaki, a. Ohtomo, and M. Kawasaki, "Electron transport in ZnO thin films," *Appl. Phys. Lett.*, vol. 87, no. 2, p. 022101, 2005.

[4] K. Ellmer and R. Mientus, "Carrier transport in polycrystalline ITO and ZnO:Al II: The influence of grain barriers and boundaries," *Thin Solid Films*, vol. 516, no. 14, pp. 5829–5835, May 2008.

[5] Y. Shigesato and Y. Hayashi, "Doping mechanisms of tin-doped indium oxide films," *Appl. Phys. Lett.*, vol. 61, no. July, pp. 73–75, 1992.

[6] C. Yu, S. Chen, S. Sun, and H. Chou, "Influence of the grain boundary barrier height on the electrical properties of Gallium doped ZnO thin films," *Appl. Surf. Sci.*, vol. 257, no. 15, pp. 6498–6502, May 2011.

[7] B. Stannowski, F. Ruske, S. Neubert, S. Schönau, S. Ring, S. Calnan, M. Wimmer, O. Gabriel, B. Szyszka, B. Rech, and R. Schlatmann, "Potential of high-mobility sputtered zinc oxide as front contact for high efficiency thin film silicon solar cells," *Thin Solid Films*, Oct. 2013.

[8] T. Koida and M. Kondo, "High-mobility transparent conductive Zr-doped In_2O_3," *Appl. Phys. Lett.*, vol. 89, no. 8, p. 082104, 2006.

[9] T. Koida and M. Kondo, "Improved near-infrared transparency in sputtered In_2O_3-based transparent conductive oxide thin films by Zr-doping," *J. Appl. Phys.*, vol. 101, no. 6, p. 063705, 2007.

[10] M. Kamei and T. Yagami, "Heteroepitaxial growth of tin-doped indium oxide films on single crystalline yttria stabilized zirconia substrates," *Appl. Phys. ...*, vol. 64, no. 001, pp. 2712–2714, 1994.

[11] K. Ellmer and R. Mientus, "Carrier transport in polycrystalline transparent conductive oxides: A comparative study of zinc oxide and indium oxide," *Thin Solid Films*, vol. 516, no. 14, pp. 4620–4627, May 2008.

[12] S.-Y. Lee and B.-O. Park, "Structural, electrical and optical characteristics of SnO_2:Sb thin films by ultrasonic spray pyrolysis," *Thin Solid Films*, vol. 510, no. 1–2, pp. 154–158, Jul. 2006.

[13] J. Bruneaux, H. Cachet, M. Froment, and A. Messad, "Correlation between Structural and Electrical properties of Sprayed Tin Oxide films with and without Fluorine doping," *Thin Solid Films*, vol. 197, pp. 129–142, 1991.

[14] H. Toyosaki, M. Kawasaki, and Y. Tokura, "Electrical properties of Ta-doped SnO_2 thin films epitaxially grown on TiO_2 substrate," *Appl. Phys. Lett.*, vol. 93, no. 13, p. 132109, 2008.

[15] K. Ellmer, "Transparent Conductive Zinc Oxide and Its Derivatives," in *Handbook of Transparent Conductors*, D. S. Ginley, Ed. Boston, MA: Springer US, 2011, pp. 193–264.

[16] S. S. Devlin, *Physics and Chemistry of II-VI Compounds*. North-Holland, Amsterdam, 1967, p. 549.

[17] K. I. Hagemark and L. C. Chacka, "Electrical transport properties of Zn doped ZnO," *J. Solid State Chem.*, vol. 15, no. 3, pp. 261–270, 1975.

[18] J. Bardeen and W. Shockley, "Deformation Potentials and Mobilities in Non-Polar Crystals," *Phys. Rev.*, vol. 80, no. 1, pp. 72–80, Oct. 1950.

[19] K. Seeger, *Semiconductor Physics*, vol. 40. Berlin, Heidelberg: Springer Berlin Heidelberg, 1991.

[20] K. Ellmer, "Resistivity of polycrystalline zinc oxide films: current status and physical limit," *J. Phys. D. Appl. Phys.*, vol. 34, no. 21, pp. 3097–3108, Nov. 2001.

[21] G. Rey, C. Ternon, M. Modreanu, X. Mescot, V. Consonni, and D. Bellet, "Electron scattering mechanisms in fluorine-doped SnO_2 thin films," *J. Appl. Phys.*, vol. 114, no. 18, p. 183713, 2013.

[22] T. Pisarkiewicz, K. Zakrzewska, and E. Leja, “Scattering of charge carriers in transparent and conducting thin oxide films with a non-parabolic conduction band,” *Thin Solid Films*, vol. 174, pp. 217–223, 1989.

[23] C. Erginsoy, “Neutral Impurity Scattering in Semiconductors,” *Phys. Rev.*, vol. 79, no. 6, pp. 1013–1014, Sep. 1950.

[24] J. Seto, “The electrical properties of polycrystalline silicon films,” *J. Appl. Phys.*, vol. 46, pp. 5247–5254, 1975.

[25] R. E. Jones and S. P. Wesolowski, “Electrical, thermoelectric, and optical properties of strongly degenerate polycrystalline silicon films,” *J. Appl. Phys.*, vol. 56, no. 6, p. 1701, 1984.

[26] M. W. J. Prins, J. F. M. Cillessen, and L. F. Feiner, “Grain-boundary-limited transport in semiconducting SnO_2 thin films: Model and experiments,” *J. Appl. Phys.*, vol. 83, no. 2, p. 888, 1998.

[27] S. M. Sze and K. K. Ng, *Physics of Semiconductor Devices*. Wiley, 2006.

[28] D. H. Zhang and H. L. Ma, “Scattering mechanisms of charge carriers in transparent conducting oxide films,” *Appl. Phys. A*, vol. 62, p. 487, 1996.

[29] I. H. Kim, J. H. Ko, D. Kim, K. S. Lee, T. S. Lee, J. -h. Jeong, B. Cheong, Y.-J. Baik, and W. M. Kim, “Scattering mechanism of transparent conducting tin oxide films prepared by magnetron sputtering,” *Thin Solid Films*, vol. 515, no. 4, pp. 2475–2480, Dec. 2006.

[30] T. J. Coutts, D. L. Young, and T. A. Gessert, "Modeling, Characterization, and Properties of Transparent Conducting Oxides," in *Handbook of Transparent Conductors*, D. S. Ginley, Ed. Boston, MA: Springer US, 2011.

[31] J. G. Simmons, "Generalized Formula for the Electric Tunnel Effect between Similar Electrodes Separated by a Thin Insulating Film," *J. Appl. Phys.*, vol. 34, no. 6, p. 1793, 1963.

[32] J. Steinhauser, "Low Pressure Chemical Vapor Deposited Zinc Oxide for Silicon Thin Film Solar Cells Optical and Electrical Properties," Lulu.com, 2008.

[33] G. Masetti, M. Severi, and S. Solmi, "Modeling of carrier mobility against carrier concentration in arsenic-, phosphorus-, and boron-doped silicon," *IEEE Trans. Electron Devices*, vol. ED-30, p. 764, 1983.

[34] T. Minami, H. Sato, and K. Ohashi, "Conduction mechanism of highly conductive and transparent zinc oxide thin films prepared by magnetron sputtering," *J. Cryst. Growth*, vol. 117, pp. 370–374, 1992.

[35] T. Minami, "New n-Type Transparent Conducting Oxides," *MRS Bull.*, vol. 25, no. 8, pp. 38–44, 2000.

[36] A. A. Ziabari and S. M. Rozati, "Carrier transport and bandgap shift in n-type degenerate ZnO thin films : The effect of band edge nonparabolicity," *Phys. B Phys. Condens. Matter*, vol. 407, no. 23, pp. 4512–4517, 2012.

[37] K. L. Chopra, S. Major, and D. K. Pandya, “Transparent conductors—A status review,” *Thin Solid Films*, vol. 102, no. 1, pp. 1–46, Apr. 1983.

[38] M. Mizuhashi, Y. Gotoh, K. Adachi, and Y. Gotoh, “Texture Morphology of SnO_2:F films and cell reflectance,” *Jpn. J. Appl. Phys.*, vol. 27, no. 11, pp. 2053–2061, 1988.

[39] M. Kambe, K. Sato, D. Kobayashi, Y. Kurokawa, S. Miyajima, M. Fukawa, N. Taneda, A. Yamada, and M. Konagai, “TiO_2 -Coated Transparent Conductive Oxide (SnO_2 :F) Films Prepared by Atmospheric Pressure Chemical Vapor Deposition with High Durability against Atomic Hydrogen,” *Jpn. J. Appl. Phys.*, vol. 45, no. No. 10, pp. L291–L293, Mar. 2006.

[40] R. Petritz, “Theory of an experiment for measuring the mobility and density of carriers in the space-charge region of a semiconductor surface,” *Phys. Rev.*, vol. 110, p. 1254, 1958.

Chapter 5[1], [2]

5 Fabrication of SnO_2:F Films with Both Very High Haze and High Mobility

5.1 Introduction

For front transparent conductive oxide (TCO) films used in thin-film silicon solar cells, high transmittance in all wavelength, low sheet resistance and high haze value are required. To achieve high transmittance and low sheet resistance, the carrier concentration and mobility of TCO need to be low and high, respectively. Fig. 5-1 shows simulation results of free carrier absorption based on Drude model[3], [4]. From Fig. 5-1(a), the absorption is almost the same in various carrier concentration if the mobility and the product of carrier concentration and film thickness $(n \times d)$ are fixed. From Fig. 5-1(b), the absorption becomes higher rapidly as mobility decreases. So, higher mobility is very important to achieve lower absorption especially in the near-infrared (NIR) region.

TCOs with high mobility of around 80 cm^2/Vs have been reported by several groups including ours[5]–[7] for SnO_2 based TCO. But all of them have flat surfaces and low haze values. Recently, W-textured ZnO films fabricated by metal–organic chemical vapor deposition (MOCVD) on reactive ion etching (RIE) processed glass substrates are reported to have very high haze value[8]. However, the mobility of MOCVD B-doped ZnO is not high enough. Therefore, we have developed F-doped SnO_2 (FTO) with higher mobility and higher haze value using RIE-etched substrate.

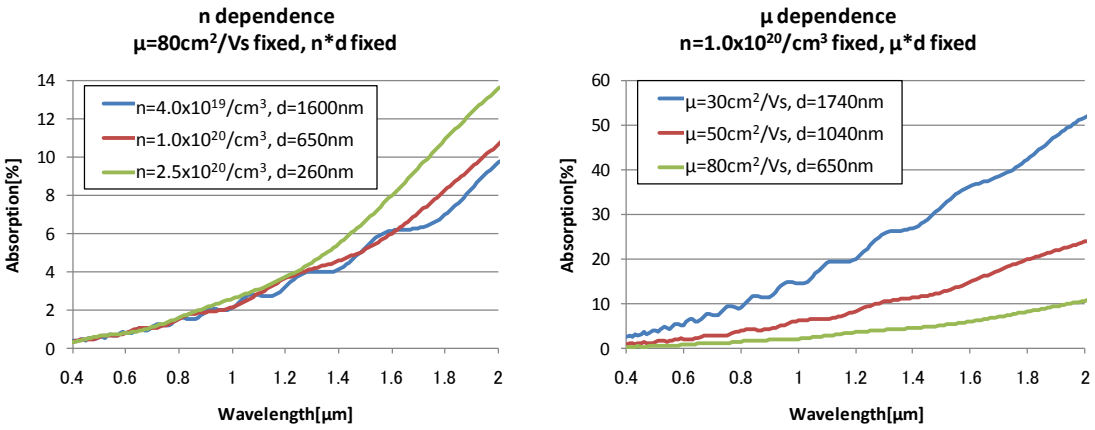

(a) (b)

Fig. 5-1: (a) n dependence. μ is fixed. $(n \times d)$ is fixed to constant. (b) μ dependence. n is fixed. So, $(\mu \times d)$ is fixed.

In all experiments, 0.7-mm-thick alkaline-free glass substrates (Corning 7059) were used. Before FTO-film deposition, these substrates were etched in SAMCO RIE-10NR by a standard RIE process using carbon tetrafluoride (CF_4) as the etching gas. The glass etching time was varied from 0 to 90 min. Power and CF_4 flow rate during RIE are set as 200 W and 15 sccm respectively. FTO was deposited on both RIE and flat substrates using low pressure chemical vapor deposition (LPCVD). Detail of the LPCVD deposition machine is described in Chapter 3. $SnCl_4$ and H_2O were vaporized using the bubbling method. N_2 was used as the carrier gas. HF, which was used to dope fluorine into SnO_2, was vaporized directly from liquid HF. These three gases were mixed downstream of the showerhead to avoid the pipe clogging. The calculated flow rates (excluding that of the carrier N_2 gas) of $SnCl_4$, H_2O, and HF were set at 2, 400 and 0~8 sccm, respectively. The deposition period was varied from 20 to 90 min. In all the experiments, the chamber pressure was kept at 100 Pa during deposition. During

deposition, the temperature of the glass substrate was maintained at 360 or 380°C. All samples were annealed at 400°C in 100% N_2 (1 atm) for 10 min before evaluation. We have tried two film structures. One is consisted entirely of F-doped layer while the other is stacked structure of non-doped layer (substrate side) and F-doped layer (top side). Non-doped and F-doped layers are deposited continuously by only changing HF flow from 0 to 8sccm.

Film thickness on flat substrates were measured using a DEKTAK M6, which is a common use apparatus. Film thickness on RIE substrates were not measured. However, since the same conditions were used for FTO deposited both on RIE and flat substrates, their film thickness on RIE and flat substrates were supposed to be the same. In fact, we confirmed that the thickness on RIE and flat substrates with same deposition conditions were same by SEM cross-sectional observation. The electrical resistivity ρ, the carrier concentration n and the mobility μ of the films were obtained by Hall measurements in the van der Pauw configuration using BioRad HL5500.

Transmittance (T), reflectance (R), absorption(A) and haze ratio were measured by PerkinElmer Lambda950 spectrometer. It is difficult to measure T, R, and A of textured FTO films accurately because the light will be scattered by the textured surface. T, R, and A of FTO films on flat substrates can be measured accurately by adopting IM technique[9], which suppresses the light scattering effect at FTO films /air interface. However, it is impossible to measure T, R, and A of FTO films on RIE substrates accurately even if IM technique is adopted, because light is scattered at both FTO films / air and glass / FTO films interfaces. We will discuss the problem in Chapter 6 in detail. For comparison reason, IM technique has also been applied to FTO films fabricated on flat substrates. As explained in the introduction section 5.1, free carrier

absorption can be related to the product of carrier concentration and film thickness($n \times d$). We have confirmed that $(n \times d)$ and absorption have a linear correlation based on the measured data of FTO films on flat substrates. Here, we assumed that we can also estimate the absorption of FTO films on RIE substrates from $(n \times d)$ obtained by Hall measurements.

SEM images were observed with Hitachi SU-70 or S-3400. Samples were cleaved and coated with osmium and platinum before SEM observation. The thicknesses of osmium and platinum were approximately 3 and 1 nm, respectively.

Cell evaluations were performed in the conditions described here. Before cell fabrication, thin ZnO:B film by MOCVD or ZnO:Al films by sputtering was deposited on FTO in order to avoid SnO_2 reduction by atomic hydrogen[6]. μc-Si:H solar cells with an area of 0.086 cm^2 were fabricated with the layer sequence: TCO / p-μc-SiO:H / i- μc-Si:H / n- μc-SiO:H / Ag / Al by a conventional plasma enhanced chemical vapor deposition (PECVD) system using SiH_4, H_2, B_2H_6, PH_3 and CO_2 as source gases, at the substrate temperature of about 200 °C. The i-layer thickness was about 1μm. Ag and Al layers were deposited by evaporation method. The current-voltage (I-V) characteristics of the fabricated solar cells were measured under 1-sun (AM 1.5, 100mW/cm^2) illumination. The external quantum efficiency (EQE) measurement was performed to estimate the spectral response of these solar cells. In case of cell evaluation with tandem structure, a-Si:H/μc-Si:H solar cells with an area of 0.23 cm^2 were fabricated with the layer sequence: TCO / p-a-SiC:H / i-a-Si:H / n-μc-SiO:H / p-μc-SiO:H / i- μc-Si:H / n- μc-SiO:H / Ag / Al. The thickness of i-a-Si:H and i-μc-Si:H are 300 nm and 2 μm, respectively.

5.2 Mobility of SnO_2:F on RIE Etched Glass Substrates

Fig. 5-2(a) shows the mobility dependence on RIE time. The pressure of RIE was fixed to 7 Pa. We found that for the film thicknesses of around 900 nm the mobility dropped from 75 to 36 cm^2/Vs when the glass surface has been textured by RIE. Sheet resistance of FTO films on RIE substrates are measured to be high, because the film is winding as shown in Fig. 5-2(b). As the result, low mobility are observed on RIE substrates. However, the low mobility doesn't correspond to the correct property of the film material itself. So, we call it as "Effective mobility", here. We also found that the film thickness should be much thicker than 2612 nm in order to suppress the drop of the effective mobility. It can be understood that the valley of RIE substrate is filled with film and the film surface becomes flatter. From this result, it is clear that much thicker film than 2612 nm is required to avoid the drop of the effective mobility.

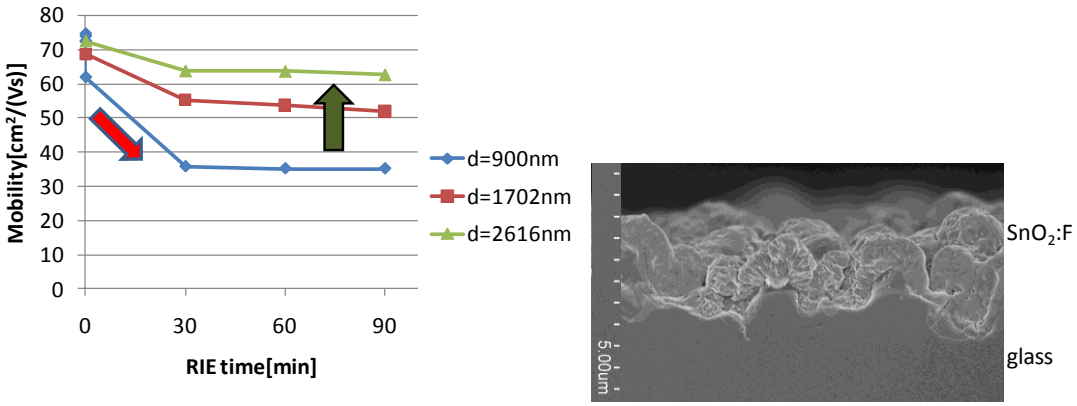

(a) (b)

Fig. 5-2: (a) Effective mobility dependence on RIE time. (Film configuration is F-doped single layer.) (b) SEM cross section image of the sample with d=900nm and RIE time = 30min.

5.3 Mobility in Low Carrier Concentration Region

5.3.1 Dependence of Mobility on carrier concentration

If film thickness is increased from 900nm to about 3000nm, we need to decrease carrier concentration from $1x10^{20}$ cm^{-3} to $2\text{-}3x10^{19}$ cm^{-3}, in order to keep free carrier absorption low. Fig. 5-3 shows the dependence of mobility on carrier concentration of FTO films fabricated on flat substrates at various conditions. The mobility of FTO films have the peaks at carrier concentration of about $1x10^{20}$ cm^{-3}. So, if carrier concentration is reduced by adjusting HF flow rate, mobility becomes low. As described in Chapter 4, grain barrier scattering is dominant at lower carrier concentration. It is not easy to reduce the grain barrier scattering drastically. Therefore high mobility with low carrier concentration could not be obtained at the same time, due to the grain barrier scattering.

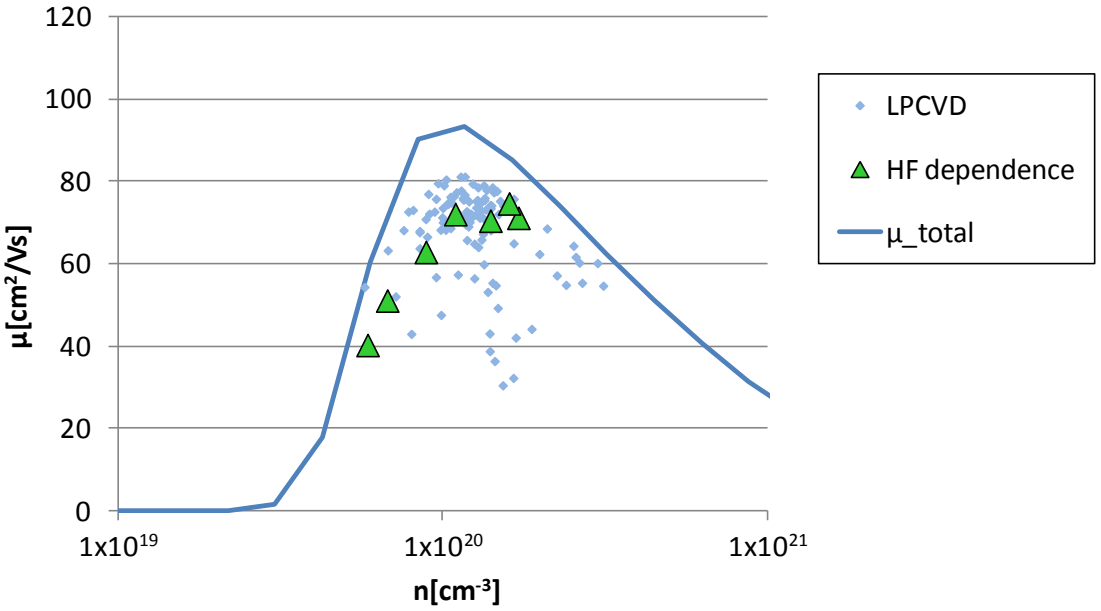

Fig. 5-3 Mobility dependence on carrier concentration of various samples. (HF dependence : Deposited with $HF/SnCl_4$=0~24. LPCVD : Deposited under various conditions, μ_total : Theoretical curve.) Details are shown in Chapter 4.

5.3.2 Non-doped / F-doped Stacked Structure

In order to achieve high mobility with low carrier concentration, we have adopted a stacked structure using thick non-doped layer and thin F-doped layer as shown in Fig. 5-4. With this approach, we can control the averaged carrier concentration, and the mobility in low carrier concentration is improved drastically as shown in Fig. 5-5.

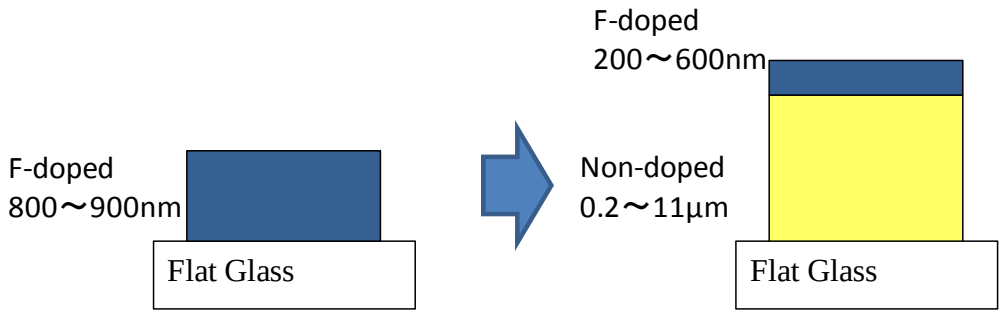

Fig. 5-4 Schematic of non-doped / F-doped stacked structure.

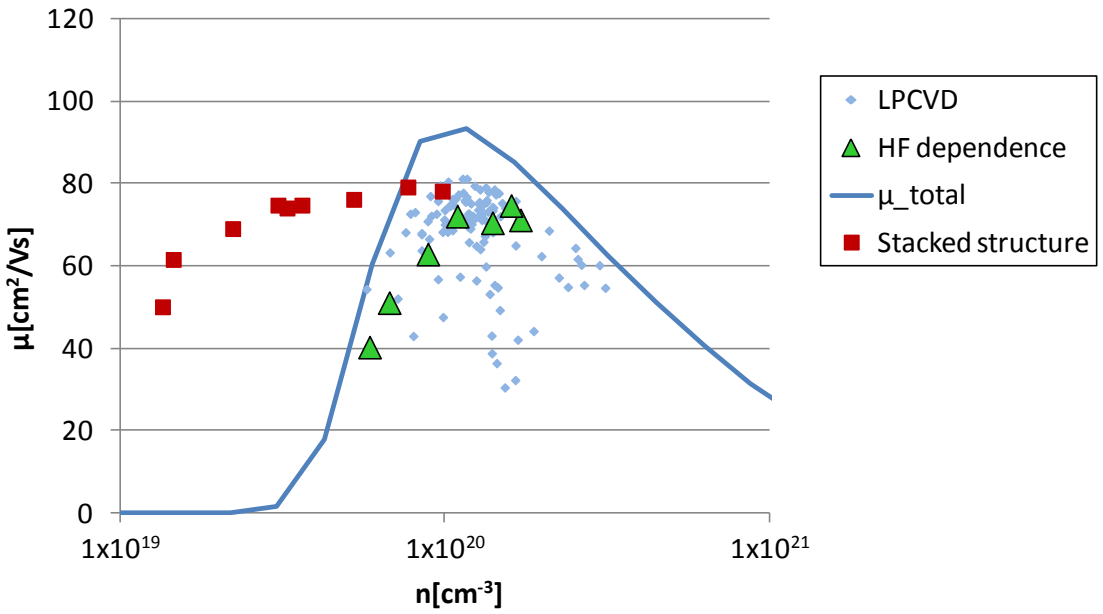

Fig. 5-5: Mobility dependence on carrier concentration of the non-doped / F-doped stacked structure shown in Fig. 5-4. Other data are same as Fig. 5-3.

5.4 Non-doped / F-doped Stacked Structure on RIE Etched Glass Substrates

We applied this stacked structure to RIE substrate. The condition of RIE process is fixed to 7 Pa 20 min. Fig. 5-6 shows the dependence of mobility and the

product of carrier concentration and film thickness $(n \times d)$ on film thickness. In the samples with stacked structure, F-doped and non-doped thickness is varied as $(n \times d)$ value is kept almost same around 7x10^{15} cm^{-2}. (F-doped thickness is 200 ~ 600 nm. Non-doped thickness is 1200 ~ 3000 nm.) The mobility of FTO film on RIE substrates is much lower than that on flat substrates if film thickness is thin. If thickness becomes thick up to 3000 nm, the mobility on RIE and flat substrates are almost the same. According to Fig. 5-6(b), $(n \times d)$ value is proportional to film thickness for the samples with F-doped single layer, but $(n \times d)$ is kept almost constant in stacked samples, whereas the mobility dependence of these two film structures are almost the same for both flat and RIE substrates.

Table 5-1 shows measured properties of various samples (Type-U, Sample A : F-doped layer only on flat glass, Sample B : Stacked structure on flat glass, Sample C : Stacked structure on RIE glass). SEM image, spectral absorption and haze ratio of these samples are shown in Fig. 5-7 and Fig. 5-8. Optical properties of these samples are shown in Fig. 5-8. As shown in Table 5-1, Sample A, B, and C has almost same $(n \times d)$, therefore, the absorption of these samples are equally low. (Note: The absorption of Sample C can't be measured accurately by IM method because of the reason described in Chapter 6. However, the absorption of Sample C should be same as Sample A and B, because $(n \times d)$ of these samples are almost same.) On the other hand, haze values of these samples are completely different. So, we can adjust haze ratio in this range. As the result, we have successfully achieved the high mobility (80 cm^2/Vs), low carrier concentration (2.2x10^{19} cm^{-3}) and high haze value (77% at wavelength of 1000 nm) at the same time.

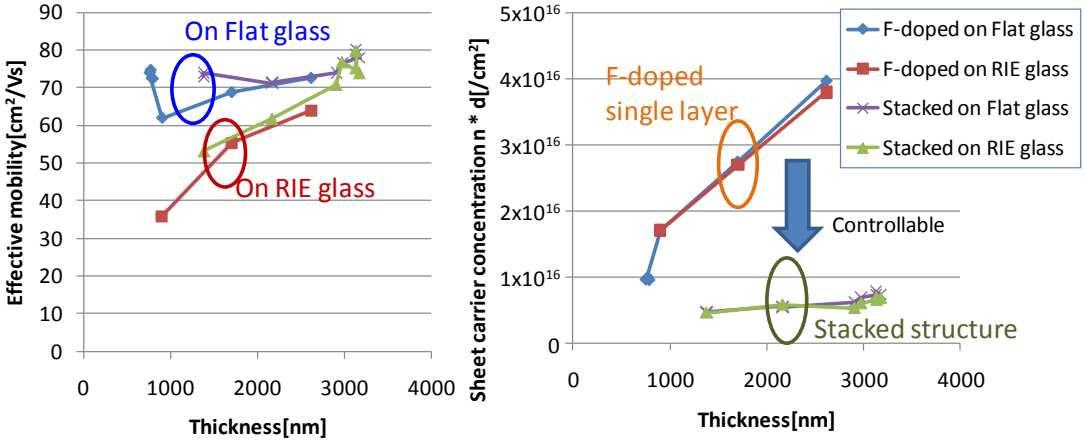

Fig. 5-6 : (a) Effective mobility dependence and (b) n * d dependence on film thickness. F-doped single layer on flat substrate (diamond), F-doped single layer on RIE substrate (square), stacked structure on flat substrate (cross), stacked structure on RIE substrate.

	Type-U	Sample A	Sample B	Sample C
Glass substrate	Flat	Flat	Flat	RIE
TCO	F-doped	F-doped	Stacked	Stacked
Thickness[nm]	867	867	2974	3129
Film absorption[%] (ave400～2000nm)	19.9	6.9	6.2	6.4 (Estimated)
Haze[%] (λ=1000nm)	1.9	0.6	7.9	76.5
Rs[Ω/□]	6.7	11.0	11.7	11.2
Mobility[cm^2/Vs]	58.8	72.4	76.6	79.8
Carrier concentration [cm^{-3}]	$1.8x10^{20}$	$9.0 x10^{19}$	$2.3x10^{19}$	$2.2x10^{19}$
n * d [cm^{-2}]	$1.6x10^{16}$	$7.8x10^{15}$	$7.0x10^{15}$	$7.0x10^{15}$

Table 5-1 The properties of various samples.

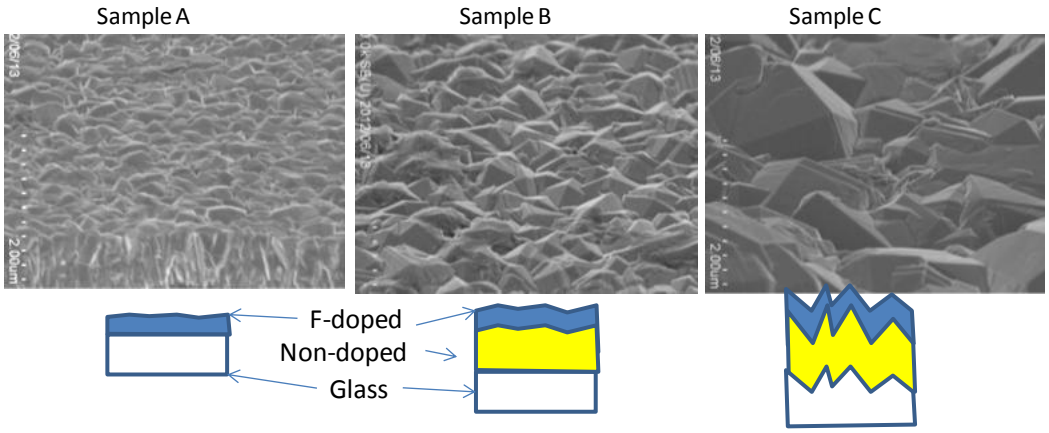

Fig. 5-7 : SEM image of surface morphology. Sample A : F-doped layer on flat substrate, Sample B : Stacked structure on flat substrate, Sample C : Stacked structure on RIE substrate.

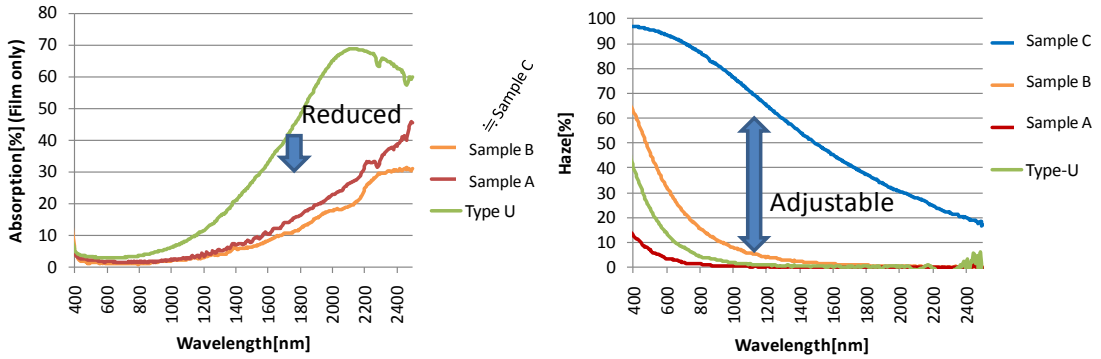

(a) (b)

Fig. 5-8 : (a) Spectral absorption. (b) Spectral haze.

5.5 Increasing Haze Ratio in Near-Infrared Region

As shown in section 5.4, we have succeeded to increase haze value. However, high haze is more important as wavelength become longer, because the absorption coefficient of thin-film silicon material is lower as wavelength becomes longer. As

described in Chapter 2, we set our target of haze ratio to 90% at wavelength 1000nm. Therefore, higher haze than sample C shown above is preferable. However, if RIE time is extended, the increment of haze value is very small as shown in Fig. 5-9.

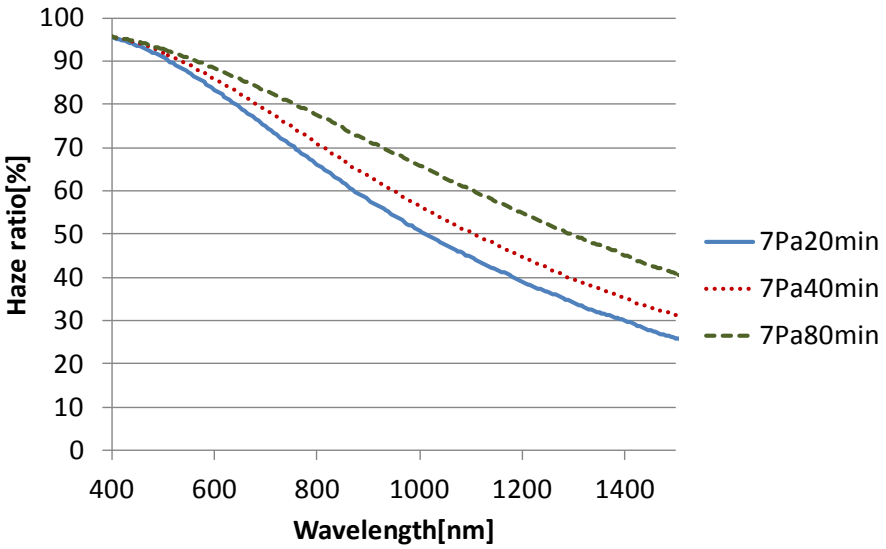

Fig. 5-9 Spectral haze of stacked structure on RIE glass. RIE time are 20, 40, and 80 min.

In this study, we have found that haze ratio can be increased drastically be increasing RIE pressure. Fig.5-10 shows SEM images of (a) RIE etched substrates in various conditions (top view), and (b) W-textured FTO (45 degree tilted view). As RIE pressure is increased, the feature size becomes larger and the depth of valley becomes deeper in both RIE etched substrates and FTO films on them, although the dependency on RIE time is not clear.

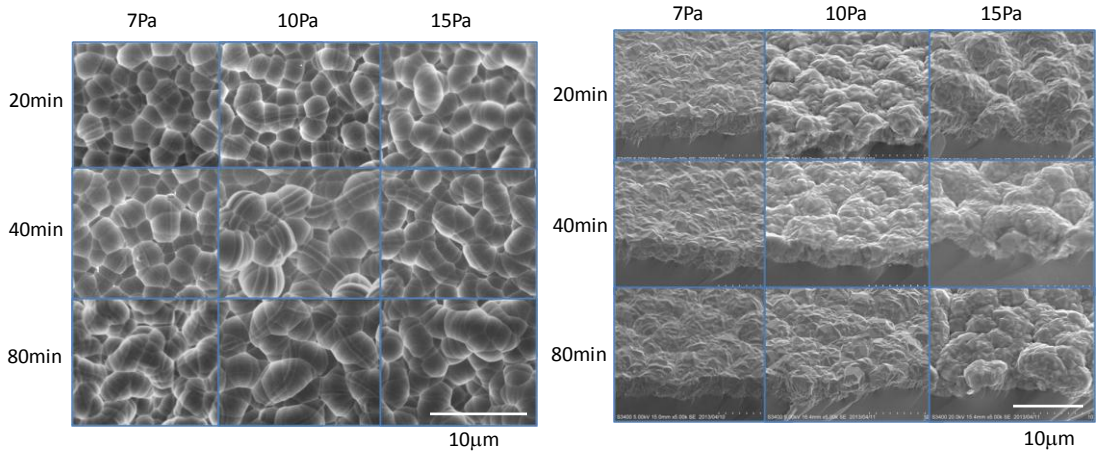

(a) (b)

Fig.5-10 SEM image of (a) RIE etched substrates (top view) and (b) W-textured FTO (45 degree tilted view).

Spectral haze and transmittance of stacked structure on RIE glass are shown in Fig. 5-11. By increasing RIE pressure from 7 Pa to 15 Pa, we have succeeded increasing haze ratio drastically, while transmittance of all samples are same and flat for all wavelength. The flat transmittance can be the result of high mobility as shown in Table 5-2. Fig. 5-12 shows the dependence of the mobility on RIE pressure. As RIE pressure is increased, mobility decreases slightly. This dependency can be understood from the SEM observation result that the feature size becomes larger and the depth of valley becomes deeper. On the other hand, mobility doesn't depend on the RIE process time. It is coincide with the SEM observation result.

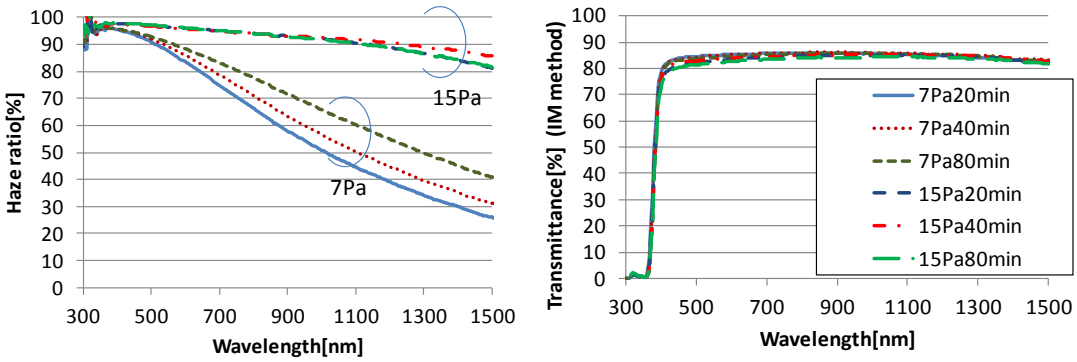

Fig. 5-11 Spectral haze of stacked structure on RIE glass. RIE time are 20, 40, and 80 min. RIE pressure is 7 and 15 Pa.

RIE condition		Mobility	Sheet R
Pressure[Pa]	Time[min]	[cm^2/Vs]	[Ω/□]
7	20	87.4	10.2
7	40	85.6	11.1
7	80	82.7	9.8
10	20	82.5	9.6
10	40	83.0	10.2
10	80	81.6	10.4
15	20	72.5	13.5
15	40	75.1	11.8
15	80	75.3	11.9
Ref : ZnO:B[8]		18.0	8.5

Table 5-2. Electrical properties of W-textured FTO. FTO thickness is around 3.6μm.

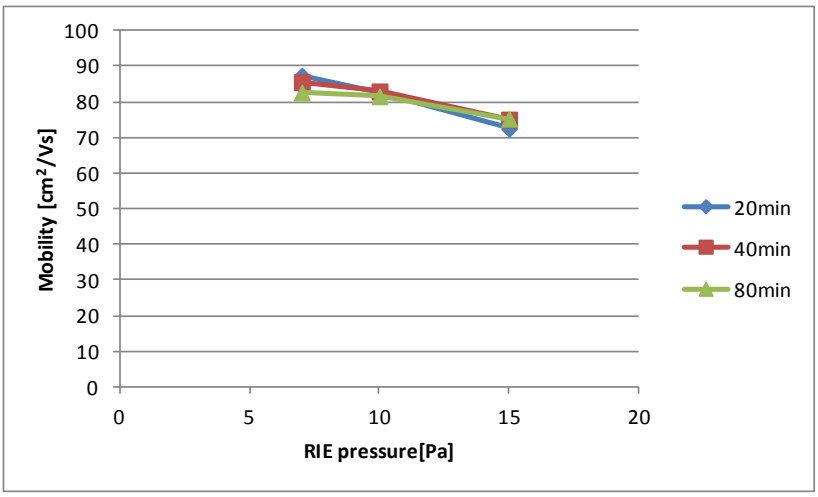

Fig. 5-12 The dependence of the mobility on RIE pressure. RIE process time is 20, 40, and 80 min.

5.6 Evaluation of W-textured TCO with Thin-Film Silicon Solar Cells

5.6.1 Evaluation with μc-Si:H solar cells

For comparing the capability of TCO substrates, cell evaluations were performed on W-textured FTO and ZnO:B with the same RIE condition (RIE pressure = 15 Pa, RIE process time = 40 min). Film thickness of FTO is around 3.6μm and that of ZnO:B is around 1.5μm. SEM images are shown in Fig. 5-13. The small textures generated by the crystalline FTO and ZnO:B are completely different. FTO has larger textures and ZnO:B has smaller. The large feature size generated by the shape of the RIE etched substrates are similar, however, FTO seems to have larger feature size than ZnO:B, because the film thickness of FTO is thicker than ZnO:B. Fig. 5-14 shows transmittance and spectral haze ratio of W-textured FTO and ZnO:B. FTO has higher

haze ratio than ZnO:B, especially in longer wavelength region. This can be attributed to the larger feature size of W-textured FTO. Transmittance of ZnO:B measured in IM method shows higher than that of FTO, but the absolute value itself may not be correct, because scattering at the interface between RIE etched glass and TCO can't suppress by IM method. (Detail will be explained in Chapter 6.) From Fig. 5-14(a), transmittance of ZnO:B drops in NIR region, but that of FTO is flat, because FTO has higher mobility around 80 cm^2/Vs. Note that transmittance of both samples drop at same wavelength in UV region, but it is the absorption of CH_2I_2 liquid used in IM method. In actual, SnO_2 has larger band gap than ZnO. Therefore, The absorption edge of FTO locates at higher energy than ZnO:B.

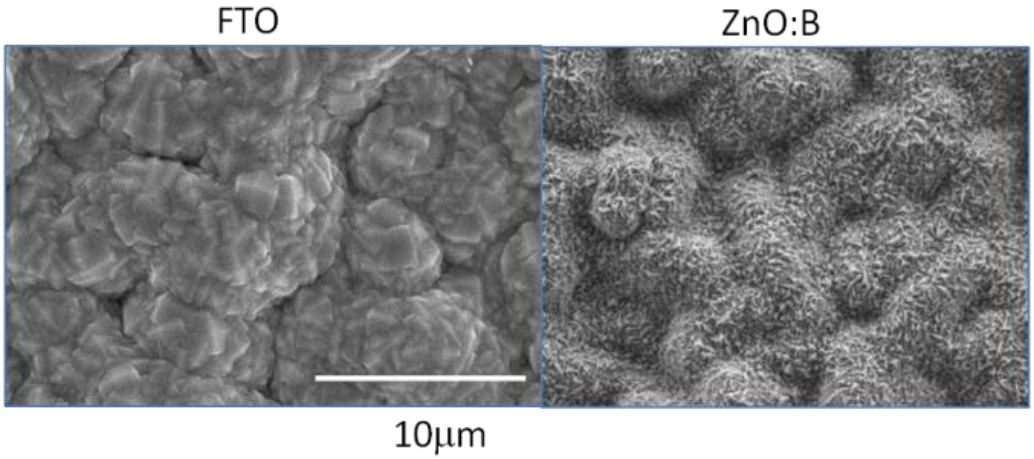

Fig. 5-13. SEM image of W-textured FTO and ZnO:B. (RIE condition: 15Pa , 40min).

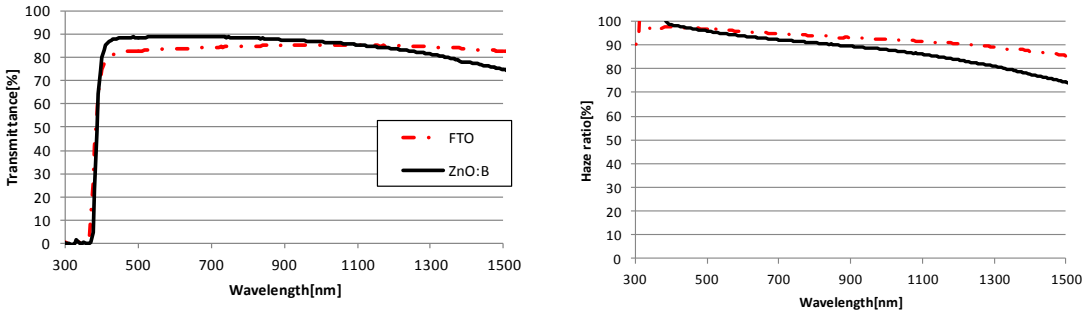

(a) (b)

Fig. 5-14 (a) Transmittance and (b) spectral haze ratio of W-textured FTO and ZnO:B.

The I–V characteristics and EQE of μc-Si:H solar cells are shown in Fig. 5-15. Higher conversion efficiency was observed in FTO than ZnO:B. Jsc of these two samples are almost same, but EQE is different. In the wavelength region less than 400 nm, FTO has higher EQE because SnO_2 has larger band gap than ZnO. In the wavelength region between 400 and 700 nm, ZnO:B has higher EQE. The difference of the transmittance shown in Fig. 5-14 may be able to explain the EQE. However, as explained previously, the absolute value of the transmittance measured in IM method may not be correct. In longer wavelength than 700nm, FTO has higher EQE. This can be explained by the drop of transmittance of ZnO:B in longer wavelength region and/or slightly lower haze ratio of ZnO:B than that of FTO.

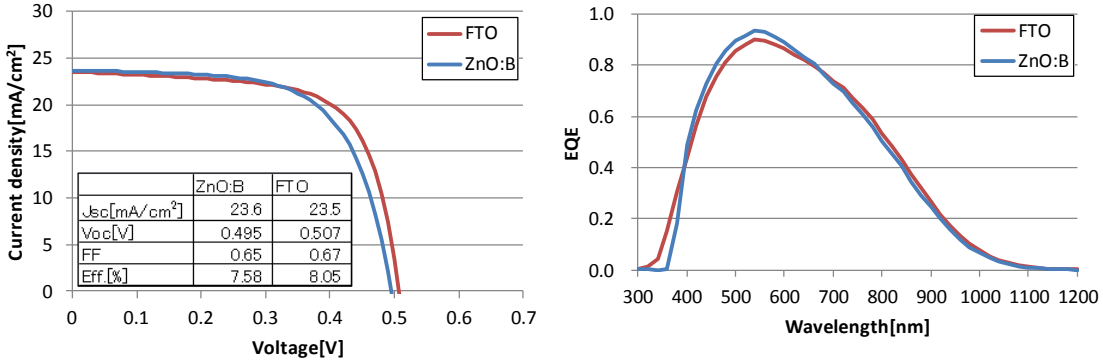

(a) (b)

Fig. 5-15 (a) I-V characteristics and (b) EQE of μc-Si:H solar cells with W-textured FTO and ZnO:B.

5.6.2 Evaluation with a-Si:H/μc-Si:H tandem solar cells

We also performed cell evaluation with a-Si:H/μc-Si:H tandem solar cells. In this experiment, the configuration of FTO sample are slightly changed from that in the subsection 5.6.1, while the configuration of ZnO:B sample is not changed. Before the deposition of the non-doped/F-doped stacked structure, TiO_2 (thickness 9nm) and SiO_2 (thickness 31nm) are deposited on RIE etched glass by sputtering in order to reduce the reflection at the interface between glass and non-doped SnO_2 layer. Fig. 5-16 shows the transmittance and spectral haze ratio of W-textured FTO and ZnO:B. Compared to Fig. 5-14, transmittance of FTO sample is higher. This difference is partially due to the TiO_2/SiO_2 layer placed between glass and SnO_2. However, the effect of reducing reflection at glass/SnO_2 interface is around 2%, and it can't explain the difference between Fig. 5-14 and Fig. 5-16. This may be attributed to the measurement error as described in Chapter 6. Regardless of the absolute value of transmittance, optical properties of FTO samples in and Fig. 5-16 are similar.

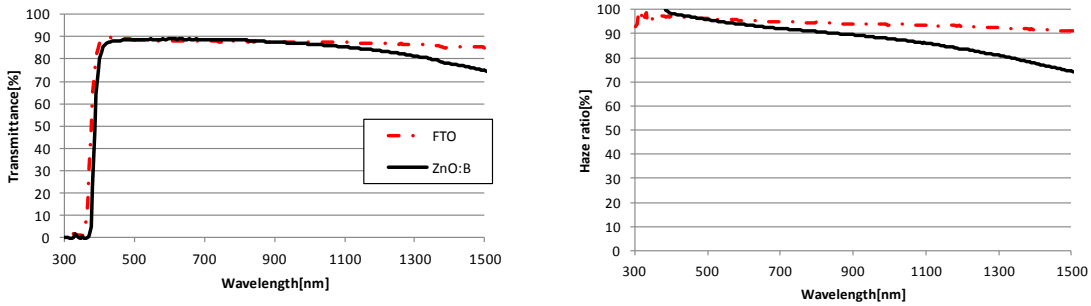

(a) (b)

Fig. 5-16 (a) Transmittance and (b) spectral haze ratio of W-textured FTO and ZnO:B.

I-V characteristics and EQE of a-Si:H/μc-Si:H tandem solar cells are shown in Fig. 5-17(a) and (b). Higher efficiency were obtained in FTO than in ZnO:B. External quantum efficiency of these two samples show clear difference. Similar to the subsection 5.6.1, this difference can be explained by the optical properties of W-textured FTO and ZnO:B. In the wavelength region less than 400 nm, FTO has higher EQE because SnO_2 has larger band gap than ZnO. In the wavelength region between 400 and 700 nm, both have similar EQE. In longer wavelength than 700nm, FTO shows higher EQE. This can be explained by the drop of transmittance of ZnO:B in longer wavelength region and lower haze ratio of ZnO:B than that of FTO.

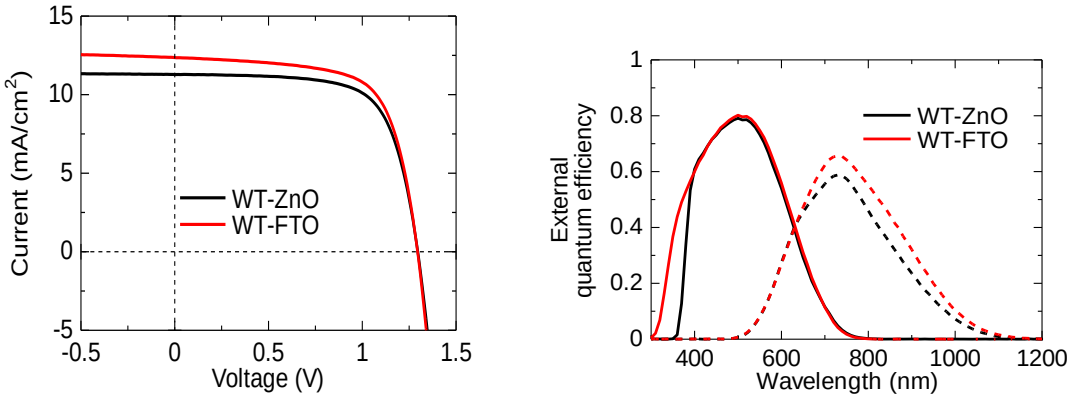

(a) (b)

Fig. 5-17 (a) I-V characteristics and (b) EQE of a-Si:H/μc-Si:H tandem solar cells with W-textured FTO and ZnO:B.

	WT-ZnO	WT-FTO
Jsc [mA/cm^2]	11.2822	12.3619
Voc [V]	1.2959	1.2947
Fill Factor	0.6946	0.679
Efficiency [%]	10.156	10.866
Series Resistance [Ω]	5.17x10	4.61x10
Shunt Resistance [Ω]	2.73x10^4	8.35x10^3
Sample Area [cm^2]	0.23	0.23
QE top [mA/cm^2]	11.212	11.693
QE bottom [mA/cm^2]	10.695	12.329
QE sum [mA/cm^2]	21.907	24.023

Table 5-3 The properties of a-Si:H/μc-Si:H tandem solar cells with W-textured FTO and

ZnO:B.

5.7 Conclusion

We have combined F-doped SnO_2 (FTO) with high mobility deposited by LPCVD and reactive ion etching (RIE) processed glass substrate. However, two problems have been found. (1) The mobility of FTO on RIE substrate dropped from that on flat glass (75 to 36 cm^2/Vs). To avoid this drop, thicker film is needed. (2) To keep high transmittance with thicker film, lower carrier concentration is needed. But the mobility dropped with lower carrier concentration. In order to solve these constrains, we have adopted a stacked structure using thick non-doped layer of 2700 nm and thin F-doped layer of 500 nm. With this novel approach, we have successfully achieved the high mobility (80 cm^2/Vs), low carrier concentration ($2.2x10^{19}$ cm^{-3}) and high haze value (77% at wavelength of 1000 nm) at the same time.

We also have found that we can control the morphology of RIE etched glass by changing RIE pressure resulting in an increase of haze ratio at the wavelength 1000 nm drastically from 57 % (7 Pa) to 92 % (15 Pa). By this approach, we can fabricate FTO substrates with high mobility (around $80cm^2/Vs$) and very high haze (90% at 1000nm) as the target shown in Chapter 2.

For evaluation purpose μc-Si:H single cells with 1 μm-thick i-layer have been fabricated on these newly developed FTO substrate using RIE conditions of 15Pa, 40min. The efficiency of 8.05% was obtained, where 7.58% was obtained in case of W-textured ZnO:B. And we also fabricated a-Si:H/μc-Si:H tandem solar cells. The efficiency of 10.87% was obtained, where 10.16% was obtained in case of W-textured

ZnO:B. These results show that this newly developed W-textured FTO is a promising candidate for high efficiency thin film Si solar cells.

References

[1] M. Isshiki, Y. Ishikawa, T. Ikeda, T. Oyama, and H. Odaka, "SnO_2 : F with Very High Haze Value and Transmittance in Near Infrared Wavelength for Use as Front Transparent Conductive Oxide Films in Thin- Film Silicon Solar Cells," *MRS Proc.*, vol. 1536, 2014.

[2] M. Isshiki, P. Sichanugrist, Y. Abe, and M. Konagai, "SnO_2 : F Substrates with Larger Feature Size and Its Application to Thin-Film Silicon Solar Cells," in *23rd International Photovoltaic Science and Engineering Conference (PVSEC-23)*, 2013, p. 2–O–9.

[3] P. Drude, "Zur Elektronentheorie der Metalle," *Ann. Phys.*, vol. 306, no. 3, pp. 566–613, 1900.

[4] P. Drude, "Zur Elektronentheorie der Metalle; II. Teil. Galvanomagnetische und thermomagnetische Effecte," *Ann. Phys.*, vol. 308, no. 11, pp. 369–402, 1900.

[5] M. Isshiki, T. Ikeda, J. Okubo, T. Oyama, and E. Shidoji, "Improving Mobility of F-Doped SnO_2 Thin Films by Introducing Temperature Gradient during Low-Pressure Chemical Vapor Deposition," *Jpn. J. Appl. Phys.*, vol. 51, p. 095801, 2012.

[6] S. Nakao, N. Yamada, T. Hitosugi, Y. Hirose, T. Shimada, and T. Hasegawa, "High Mobility Exceeding 80 $cm^2V^{-1}s^{-1}$ in Polycrystalline Ta-Doped SnO_2 Thin

Films on Glass Using Anatase TiO_2 Seed Layers," *Appl. Phys. Express*, vol. 3, no. 3, p. 031102, Feb. 2010.

[7] S. Nakao, N. Yamada, T. Hitosugi, Y. Hirose, T. Shimada, and T. Hasegawa, "Fabrication of transparent conductive W-doped SnO_2 thin films on glass substrates using anatase TiO_2 seed layers," *Phys. Status Solidi*, vol. 8, no. 2, pp. 543–545, Feb. 2011.

[8] A. Hongsingthong, T. Krajangsang, I. A. Yunaz, S. Miyajima, and M. Konagai, "ZnO Films with Very High Haze Value for Use as Front Transparent Conductive Oxide Films in Thin-Film Silicon Solar Cells," *Appl. Phys. Express*, vol. 3, no. 5, p. 051102, May 2010.

[9] M. Mizuhashi, Y. Gotoh, K. Adachi, and Y. Gotoh, "Texture Morphology of SnO_2:F films and cell reflectance," *Jpn. J. Appl. Phys.*, vol. 27, no. 11, pp. 2053–2061, 1988.

Chapter 6[1]

6 New method to measure whole-wavelength transmittance of TCO substrates for thin-film silicon solar cells

6.1 Introduction

Among thin-film silicon solar cells (TFSSC), the highest initial efficiency of 16.3% was reported in a-Si:H/a-SiGe:H/μc-Si:H triple structure, and highest stabilized efficiency of 13.4% was reported in a-Si:H/μc-Si:H/μc-Si:H triple structure[2]. On the other hand, a theoretical analysis reported that an efficiency of over 20% can be achieved[3]. There is a large gap between theoretical and experimental efficiency so that there should be large room for improving efficiency.

In case of superstrate type TFSSC, transparency and light trapping are very important functions of TCO substrates for achieving high cell efficiency. In order to improve light trapping, many researchers have studied to increase haze ratio by adjusting deposition conditions of atmosphere pressure chemical vapor deposition (APCVD)[4], [5], applying reactive ion etched glass substrates[6]–[9] (so-called "W-textured TCO"), applying photolithography etched substrates[10], and applying nanoimprint plastic mold[11]–[16]. To measure the transmittance and reflectance of TCO substrates with high haze, an immersion (IM) method is widely used[17]–[19]. The IM method has been introduced to reduce the measurement error due to the

scattering at TCO surface by reducing the scattering with attaching CH_2I_2 liquids (whose refractive index 1.74 is close to that of TCO materials) onto TCO surface.

Fig. 6-1 show the schematic of 2 methods used for transmittance measurement. (a) is the conventional method and (b) is the improved IM method. The substrate configuration for W-textured TCO is also shown in (c). However, three problems in measuring transmittance with IM method have been found. (1) CH_2I_2 liquids themselves absorb light in short wavelength region less than 400nm. (2) The transmittance around the absorption edge of CH_2I_2 liquids is very sensitive for the amount of the liquid. The above two problems are important especially for solar cells with wide band gap materials such as a-SiO:H[20]–[22] and a-SiC:H[23]–[26]. which are necessary for the top cells for multi stacked solar cells as innovative thin-film solar cells[27]. (3) Scattering cannot be suppressed when the scattering surfaces are more than 2 surfaces (for example, TCO on RIE etched glass substrate as shown in Fig. 6-1(c)). In this chapter, we proposed a new method to measure the transmittance which can avoid the problems described above.

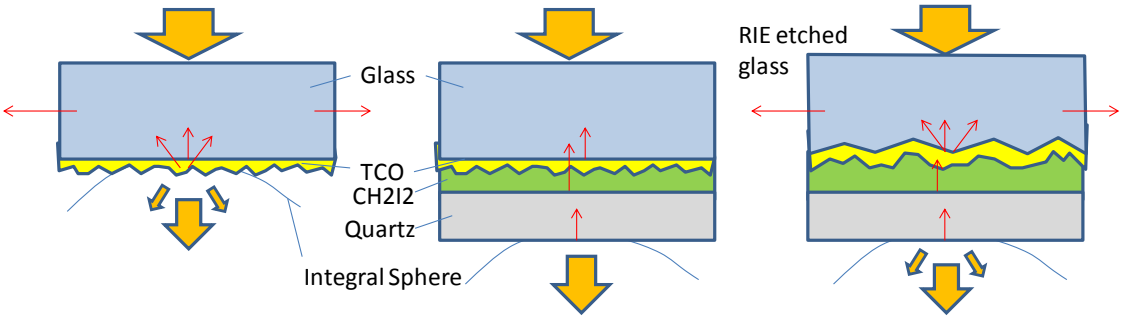

Fig. 6-1. Schematics of methods to measure the transmittance. (a) Conventional, (b) IM method, (c) IM method applied to W-textured TCO.

6.2 Experimental methods

6.2.1 TCO substrates and optical evaluations

We prepared two kinds of TCO substrates. One is SnO_2:F (FTO) films on flat glass substrates. The other is FTO or ZnO:B (BZO) on RIE etched glass substrates. We called them as "W-textured" TCO. In all experiments, 0.7-mm-thick alkaline-free glass substrates (Asahi glass AN100 or Corning 7059) or 1.0-mm-thick soda lime glass substrates (Schott B270) were used. In case of FTO on flat glass, anti-reflection (AR) layers are fabricated with Ta_2O_5 and SiO_2 and they are inserted into air / glass interface and glass / TCO interface. Sample configurations are listed in Table 6-1. In case of RIE etched glass, sample configurations are listed in Table 6-2. The details of their deposition process are described elsewhere[7].

Sample#	Glass	Anti reflection layer location	Film thickness [μm]	Sheet resistance [Ω/□]
woAR1	AN100	None	0.8	6.8
woAR2	AN100	None	1.6	3.6
withAR1	AN100	Air/glass, glass/TCO	1.6	4.7
withAR2	B270	Air/glass, glass/TCO	1.6	3.7

Table 6-1: Sample configurations of FTO films on flat glass.

Sample#	TCO	Film thickness [μm]
FTO-1, FTO-2,FTO-3	FTO	3.6
BZO	BZO	1.5

Table 6-2 : Sample configurations of TCO films on RIE etched glass (Corning 7059). RIE condition is 15 Pa 40 min. Sheet resistance is around 10 Ω/□.

Optical properties were measured using PerkinElmer Lambda950. Here we propose the new method to measure the transmittance more accuracy as shown in Fig. 6-2.

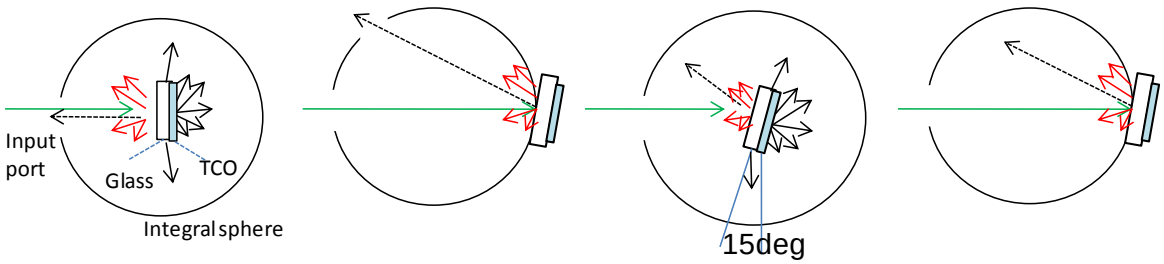

(a) (b) (c) (d)

Fig. 6-2. Measurement Configurations. (a) Sample is placed inside the integral sphere and perpendicular to the incident light. The measured value is defined as $T_{integral}$(0deg). (b) Reflectance in Specular Component Excluded (SCE) mode (R_{SCE}). (c) Sample is placed inside the integral sphere and tilted 15degree to the incident light. The measured value is defined as $T_{integral}$(15deg). (d) Reflectance in Specular Component Included (SCI) mode (R_{SCI}).

6.2.2 μc-Si:H cell fabrication

Regarding to the W-textured TCO samples, we evaluated cell performance with μc-Si:H solar cells. In case of FTO samples, thin ZnO:Al was deposited by sputtering on FTO before cell fabrication in order to avoid SnO_2 reduction by atomic hydrogen[28]. μc-Si:H solar cells with an area of 0.086 cm^2 were fabricated with the layer sequence: TCO / p-μc-SiO:H / i- μc-Si:H / n- μc-SiO:H / Ag / Al by a conventional plasma enhanced chemical vapor deposition (PECVD) system using SiH_4, H_2, B_2H_6, PH_3 and CO_2 as source gases, at the substrate temperature of about 200 °C. The i-layer thickness was about 1μm. Ag and Al layers were deposited by evaporation method. The current-voltage (I-V) characteristics of fabricated solar cells were measured under 1-sun (AM 1.5, 100mW/cm^2) illumination. The external quantum efficiency (EQE) measurement was performed to estimate the spectral response of these solar cells. While the measurements of I-V and EQE, shadow mask with 0.078 cm^2 hole was adopted to eliminate the effect of scattered light from the surrounding area.

6.3 Results and discussion

6.3.1 Effective transmittance of FTO on flat glass

Fig. 6-3 shows the transmittance and absorption of FTO samples in Table 6-1 measured with TCO substrate alone. $A(\text{TCO only}) = 100 - \big(T(\text{TCO only}) + R(\text{TCO only})\big)$ where $A(\text{TCO only})$, $T(\text{TCO only})$, and $R(\text{TCO only})$ refer to the absorption, transmittance, and reflectance measured with TCO alone as shown in Fig. 6-1(a). Fig. 6-4 shows the transmittance and absorption of FTO samples in Table 6-1 measured by IM method. $A(\text{IM}) = 100 - \big(T(\text{IM}) + R(\text{IM})\big)$ where $A(\text{IM})$, $T(\text{IM})$,

and R(IM) refer to the absorption, transmittance, and reflectance measured by IM method as shown in Fig. 6-1(b). Comparing between A(TCO only) and A(IM), A(TCO only) is higher than A(IM). This is due to the measurement error of A(TCO only) mentioned in the introduction. Because the certain amount of light reflected and scattered at textured TCO / air interface has been escaped from the glass edge by total internal reflection at TCO / air interface and glass / air interface, low transmittance was measured. Comparing between the inset of Fig. 6-3 and Fig. 6-4, the transmittances in short wavelength region less than 400nm are completely different. T(IM) was much lower than T(TCO only) due to the absorption of CH_2I_2 liquid used in IM method. Therefore, IM method has a disadvantage of measuring absorption at the short wavelength region accurately due to the absorption of CH_2I_2 liquid.

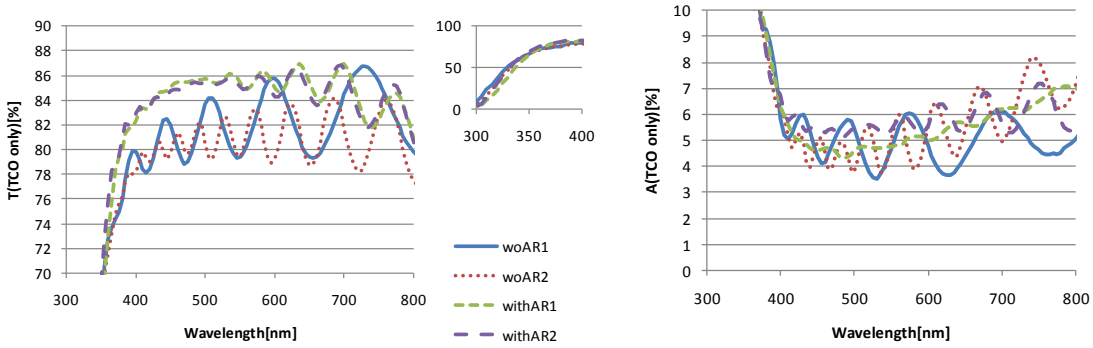

(a) (b)

Fig. 6-3. (a) Transmittance T(TCO only) and (b) Absorption A(TCO only) of FTO on flat glass measured with TCO substrate alone. The inset of (a) shows T(TCO only) in 300~400nm wavelength.

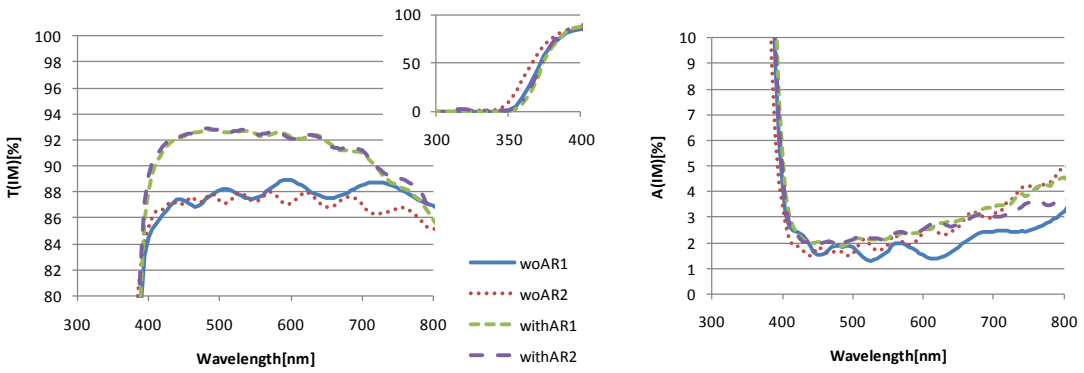

(a) (b)

Fig. 6-4. (a) Transmittance T(IM) and (b) Absorption A(IM) of FTO on flat glass measured in IM method. The inset of (a) shows T(IM) in 300~400nm wavelength.

To overcome these problems, we adopted a new setup to measure the transmittance by using a center mount accessory (PerkinElmer PELA9039) to hold TCO samples inside the integral sphere as shown in Fig. 6-2. In (a), the sample is placed inside the integral sphere and perpendicular to the incident light, so that only specular reflected light exits from the integral sphere. The measured value is defined as $T_{integral}(0deg)$. In (b), the reflectance in specular component excluded (SCE) mode (defined as R_{SCE}) is measured. In (c), the sample is placed inside the integral sphere and tilted 15degree to the incident light, so that all transmitted and reflected light are captured by the integral sphere. The measured value is defined as $T_{integral}(15deg)$. In (d), the reflectance in specular component included (SCI) mode (defined as R_{SCI}) is measured. Considering that all light are captured in the configuration (c), $100 - T_{integral}(15deg)$ should be similar to the absorption. Similarly, $100 - (T_{integral(0deg)} + R_{SCI} - R_{SCE})$ should be similar to the absorption too, because $R_{SCI} - R_{SCE}$ is specular reflection.

Fig. 6-5 shows the absorption of FTO fabricated on flat glass measured under

different configuration. It was confirmed that A(IM) (Fig. 6-4 (b)), $100 - T_{integral}(15deg)$ (shown in Fig. 6-5(a)), and $100 - (T_{integral(0deg)} + R_{SCI} - R_{SCE})$ (shown in Fig. 6-5(b)) are almost the same, although A(TCO only) (Fig. 6-3(b)) has higher value by 2~3 % in visible light region. Note that $100 - T_{integral}(15deg)$ and $100 - (T_{integral(0deg)} + R_{SCI} - R_{SCE})$ have slightly larger values compared to A(IM). This may come from the fact that in case of Fig. 6-2 some light was absorbed by TCO several times before it escapes from the glass edge while traveling through TCO layer. However, we can confirmed that this loss is much smaller than the light escaped from glass edge by comparing Fig. 6-3(b), Fig. 6-4(b), and Fig. 6-5. And in short wavelength region less than 400nm, A(IM) should not be correct value due to the absorption of CH_2I_2 liquid, whereas $100 - T_{integral}(15deg)$ and $100 - (T_{integral(0deg)} + R_{SCI} - R_{SCE})$ should be correct.

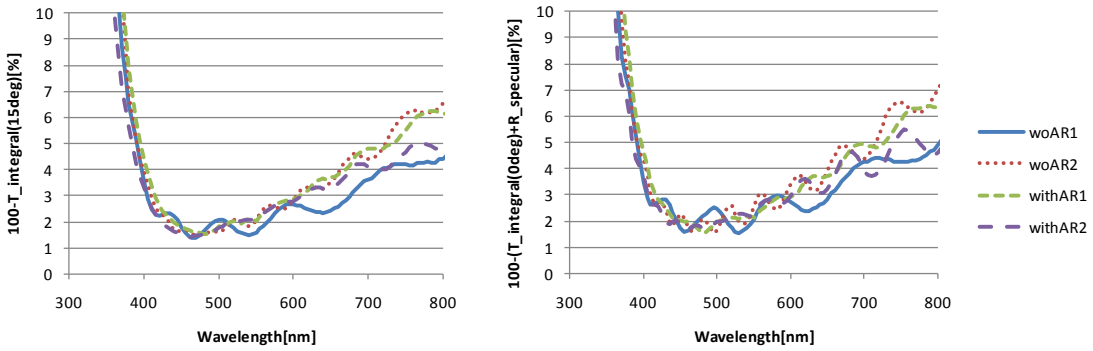

(a) (b)

Fig. 6-5. Absorption of FTO on flat glass measured in different configurations. (a) $100–T_{integral}(15deg)$ and (b) $100-(T_{integral}(0deg)+R_{SCI}-R_{SCE})$

As described above, we confirmed that the absorption could be measured correctly with $100 - T_{integral}(15deg)$ and $100 - (T_{integral(0deg)} + R_{SCI} - R_{SCE})$. This new method can be applied to measure the transmittance including the light

escaped from the glass edge. $T_{integral}(0deg)$ includes the transmitted light, the light escaped from the edge, and R_{SCE}. The sum of the transmitted light and the light escaped from the edge should be a good measure for the amount of light arriving at the thin-film silicon layer in the actual cell. Therefore, we call $T_{integral}(0deg) - R_{SCE}$ as an "effective transmittance". Similarly, $T_{integral}(15deg) - R_{SCI}$ should be the same as the effective transmittance. Fig. 6-6 shows the effective transmittance of FTO fabricated on flat glass, $T_{integral}(0deg) - R_{SCE}$ and $T_{integral}(15deg) - R_{SCI}$. It was confirmed that both are equal to each other. Note that the effective transmittance is not equal to the amount of light arriving at the thin-film silicon layer, because the reflection at TCO surface is different between the measurement condition and the cell condition. However, we should be able to compare the effective transmittance relatively among various TCO substrates.

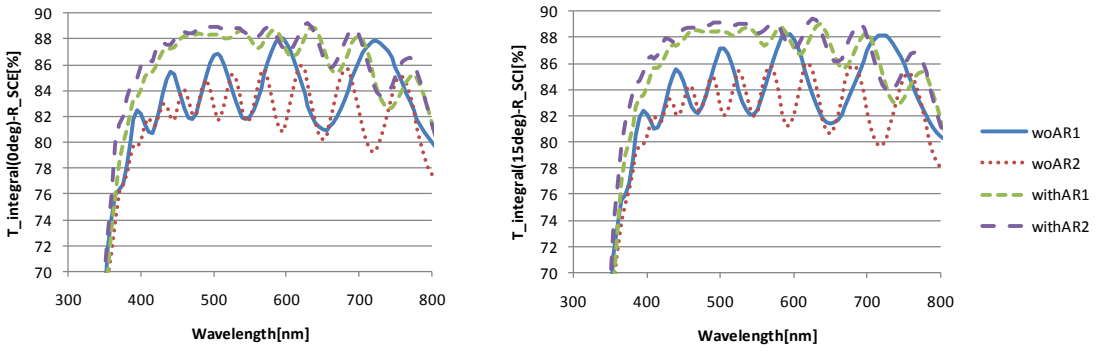

(a) (b)

Fig. 6-6. Effective transmittance of FTO on flat glass. (a) $T_{integral}(0deg)$-R_{SCE}. (b) $T_{integral}(15deg)$-R_{SCI}.

6.3.2 Effective transmittance of TCO on RIE etched glass substrates

As described above, transmittance measured in IM method and the effective transmittance should be a good measure for the amount of light arriving at the thin-film

silicon layer in the actual cell. However, IM method can't reduce the measurement error enough in case that TCO is deposited on substrates having the structures like RIE etched glass substrates (so-called "W-textured TCO"), photolithography etched substrates, and nanoimprint plastic mold, because the scattering at TCO / substrates can't be suppressed even if CH_2I_2 is attached on TCO surface as shown in Fig. 6-1(c). Fig. 6-7(a) shows the haze ratio measured in IM method configuration as shown in Fig. 6-1(c), and (b) shows the conventional haze ratio measured with only TCO as shown in Fig. 6-1(a). All samples have very high haze ratio for the conventional method and even in IM method configuration, all samples still have high haze ratio. Therefore, we can expect that some lights still escape from the glass edge as described above even if the IM method has been used.

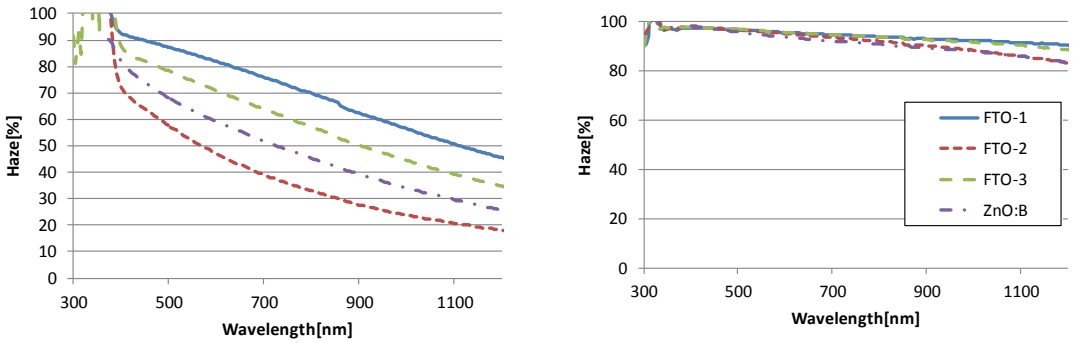

(a) (b)

Fig. 6-7. (a) Haze ratio (measured by IM method). (b) Haze ratio (measured with only TCO)

As shown in Fig. 6-8, we compared the transmittances of W-textured TCO substrates shown in Table 6-2 which were measured by IM method (T(IM)) and by this proposed method ($T_{integral}(0deg) - R_{SCE}$) or effective transmittance. It should be noted that $T_{integral}(15deg) - R_{SCI}$ (not shown) is almost the same as $T_{integral}(0deg) -$

R_{SCE}. It is clear that the magnitude sequence of T(IM) for various substrates is different from the one measured by this proposed method.

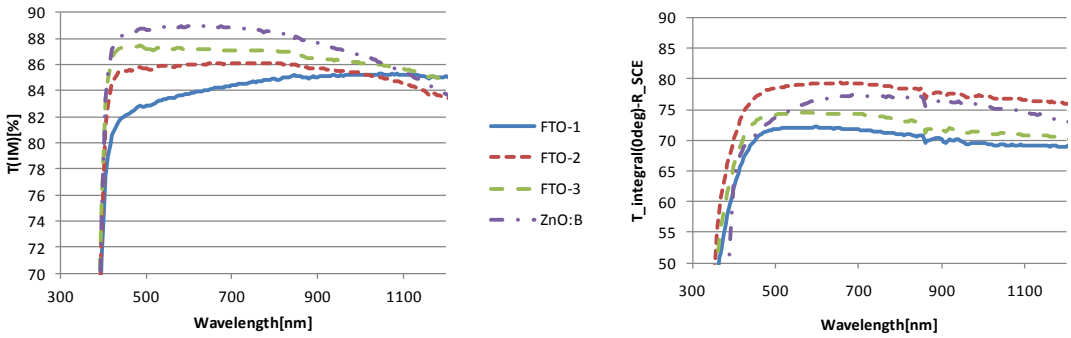

(a) (b)

Fig. 6-8. (a) Transmittance in IM method (T(IM)) and (b) the effective transmittance ($T_{integral}$(0deg)-R_{SCE}) of W-textured FTO and BZO.

6.3.3 Comparison between the effective transmittance and the external quantum efficiency of μc-Si:H cells

To see the relation between the EQE and the effective transmittance, the μc-Si cells were fabricated on the W-textured TCO shown in Table 6-2. Their I–V characteristics and EQE were shown in Fig. 6-9 while their measured parameters were also shown in Table 6-3. Voc, FF, and Jsc varied among the samples, but EQE should be rigidly connected with the transmittance of TCO substrates. Comparing between the EQE and the effective transmittance, it is found that the magnitude sequence of the effective transmittance is similar to that of the EQE. (FTO-2 > BZO > FTO-3 > FTO-1 in order of the effective transmittance at around wavelength 500 ~ 600 nm. FTO-2 ~ BZO > FTO-3 ~ FTO-1 in order of EQE at around wavelength 500 ~ 600 nm.) However, the order of T(IM) is obviously different from that of the EQE. (BZO > FTO-3 >

FTO-2 > FTO-1 in order of T(IM).) Therefore, this new method could be a useful tool to evaluate TCO substrates for thin-film silicon solar cells.

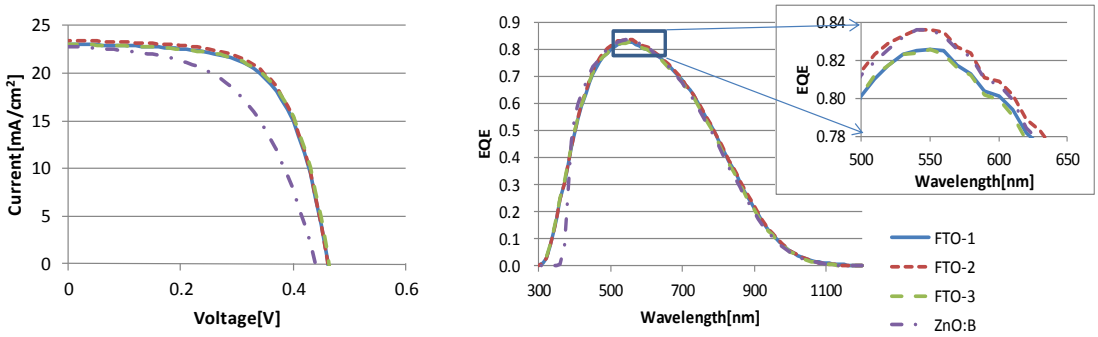

(a) (b)

Fig. 6-9. (a) I-V characteristics and (b) external quantum efficiency (EQE).

	FTO-1	FTO-2	FTO-3	BZO
Jsc[mA/cm^2]	23.06	23.43	23.04	22.80
Voc[V]	0.462	0.461	0.463	0.440
Fill Factor	0.642	0.646	0.647	0.539
Efficiency[%]	6.83	6.98	6.90	5.41

Table 6-3. Parameters of μc-Si:H cells on W-textured FTO and BZO.

6.4 Conclusions

In IM method widely used for evaluation of TCO substrates, three problems had been found in order to measure their transmittances accurately. (1) CH_2I_2 liquid itself absorbs the light in short wavelength region. (2) The transmittance around the

absorption edge of CH_2I_2 liquids is very sensitive to its amount. (3) Scattering cannot be suppressed when the scattering surfaces are more than 2 surfaces (for example, TCO on RIE etched glass substrate). To overcome these problems, we proposed new setup to measure the optical properties of TCO substrates by holding the samples inside the integral sphere. It has been confirmed that the absorption in all wavelength could be measured accurately. As the results, we have confirmed that their absorption in all wavelength could be measured accurately and the transmittance measured by the new method was well consistent with the external quantum efficiency (EQE) of the fabricated cell while the transmittance measured with conventional IM method showed differently. Therefore, this new method could be a useful tool to evaluate TCO substrates for thin-film silicon solar cells.

References

[1] M. Isshiki, P. Sichanugrist, Y. Abe, and T. Oyama, "New method to measure whole-wavelength transmittance of TCO substrates for thin-film silicon solar cells," *Cuurent Appl. Phys.*

[2] S. Kim, J.-W. Chung, H. H.-M. Lee, J. Park, and Y. Heo, "Remarkable progress in thin-film silicon solar cells using high-efficiency triple-junction technology," *Sol. Energy Mater. Sol. Cells*, vol. 119, pp. 26–35, Dec. 2013.

[3] I. A. Yunaz, A. Yamada, and M. Konagai, "Theoretical Analysis of Amorphous Silicon Alloy Based Triple Junction Solar Cells," *Jpn. J. Appl. Phys.*, vol. 46, no. No. 47, pp. L1152–L1154, Nov. 2007.

[4] T. Oyama, M. Kambe, N. Taneda, and K. Masumo, "Requirements for TCO Substrate in Si-based Thin Film Solar Cells -Toward Tandem," *MRS Proc.*, vol. 1101, 2008.

[5] M. Kambe, T. Matsui, H. Sai, N. Taneda, K. Masumo, A. Takahashi, T. Ikeda, T. Oyama, M. Kondo, and K. Sato, "Improved light-trapping effect in a-Si:H / μC-Si:H tandem solar cells by using high haze SnO_2:F thin films," in *2009 34th IEEE Photovoltaic Specialists Conference (PVSC)*, 2009, pp. 001663–001666.

[6] A. Hongsingthong, T. Krajangsang, I. A. Yunaz, S. Miyajima, and M. Konagai, "ZnO Films with Very High Haze Value for Use as Front Transparent

Conductive Oxide Films in Thin-Film Silicon Solar Cells," *Appl. Phys. Express*, vol. 3, no. 5, p. 051102, May 2010.

[7] M. Isshiki, Y. Ishikawa, T. Ikeda, T. Oyama, and H. Odaka, "SnO_2:F with Very High Haze Value and Transmittance in Near Infrared Wavelength for Use as Front Transparent Conductive Oxide Films in Thin- Film Silicon Solar Cells," *MRS Proc.*, vol. 1536, 2014.

[8] M. Isshiki, P. Sichanugrist, Y. Abe, and M. Konagai, "SnO_2:F Substrates with Larger Feature Size and Its Application to Thin-Film Silicon Solar Cells," in *23rd International Photovoltaic Science and Engineering Conference (PVSEC-23)*, 2013, p. 2–O–9.

[9] A. Hongsingthong, T. Krajangsang, A. Limmanee, K. Sriprapha, J. Sritharathikhun, and M. Konagai, "Development of textured ZnO-coated low-cost glass substrate with very high haze ratio for silicon-based thin film solar cells," *Thin Solid Films*, vol. 537, pp. 291–295, Jun. 2013.

[10] H. Stiebig, N. Senoussaoui, C. Zahren, C. Haase, and J. Müller, "Silicon thin-film solar cells with rectangular-shaped grating couplers," *Prog. Photovoltaics Res. Appl.*, vol. 14, no. 1, pp. 13–24, Jan. 2006.

[11] J. Escarré, K. Söderström, C. Battaglia, F.-J. Haug, and C. Ballif, "High fidelity transfer of nanometric random textures by UV embossing for thin film solar cells applications," *Sol. Energy Mater. Sol. Cells*, vol. 95, no. 3, pp. 881–886, Mar. 2011.

[12] M. Despeisse, M. Boccard, C. Battaglia, J. Escarre, G. Bugnon, S. Hänni, K. Söderström, B. Perruche, L. Ding, S. Nicolay, F. Meillaud, and C. Ballif, "ADVANCED SUPERSTRATES FOR HIGH EFFICIENCY THIN FILM SILICON SOLAR CELLS," in *The 21st International Photovoltaic Science and Engineering Conference*, 2011.

[13] C. Battaglia, J. Escarré, K. Söderström, L. Erni, L. Ding, G. Bugnon, A. Billet, M. Boccard, L. Barraud, S. De Wolf, F.-J. Haug, M. Despeisse, and C. Ballif, "Nanoimprint lithography for high-efficiency thin-film silicon solar cells.," *Nano Lett.*, vol. 11, no. 2, pp. 661–5, Feb. 2011.

[14] A. Bessonov, Y. Cho, S.-J. Jung, E.-A. Park, E.-S. Hwang, J.-W. Lee, M. Shin, and S. Lee, "Nanoimprint patterning for tunable light trapping in large-area silicon solar cells," *Sol. Energy Mater. Sol. Cells*, vol. 95, no. 10, pp. 2886–2892, Oct. 2011.

[15] M. a. González Lazo, R. Teuscher, Y. Leterrier, J.-A. E. Månson, C. Calderone, A. Hessler-Wyser, P. Couty, Y. Ziegler, and D. Fischer, "UV-nanoimprint lithography and large area roll-to-roll texturization with hyperbranched polymer nanocomposites for light-trapping applications," *Sol. Energy Mater. Sol. Cells*, vol. 103, pp. 147–156, Aug. 2012.

[16] A. Feltrin, T. Meguro, E. Van Assche, T. Suezaki, M. Ichikawa, T. Kuchiyama, D. Adachi, O. Inaki, K. Yoshikawa, G. Koizumi, H. Uzu, H. Ueda, T. Uto, T. Fujimoto, T. Irie, H. Hayakawa, N. Nakanishi, M. Yoshimi, and K. Yamamoto,

"Advanced light trapping designs for high efficiency thin film silicon solar cells," *Sol. Energy Mater. Sol. Cells*, vol. 119, pp. 219–227, Dec. 2013.

[17] M. Mizuhashi, Y. Gotoh, K. Adachi, and Y. Gotoh, "Texture Morphology of SnO_2:F films and cell reflectance," *Jpn. J. Appl. Phys.*, vol. 27, no. 11, pp. 2053–2061, 1988.

[18] M. Kambe, N. Taneda, A. Takahashi, and T. Oyama, "Coated Glass Substrates for Silicon Based Thin Film Solar Cells," *Res. Reports Asahi Glas. Co., Ltd.*, vol. 60, 2010.

[19] J. Steinhauser, "Low Pressure Chemical Vapor Deposited Zinc Oxide for Silicon Thin Film Solar Cells Optical and Electrical Properties," Lulu.com, 2008.

[20] S. M. Iftiquar, "The roles of deposition pressure and rf power in opto-electronic properties of a-SiO: H films," *J. Phys. D. Appl. Phys.*, vol. 1630, 1998.

[21] S. Fujikake, H. Ohta, A. Asano, Y. Ichikawa, and H. Sakai, "High Quality a-SiO:H Films and Their Application to a-Si Solar Cells," *MRS Proc.*, vol. 258, p. 875, Feb. 2011.

[22] D. Das, S. Iftiquar, and A. Barua, "Wide optical-gap a-SiO: H films prepared by rf glow discharge," *J. Non. Cryst. Solids*, vol. 210, pp. 148–154, 1997.

[23] Y. Tawada, H. Okamoto, and Y. Hamakawa, "a-SiC:H/a-Si:H heterojunction solar cell having more than 7.1% conversion efficiency," *Appl. Phys. Lett.*, vol. 39, no. 3, p. 237, 1981.

[24] Y. Tawada, K. Tsuge, M. Kondo, H. Okamoto, and Y. Hamakawa, "Properties and structure of a-SiC:H for high-efficiency a-Si solar cell," *J. Appl. Phys.*, vol. 53, no. 7, p. 5273, 1982.

[25] Y. Hamakawa, K. Fujimoto, K. Okuda, Y. Kashima, S. Nonomura, and H. Okamoto, "New types of high efficiency solar cells based on a-Si," *Appl. Phys. Lett.*, vol. 43, no. 7, p. 644, 1983.

[26] I. Solomon, M. Schmidt, C. Sénémaud, and M. Driss Khodja, "Band structure of carbonated amorphous silicon studied by optical, photoelectron, and x-ray spectroscopy," *Phys. Rev. B*, vol. 38, no. 18, pp. 13263–13270, Dec. 1988.

[27] M. Konagai, "Present Status and Future Prospects of Silicon Thin-Film Solar Cells," *Jpn. J. Appl. Phys.*, vol. 50, p. 030001, Mar. 2011.

[28] M. Kitagawa, K. Mori, S. Ishihara, M. Ohno, T. Hirao, Y. Yoshioka, and S. Kohiki, "Interaction of hydrogenated amorphous silicon films with transparent conductive films," *J. Appl. Phys.*, vol. 54, no. 6, p. 3269, 1983.

Chapter 7

7 Conclusions and Future Prospects

7.1 Conclusions

Photovoltaic is the most important technology for reducing CO_2 emission drastically in the near future. At this moment, crystalline silicon (c-Si) solar cells are dominant among various solar cells. However, if solar cells are produced in terawatt level, c-Si can't be produced due to the shortage of silver. On the other hand, thin-film silicon solar cells have capability of fabricating a few tenth of terawatt[1]. Therefore, thin-film silicon solar cells are promising candidate for terawatt level deployment. To accelerate the deployment of thin-film silicon solar cells, it is important to improve efficiency for cost reduction. Toward higher efficiency, tandem and triple structures are developed in order to utilize sun light in the near infrared region effectively. Therefore, transparent conductive oxide (TCO) films are required to have high performance (high transmittance and high haze ratio) in the near infrared region in addition to the visible light region. In this thesis, the study of improving mobility and increasing haze ratio in SnO_2:F film was reported.

In Chapter 3, we investigated how the electrical properties and the crystallite orientation of SnO_2:F (FTO) films fabricated by LPCVD depend on film thickness and deposition temperature. We found that, depending on film thickness, mobility peaked at different deposition temperatures. The temperature at which the mobility peaked for a thin film was higher than that for a thick film. On the basis of this result,

we introduced a temperature gradient ΔT during deposition, which improved the mobility of FTO to 77.5 cm^2/Vs. This mobility is the highest value among the reports of the deposition of FTO by CVD, as far as we know.

In Chapter 4, the results of studying the scattering mechanisms in SnO_2 films are reported. We have succeeded to simulate the dependence of the mobility both on carrier concentration and on temperature. With only one parameter, all properties can be roughly reproduced. From these results, we can understand the scattering mechanisms of SnO_2:F thin films as (1) ionized impurity scattering is dominant at higher carrier concentration than $1x10^{20}$ cm^{-3}, (2) grain barrier scattering through tunneling is dominant at lower carrier concentration than $1x10^{20}$ cm^{-3}. By using non-doped / F-doped stacked structure, we confirmed that the mobility at lower carrier concentration increase as the grain size become larger, while the mobility at higher carrier concentration don't depend on the grain size.

In Chapter 5, the fabrication of SnO_2:F films with both very high haze and high mobility was reported. We have combined F-doped SnO_2 (FTO) with high mobility deposited by LPCVD and reactive ion etching (RIE) processed glass substrate. However, two problems have been found. (1) The mobility of FTO on RIE substrate dropped from that on flat glass (75 to 36 cm^2/Vs). To avoid this drop, thicker film is needed. (2) To keep high transmittance with thicker film, lower carrier concentration is needed. But the mobility dropped with lower carrier concentration. In order to solve these constraints, we have adopted a stacked structure using thick non-doped layer of 2700 nm and thin F-doped layer of 500 nm. With this novel approach, we have successfully achieved the high mobility (80 cm^2/Vs), low carrier concentration ($2.2x10^{19}$ cm^{-3}) and high haze value (77% at wavelength of 1000 nm) at the same time. We also have found that we

can control the morphology of RIE etched glass by changing RIE pressure resulting in an increase of haze ratio at the wavelength 1000 nm drastically from 57 % (7 Pa) to 92 % (15 Pa). For evaluation purpose μc-Si:H single cells with 1 μm-thick i-layer have been fabricated on these newly developed FTO substrates using RIE conditions of 15Pa, 40min. The efficiency of 8.05% was obtained, where 7.58% was obtained in case of W-textured ZnO:B. And we also fabricated a-Si:H/μc-Si:H tandem solar cells. The efficiency of 10.87% was obtained, where 10.16% was obtained in case of W-textured ZnO:B. These results show that this newly developed W-textured FTO is a promising candidate for high efficiency thin film Si solar cells.

In Chapter 6, new method to measure whole-wavelength transmittance of TCO substrates for thin-film silicon solar cells was reported. In IM method widely used for evaluation of TCO substrates, three problems had been found in order to measure their transmittances accurately. (1) CH_2I_2 liquid itself absorbs the light in the short wavelength region. (2) The transmittance around the absorption edge of CH_2I_2 liquids is very sensitive to its amount. (3) Scattering cannot be suppressed when the scattering surfaces are more than 2 surfaces (for example, TCO on RIE etched glass substrate). To overcome these problems, we proposed new setup to measure the optical properties of TCO substrates by holding the samples inside the integral sphere. It has been confirmed that the absorption in all wavelength could be measured accurately. As the results, we have confirmed that their absorption in all wavelength could be measured accurately and the transmittance measured by the new method was well consistent with the external quantum efficiency (EQE) of the fabricated cell while the transmittance measured with conventional IM method showed differently. Therefore, this new method could be a useful tool to evaluate TCO substrates for thin-film silicon solar cells.

7.2 Future Prospects

In this study, properties of SnO_2:F films TCO substrates were improved by the application of LPCVD, introducing temperature gradient, and the combination with RIE etched glass and non-doped/F-doped stacked structures.

As described in Chapter 5, feature size can be controlled by adjusting the pressure during RIE process. If feature size becomes larger, the ability of light scattering in longer wavelength will increase, and therefore Jsc could be increased. It is known that porous and defective region are created at concaves or sharp valleys[2]. If the feature size is larger, the density of the porous and defective region will be lower, and then, Voc and FF will be higher. By exploring the larger feature size and combining with a-Si:H/μc-Si:H/μc-Si:H triple junction structure, higher efficiency than 20% (which is shown as target of 2025 in PV2030+[3]) can be expected.

Furthermore, this high performance SnO_2:F films can be applied to 5-junction thin film full spectrum solar cells with low concentration ratios to achieve a conversion efficiency of more than 40 %[4].

References

[1] A. Feltrin, A. Freundlich, Material considerations for terawatt level deployment of photovoltaics, Renew. Energy. 33 (2008) 180–185. doi:10.1016/j.renene.2007.05.024.

[2] H. Tan, E. Psomadaki, O. Isabella, M. Fischer, P. Babal, R. Vasudevan, et al., Micro-textures for efficient light trapping and improved electrical performance in thin-film nanocrystalline silicon solar cells, Appl. Phys. Lett. 103 (2013) 173905. doi:10.1063/1.4826639.

[3] NEDO, PV Roadmap 2030+, (2009).

[4] M. Konagai, Present Status and Future Prospects of Silicon Thin-Film Solar Cells, Jpn. J. Appl. Phys. 50 (2011) 030001. doi:10.1143/JJAP.50.030001.

Acknowledgements

First of all, I am sincerely indebted to Professor Makoto Konagai for giving me the opportunity of performing this study in Ph.D courses in the Tokyo Institute of Technology, although I couldn't come the laboratory so often because of the works in the Research Center of Asahi Glass Co., Ltd. I am enormously grateful for his daily supervision and precise advices throughout this research in spite of his extremely busy schedule.

I would like to give special thanks to Professor Akira Yamada, Professor Shigeki Nakagawa, Associate Professor Takaaki Manaka, and Associate Professor Shinsuke Miyajima for their valuable comments and encouragements..

I would greatly like to appreciate Dr. Porponth Sichanugrist for his great supports, discussions, and suggestions throughout this study. I couldn't finish my research and write this doctoral thesis without his valuable advices and correcting manuscripts. And I would like to appreciate Dr. Yusuke Abe for providing valuable data of cell evaluations.

I would like to appreciate Assistant Professor Yasuyoshi Kurokawa, Assistant Professor Yuzuru Ueda (moved to Tokyo University of Science), Dr. Shunsuke Kasashima (Panasonic Co., Ltd.), and Mr. Keiichi Nishikubo for their kind supports. I have learned and benefited a lot from their instructions and teaching.

I deeply appreciate secretaries at the laboratory, Ms. Kimiko Furukawa, Ms. Rie Mikado for their lots of warm and kind supports. And I want to thank all members of Konagai-Miyajima and Yamada laboratory for every support.

I would greatly like to appreciate the colleagues of Asahi Glass Co., Ltd.

Especially, I would like to appreciate Dr. Takuji Oyama for his great and kind advices and supports throughout the Ph.D course. I would like to appreciate Dr. Hidefumi Odaka for giving me the chance to begin the Ph.D course. I would like to appreciate Mr. Toru Ikeda for his valuable discussions and supports. I would like to appreciate Ms. Yasuko Ishikawa for her kind supports for all experiment. I would like to appreciate Mr. Junichi Okubo for his great contribution of introducing LPCVD equipment.

I would like to thank the New Energy and Industrial Technology Development Organization (NEDO) under METI, Japan for giving the opportunity of this study. All of this study was supported by NEDO.

Last but not least, I owe my greatest debt to my wife, Naoko Isshiki for her understanding, patience and care. Without her full support, I couldn't finish this study and this thesis. And I want to express my thanks to my daughter Maho and my son Yohei. They kindly make time for me to writing this thesis although they always want to play with me.

August 2014

Masanobu Isshik

List of Publications

Papers

1. Masanobu Isshiki, Toru Ikeda, Junichi Okubo, Takuji Oyama, Eiji Shidoji, Hidefumi Odaka, Porponth Sichanugrist, and Makoto Konagai

   "Improving Mobility of F-Doped SnO2 Thin Films by Introducing Temperature Gradient during Low-Pressure Chemical Vapor Deposition"

   Jpn. J. Appl. Phys. 51 (2012) 095801

2. Masanobu Isshiki, Yasuko Ishikawa, Toru Ikeda, Takuji Oyama, Hidefumi Odaka, Porponth Sichanugrist, and Makoto Konagai

   "SnO_2:F with Very High Haze Value and Transmittance in Near Infrared Wavelength for Use as Front Transparent Conductive Oxide Films in Thin-Film Silicon Solar Cells"

   MRS Online Proceedings Library, Vol.1536 (2014) pp 63-69.(with peer review)

3. Masanobu Isshiki, Porponth Sichanugrist, Takuji Oyama, Hidefumi Odaka, Yusuke Abe, and Makoto Konagai,

   "New method to measure whole-wavelength transmittance of TCO substrates for thin-film silicon solar cells"

   Current Applied Physics (Under Review)

International Conferences

1. Masanobu Isshiki, Yasuko Ishikawa, Toru Ikeda, Takuji Oyama, Hidefumi Odaka, Porponth Sichanugrist, and Makoto Konagai

   "SnO_2:F with Very High Haze Value and Transmittance in Near Infrared Wavelength for Use as Front Transparent Conductive Oxide Films in Thin-Film Silicon Solar Cells"

   Materials Research Society Spring Meeting, Symposium, A2.05, April 2, 2013, Moscone Center, San Francisco, California, USA

2. Masanobu Isshiki, Porponth Sichanugrist, Yusuke Abe, Makoto Konagai, Takuji Oyama, and Hidefumi Odaka

   "SnO_2:F Substrates with Larger Feature Size and Its Application to Thin-Film Silicon Solar Cells"

   23rd International Photovoltaic Science and Engineering Conference (PVSEC-23), 2-O-9, Oct. 30, 2013, Taipei International Convention Center, Taipei, Taiwan

International Workshops

1. Masanobu Isshiki, Junichi Okubo, Kunio Masumo, and Takuji Oyama

   "Full Spectrum TCO -Summary of literature study and installation of LP-CVD machine-",

2nd International Symposium on Innovative Solar Cells, Dec. 8, 2009, Epocal Tsukuba, Ibaraki, Japan (Poster presentation)

2. Masanobu Isshiki, Junichi Okubo, Toru Ikeda, Satoru Takaki
   "Full Spectrum TCO"
   3rd International Symposium on Innovative Solar Cells, Oct. 7-8, 2010, Tokyo Tech Front, Tokyo, Japan (Poster presentation)

3. Masanobu Isshiki, Yasuko Ishikawa, Toru Ikeda, Takuji Oyama, Eiji Shidoji, and Hidefumi Odaka
   "Full spectrum TCO - Toward High Transmittance in Near InfraRed -"
   4th International Symposium on Innovative Solar Cells, Mar. 5-6, 2012, Research Center for Advanced Science and Technology, Tokyo, Japan (Oral presentation)

4. Masanobu Isshiki, Toru Ikeda, Takuji Oyama, Eiji Shidoji, Hidefumi Odaka, Porponth Sichanugrist, and Makoto Konagai
   "Study of scattering mechanisms in SnO_2"
   Korea-Japan Top University League Workshop on Photovoltaics 2012, August 1-4, 2012, Korea University, Seoul, Korea (Oral and Poster presentation)

5. Masanobu Isshiki, Takuji Oyama, Yasuko Ishikawa, Hidefumi Odaka, Porponth Sichanugrist, and Makoto Konagai
   "SnO_2:F with Very High Haze Value and Transmittance in Near-Infrared Wavelength for Use as Front Transparent Conductive Oxide Films in Thin-Film

Silicon Solar Cells”

5th International Symposium on Innovative Solar Cells, Jan. 21-22, 2013, Epocal Tsukuba, Ibaraki, Japan (Poster presentation)

6. Masanobu Isshiki, Takuji Oyama, and Hidefumi Odaka

“High performance SnO_2:F TCO substrates for top cells in spectral splitting configuration”

6th International Symposium on Innovative Solar Cells, Jan. 20-21, 2014, Tokyo Tech Front, Tokyo, Japan (Oral presentation)

Domestic Conferences, Symposiums, and Workshops

1. 一色眞誠、池田徹、高木悟

“フルスペクトル TCO の研究開発”

NEDO 新エネルギー技術開発成果報告会 2010, 2010 年 7 月 27 日, 東京国際フォーラム, 東京

2. 一色眞誠

“LPCVD による高移動度フッ素ドープ酸化スズの開発”

CVD 反応分科会主催第 18 回シンポジウム「各種透明導電膜の特徴と製膜技術」, 2013 年 2 月 26 日, 文京シビックセンター, 東京 (

Patents

1. 発明者：一色眞誠、出願人：旭硝子株式会社、”フッ素ドープ酸化スズ膜形成方法”
   特願 2011-022815、特開 2012-162761、出願日：2011 年 2 月 4 日

2. 発明者：一色眞誠、池田徹、出願人：旭硝子株式会社、”フッ素ドープ酸化スズ膜形成方法”
   特願 2011-244570、特開 2013-100577、出願日：2011 年 11 月 8 日

3. 発明者：一色眞誠、出願人：旭硝子株式会社、” 透明導電性酸化物膜付き基体およびその製造方法”
   特願 2012-181722、特開 2014-037604、出願日：2012 年 8 月 20 日

4. 発明者：一色眞誠、小長井誠、出願人：東京工業大学、旭硝子株式会社、” 透明導電性酸化物膜付き基体およびその製造方法”
   特願 2012-181713、特開 2014-038807、出願日：2012 年 8 月 20 日

Books

1. 尾山卓司、高橋亮、神戸美花、一色眞誠、 II 編 12 章” U タイプ透明導電膜”、小長井 誠　植田 譲　共編、太陽電池技術ハンドブック、オーム社 2013 年 5 月